DATE ISSUED DEC " 3 1987

ORNL/Sub/84-00224/01

ORNL
MASTER COPY

A MECHANISTIC STUDY OF LOW-TEMPERATURE CORROSION ON MATERIALS IN THE COAL COMBUSTION ENVIRONMENT

Final Report
August, 1987

Report Prepared by

General Electric Company
Schenectady, NY 12345
Turbine Technology Department

R.W. Haskell
H. vonE. Doering

Corporate Research and Development
O.H. Le Blanc
K.L. Luthra

under
Subcontract Number 86X-00224C

for
OAK RIDGE NATIONAL LABORATORY
Oak Ridge, Tennessee 37831
operated by
MARTIN MARIETTA ENERGY SYSTEMS, INC.
for the
U.S. DEPARTMENT OF ENERGY
under Contract No. DE-AC05-840R21400

Printed in the United States of America. Available from
National Technical Information Service
U.S. Department of Commerce
5285 Port Royal Road, Springfield, Virginia 22161
NTIS price codes — Printed Copy A07 Microfiche A01

This report was prepared as an account of work sponsored by an agency of the United States Government. Neither the United States Government nor any agency thereof, nor any of their employees, makes any warranty, express or implied, or assumes any legal liability or responsibility for the accuracy, completeness, or usefulness of any information, apparatus, product, or process disclosed, or represents that its use would not infringe privately owned rights. Reference herein to any specific commercial product, process, or service by trade name, trademark, manufacturer, or otherwise, does not necessarily constitute or imply its endorsement, recommendation, or favoring by the United States Government or any agency thereof. The views and opinions of authors expressed herein do not necessarily state or reflect those of the United States Government or any agency thereof.

ORNL/Sub/84-00224/01

A MECHANISTIC STUDY OF LOW-TEMPERATURE CORROSION ON MATERIALS IN THE COAL COMBUSTION ENVIRONMENT

Research sponsored by the U.S. Department of Energy,
Advanced Research and Technology Development
Fossil Energy Material Program

Final Report
August, 1987

Report Prepared by

General Electric Company

Schenectady, NY 12345

Turbine Technology Department

R.W. Haskell

H. vonE. Doering

Corporate Research and Development

O.H. Le Blanc

K.L. Luthra

under
Subcontract Number 86X-00224C

for

OAK RIDGE NATIONAL LABORATORY
Oak Ridge, Tennessee 37831
operated by
MARTIN MARIETTA ENERGY SYSTEMS, INC.
for the
U.S. DEPARTMENT OF ENERGY
under Contract No. DE-AC05-840R21400

TABLE OF CONTENTS

Section			Page
	ABSTRACT		xi
	ACKNOWLEDGEMENTS		xvi
1	INTRODUCTION		1-1
2	EXAMINATION OF SPECIMENS FROM LONG-TERM MATERIALS TEST PROGRAM		2-1
	2.1	Introduction	2-1
	2.2	Deposit Chemistry of PFB-LTMT Specimens	2-1
	2.3	PFB/LTMT Corrosion Morphologies	2-8
		2.3.1 IN-738	2-8
		2.3.2 FSX-414	2-13
		2.3.3 CoCrA1Y over IN-738	2-23
		2.3.4 Platinum Aluminide over IN-738	2-23
3	THERMOCHEMICAL CALCULATIONS		3-1
	3.1	Introduction	3-1
	3.2	Thermodynamic Basis	3-2
	3.3	Melting Experiments in $K_2SO_4 - CoSO_4$	3-3
	3.4	Discussion	3-6
4	AIR-COOLED SMALL BURNER RIG (ACSBR) CONFIRMATORY TESTS		4-1
	4.1	Introduction	4-1
	4.2	Sodium Test Results	4-3
	4.3	Sodium and Potassium Test Results	4-7
	4.4	Additive Tests	4-19
	4.5	Microprobe Analyses of Selected Specimens	4-29
	4.6	Deposit Chemistry	4-41
5	CONCLUSIONS		5-1
APPENDIX A			A-1
APPENDIX B			B-1
APPENDIX C			C-1
REFERENCES			R-1
REPORT DISTRIBUTION LIST (as specified by MMEC)			

LIST OF ILLUSTRATIONS

Figure		Page
2-1.	Long-Term Materials Test Facility.	2-2
2-2.	Low-Temperature Corrosion Study, Specimens from LTMT IN-738, 1500 °F, 400X, As Polished.	2-9
2-3.	Low-Temperature Corrosion Study, Specimens from LTMT IN-738, 1300 °F, 400X, As Polished.	2-10
2-4.	Low-Temperature Corrosion Study, Test No. 3, ACSBR 1500 °F, IN-738, 400X, As Polished.	2-11
2-5.	Low-Temperature Corrosion Study, Test No. 1, ACSBR 1300 °F, IN-738, 400X, As Polished.	2-12
2-6a.	Microprobe Spectra, IN-738: Matrix.	2-14
2-6b.	Microprobe Spectra, IN-738: Corrosion Scale, 1500 °F Specimen.	2-14
2-7a.	Microprobe Spectra, IN-738: Outside Scale, 1300 °F Specimen.	2-15
2-7b.	Microprobe Spectra, IN-738: Corrosion Near Matrix, 1300 °F Specimen.	2-15
2-8a.	Electron Image, 400X, LTMT 1300 °F, Pin, IN-738.	2-16
2-8b.	Sulfur Map, 400X, LTMT 1300 °F, Pin, IN-738.	2-16
2-9a.	Nickel Map, 400X, LTMT, 1300 °F Pin, IN-738.	2-17
2-9b.	Chromium Map, 400X, LTMT, 1300 °F Pin, IN-738.	2-17
2-9c.	IN-738 Low Ni/S Area	2-18
2-9d.	IN-738 High Ni/S Area	2-18
2-10.	Specimen from LTMT, FSX-414, 1500 °F, As Polished.	2-19
2-11.	Specimen from LTMT, FSX-414, 1300 °F, As Polished	2-20
2-12a.	Microprobe Spectra, Outer Scale FSX-414, 1500 °F.	2-21
2-12b.	Microprobe Spectra, Light-Colored Internal Precipitate, FSX-414, 1500 °F.	2-21
2-12c.	Microprobe Spectra, Dark-Colored Grain Boundary Precipitate, FSX-414, 1500 °F.	2-22
2-13a.	Current Image, 400X, LTMT, 1300 °F Pin, FSX-414.	2-24
2-13b.	Sulfur Map, 400X, LTMT, 1300 °F Pin, FSX-414.	2-24
2-14a.	Cobalt Map, 400X LTMT, 1300 °F Pin, FSX-414.	2-25
2-14b.	Chromium Map, 400X, LTMT, 1300 °F Pin, FSX-414.	2-25

LIST OF ILLUSTRATIONS

Figure		Page
2-14c.	Nickel Map, 400X, LTMT, 1300 °F Pin, FSX-414.	2-26
2-15.	LTMT, CoCrAlY over IN-738, 1300 °F, 400X As Polished.	2-27
2-16.	LTMT, CoCrAlY over IN738, 1100 °F, 400X As Polished.	2-28
2-17.	Sulfur Map, 1100 °F Specimen.	2-29
2-18.	Sulfur Map, 1300 °F Specimen.	2-29
2-19.	LTMT, RT22 over IN-738, 1500 °F, 400X, As Polished.	2-30
2-20.	LTMT, RT22 over IN-738, 1300 °F, 400X, As Polished.	2-31
2-21.	LTMT, RT22 over IN-738, 1100 °F, 400X, As Polished.	2-32
2-22.	Microprobe Spectra (Area 2) Near Scale - Alloy Interface, 1500 °F Specimen.	2-33
2-23.	Microprobe Spectra (Area 2) Inner Scale, 1300 °F Specimen.	2-35
2-24.	Microprobe Spectra (Area 1) Outer Scale, 1300 °F Specimen.	2-35
2-25.	Sulfur Map, 580X, 1300 °F Specimen at Bottom of Pit, Scale-Alloy Interface (image is reversed).	2-36
2-26.	Microprobe Spectra (Area 1), Outer Scale, 1100 °F Specimen.	2-37
2-27.	Microprobe Spectra (Area 2), Pit Bottom, 1100 °F Specimen.	2-37
2-28.	Pt Map (left-hand edge of pit in Figure 2-21, image reversed), Coating and Pit, 1100 °F Specimen, 560X.	2-38
2-29.	S Map (left-hand edge of pit in Figure 2-21, image reversed), Coating and Pit, 1100 °F Specimen, 560X.	2-38
3-1.	SO_3 partial pressures at the freezing point calculated as described in Appendix A for K_2SO_4-$CoSO_4$-Na_2SO_4 mixtures containing Na_2SO_4:K_2SO_4 mole ratios of 100:0, 0:100, and 69:31.	3-2
3-2.	Calculated values of the minimum P_{SO_3} required to form a K_2SO_4-$CoSO_4$ liquid from Co_3O_4 at P_{O_2} = 1 atm and from CoO.	3-5
4-1.	Air-Cooled Small Burner.	4-2
4-2.	Air-Cooled Small Burner Rig, IN-738, Test No. 1, 1600 °F specimen, 200X, 2-2-1 Etch.	4-5
4-3.	Air-Cooled Small Burner Rig, IN-738, Test No. 1, 1500 °F specimen, 200X, 2-2-1 Etch.	4-5
4-4.	Air-Cooled Small Burner Rig, IN-738, Test No. 1, 1400 °F specimen, 200X, 2-2-1 Etch.	4-5

LIST OF ILLUSTRATIONS

Figure		Page
4-5.	Air-Cooled Small Burner Rig, IN-738, Test No. 1, 1300 °F specimen, 200X, 2-2-1 Etch.	4-5
4-6.	Air-Cooled Small Burner Rig, IN-738, Test No. 1, 1200 °F specimen, 200X, 2-2-1 Etch.	4-6
4-7.	Air-Cooled Small Burner Rig, IN-738, Test No. 1, 1100 °F specimen, 200X, 2-2-1 Etch.	4-6
4-8.	Air-Cooled Small Burner Rig, IN-738, Test No. 2, 1600 °F specimen, 200X, 2-2-1 Etch.	4-8
4-9.	Air-Cooled Small Burner Rig, IN-738, Test No. 2, 1500 °F specimen, 200X, 2-2-1 Etch.	4-8
4-10.	Air-Cooled Small Burner Rig, IN-738, Test No. 2, 1400 °F specimen, 200X, 2-2-1 Etch.	4-8
4-11.	ACSBR, Test No. 3, 1500 °F, 200X, 2-2-1 Etch.	4-9
4-12.	ACSBR, Test No. 3, 1400 °F, 200X, 2-2-1 Etch.	4-10
4-13.	ACSBR, Test No. 4, 1600 °F, 200X, 2-2-1 Etch.	4-12
4-14.	ACSBR, Test No. 4, 1300 °F, 200X, 2-2-1 Etch.	4-12
4-15.	ACSBR, Test No. 4, 1100 °F, 200X, 2-2-1 Etch.	4-12
4-16.	ACSBR, Test No. 5, 1300 °F, 200X, 2-2-1 Etch.	4-13
4-17.	ACSBR, Test No. 5, 1400 °F, Leading Edge, 200X, 2-2-1 Etch.	4-13
4-18.	ACSBR, Test No. 5, 1400 °F, Trailing Edge, 200X, 2-2-1 Etch.	4-13
4-19.	1600 °F Specimen, ACSBR (etched 2-2-1) 100X.	4-14
4-20a.	1500 °F Specimen, ACSBR, Area of Attack (etched 2-2-1) 100X.	4-15
4-20b.	1500 °F Specimen, ACSBR, Area of Uniform Attack near a Pit (etched 2-2-1) 400X.	4-16
4-21.	1300 °F Specimen, ACSBR (etched 2-2-1) 400X.	4-17
4-22.	Corrosion versus Temperature.	4-18
4-23a.	1600 °F Specimen, ACSBR (etched 2-2-1), 400X.	4-20
4-23b.	1600 °F Specimen, ACSBR (etched 2-2-1), 200X.	4-20
4-24.	1500 °F Specimen, ACSBR (etched 2-2-1), 400X.	4-21
4-25a.	1400 °F Specimen, ACSBR (etched 2-2-1), 400X.	4-21
4-25b.	1400 °F Specimen, showing pit ACSBR (etched 2-2-1), 400X.	4-21
4-26.	1300 °F Specimen, ACSBR (etched 2-2-1), 400X.	4-22

LIST OF ILLUSTRATIONS

Figure		Page
4-27.	1200 °F Specimen, ACSBR (etched 2-2-1), 400X.	4-22
4-28.	1100 °F Specimen, ACSBR (etched 2-2-1), 400X.	4-22
4-29.	1600 °F Specimen, Test 8 (etched 2-2-1), 400X.	4-25
4-30.	1400 °F Specimen, Test 8 (etched 2-2-1), 400X.	4-26
4-31.	1300 °F Specimen, Test 8 (etched 2-2-1), 400X.	4-27
4-32.	1200 °F Specimen, Test 8 (etched 2-2-1), 400X.	4-28
4-33.	1600 °F Specimen, Test 9 (etched 2-2-1), 400X.	4-30
4-34.	1500 °F Specimen, Test 9 (etched 2-2-1), 400X.	4-31
4-35.	1400 °F Specimen, Test 9 (etched 2-2-1), 400X.	4-32
4-36.	1300 °F Specimen, Test 9 (etched 2-2-1), 400X.	4-33
4-37.	Test 1, Specimen Image, 1000X.	4-34
4-38.	Test 1, Sulfur Map, 1000X.	4-34
4-39.	Test 1, Ni Map, 1000X.	4-35
4-40.	Test 1, Cr Map, 1000X.	4-35
4-41.	Test 1, Al Map, 1000X.	4-36
4-42.	Test 1, Ti Map, 1000X.	4-36
4-43.	Test 1, W Map, 1000X.	4-37
4-44.	Test 1, Co Map, 1000X.	4-37
4-45.	Test 3, Specimen Image, 1000X.	4-38
4-46.	Test 3, Sulfur Map, 1000X.	4-38
4-47.	Test 3, Cr Map, 1000X.	4-39
4-48.	Test 3, Al Map, 1000X.	4-39
4-49.	Test 3, Ni Map, 1000X.	4-40
4-50.	Test 4, Specimen Image, 100X.	4-42
4-51.	Test 4, Sulfur Map, 100X.	4-42
4-52.	Test 4, K Map, 100X.	4-43
4-53.	Test 4, Ni Map, 100X.	4-43
4-54.	Test 4, Cr Map, 100X.	4-44
4-55.	Test 4, Spectrum Image, 2000X.	4-44

LIST OF ILLUSTRATIONS

Figure		Page
4-56.	Test 4, Sulfur Map, 2000X.	4-45
4-57.	Test 4, K Map, 2000X.	4-45
4-58.	Test 4, Ni Map, 2000X.	4-46
4-59.	Test 4, Al Map, 2000X.	4-46
4-60.	Mole Percent Alloy Sulfates versus Temperature.	4-50
A-1.	K_2SO_4-$CoSO_4$ binary phase diagram.	A-2
A-2	Na_2SO_4-$CoSO_4$, binary phase diagram.	A-2
A-3.	Test plots of a quantity related to the partial molar heat of mixing of K_2SO_4 as a function of the mole fraction of $CoSO_4$ along the liquidus line in the K_2SO_4-$CoSO_4$ system using two separate approximations for the entropy of mixing.	A-4
A-4.	K_2SO_4-$CoSO_4$-Na_2SO_4 ternary phase diagram estimated from the three binary phase diagrams as described in the text.	A-8
A-5.	SO_3 partial pressures at the freezing point of liquid mixtures in equilibrium with K_2SO_4-$CoSO_4$-Na_2SO_4 solid solutions, Co_3O_4 (s), and 1 atm O_2, calculated as described in the text.	A-9
A-6.	K_2SO_4-Na_2SO_4 binary phase diagram.	A-12
A-7.	Geometrical basis of the Toop algorithm [24] as we apply it.	A-13
B-1	Fraction (F) of sulfur converting to SO_3.	B-1

LIST OF TABLES

Table		Page
2-1	LTMT Operating Conditions	2-3
2-2	Coal Analysis Pittsburgh No. 8	2-4
2-3	Chemical Analysis of Dolomites	2-5
2-4	Chemical Analysis of Deposits on Low-Velocity Test Section Pin Specimens (Water Soluble)	2-6
2-5	Chemical Analysis of Deposits on Low-Velocity Test Section Pin Specimens (Acid Soluble)	2-7
3-1	Results of Sulfation Experiments in O_2 - 0.0023% (SO_2 + SO_3)	3-4
4-1	ACSBR Test Conditions	4-4
4-2	ACSBR Test Corrosion	4-4
4-3	Concentrations (ppm) In 40cc Deposit Washing	4-47
4-4	Alloy Sulfate Concentrations (ppm) In 40 cc Deposit Washing	4-47
4-5	Deposit Chemistry, Test 8	4-48
4-6	ACSBR Test Deposit Chemistry	4-51
4-7	pH of Deposit Washings	4-52
A-1	Free Energy of "Pure" Components in Each Phase	A-10
A-2	Excess Free Energies of Mixing of Binary Phases	A-10
A-3	Temkin Ideal Free Energies of Mixing	A-13
C-1	Activity of NiO in the Presence of V_2O_5 and $Ni_3(VO_4)_2$	C-2

This report was prepared as an account of research sponsored by the U.S. Department of Energy, AR&TD Fossil Energy Materials Program, DOE/FE AA 15 10 10 0, Work Breakdown Structure Element GE-3.

ABSTRACT

INTRODUCTION

The low-temperature corrosion program arose because of the hot corrosion observed at temperatures as low as 1100 °F in the Long-Term Materials Test (LTMT). The LTMT was sponsored by DOE and involved the operation of the pressurized fluidized bed combustor (PFBC). General Electric operated the combustor at Malta, NY. In the LTMT, combustion gases were run through sections containing a variety of materials for several thousand hours.

The low-temperature corrosion program was a two-year research effort to develop an understanding of the low-temperature hot corrosion phenomena observed during the LTMT. The program involved three tasks: 1) an analysis of selected specimens from the LTMT, 2) thermochemical stability calculations on what molten salts were formed to permit hot corrosion at such low temperatures, and 3) operation of burner rig tests which would simulate the LTMT-PFBC conditions and test the conclusions of the thermochemical calculations.

EXAMINATION OF SPECIMENS FROM LTMT

The PFBC burned about a 2/1 mixture of coal and dolomite. The combustion gases were cooled by an in-bed heat exchanger to about 1750 °F and then passed through a low-velocity test section where specimens were held at about 1500 °F (the gas temperature), 1300 °F, and 1100 °F, respectively. Gas pressure in the test section was 10 atm. Sulfur concentration calculated as SO_2 was 10^{-3} to 10^{-4} atm.

Deposit analyses from the PFBC test section were reviewed. These revealed deposits consisting mainly of flyash from the coal, and Mg and Ca sulfates derived from the dolomite used in gettering the sulfur. The levels of water soluble alkali were in the 0.1% to 1.0% range. The alkali sulfates are responsible for hot corrosion. At this level they can lead to hot corrosion of otherwise corrosion-resistant materials. The table below gives a sample of the corrosion data taken. There are several aspects of this data that are surprising and disturbing. In spite of a gettering of over 90% of the sulfur as well as the use of three cyclones, corrosion rates remained substantial. The corrosion rates did not decrease when the temperature decreased from 1500-1300 °F. Sometimes the corrosion persisted to 1100 °F. The high rate of attack of the cobalt base alloy [FSX-414 (29% Cr)], relative to the nickel base alloy [IN-738 (16% Cr)], is unexpected as the cobalt base alloy is considerably more resistant under typical hot-corrosion conditions as caused by sea salt type fuel contamination or sodium sulfate induced hot corrosion. There was some indication of an increase in alkali concentration in the deposits as the specimen temperature decreased.

SAMPLE CORROSION, LOW-VELOCITY TEST SECTION, LTMT

	T(°F)	Mils	Hours
IN-738	1500	4.4	5785
	1300	4.5	3098
FSX-414	1500	5.9	5785
	1300	3.1	5785

Specimens of FSX-414 (a cobalt base material), IN-738 (a nickel base material), IN-738 coated with Co-CrAlY, and IN-738 coated with a Pt-aluminide were analyzed metallographically and by microprobe. The microstructural analysis of these materials from the PFB-LTMT showed a typical high-temperature hot corrosion morphology at 1500 °F with internal precipitates of oxide and sulfide, depleted metal (metal where the Cr has been removed by the corrosion process), and a porous scale. For the lower temperature specimens, the oxide scale became dense and layered. (See Figures 2-2 and 2-3.) Often there were pits and the internal precipitates were absent. Sulfides were found in the scale along the scale-metal interface.

THERMOCHEMICAL CALCULATIONS

The thermochemical analysis began with a knowledge that for hot corrosion to occur a liquid salt must be present, and for hot corrosion to occur below the melting point of sodium sulfate (mpt = 1623 °F, the alkali salt found on gas turbine parts) some other constituents must be present which lower the melting point of the salt. One way in which this is known to occur is through the formation of cobalt sulfate. The eutectic temperature in the sodium-cobalt sulfate system is 1061 °F. Cobalt-sodium sulfate mixtures are known to be responsible for low-temperature hot corrosion from analysis of the salts present on gas turbine airfoils. (Most hot gas path turbine materials contain cobalt. It is generally the most stable of the alloying element sulfates.) Thermochemical calculations show that cobalt sulfate is stable under conditions normally found in liquid burning gas turbines.

The new aspect in the PFB-LTMT results was thought to be the presence of potassium. It was apparent from past burner rig work* that a sodium-potassium containing salt could be far more aggressive than a sodium containing salt. The thermochemical analysis thus began with trying to work out the Na-K-Co sulfate system.

The binary diagrams were known, but they were not ideal. The binary Na_2SO_4-$CoSO_4$ could be fit by a regular solution model. The K_2SO_4-$CoSO_4$ binary required a subregular model. The K_2SO_4-Na_2SO_4 system could also be fit with a regular solution model. The problem was to develop the ternary diagram from the individual binaries. A model for doing this is available and was applied and the ternary was constructed. From the analysis the stability of $CoSO_4$ was determined. The results clearly show the stabilizing effect of K.

*High-Temperature Gas Turbine Engine Component Materials Testing Program, Task 1, "Fireside 1" Final Report, 7/1/78, GE Gas Turbine Div, DOE Contract No. EX-76-C-01-1765.

For instance for a 69:31 molar ratio of Na+K sulfates, a liquid salt (Na, K and Co sulfates) is stable for P_{SO_3} levels one order of magnitude less than that for Na alone. The results of these calculations showed that there is a substantial increase in the range of temperature and sulfur level over which a liquid salt (consisting of alkali and alloy sulfates) is stable and therefore over which hot corrosion may occur.

Melting type experiments were performed to test the theoretical thermodynamic calculations. These involved applying K_2SO_4 and K_2SO_4-$CoSO_4$ salt mixtures to cobalt samples and determining if a molten salt developed by analyzing the salt that existed after exposure to various temperatures and SO_3 concentrations. Thus, if K_2SO_4 was applied to a sample and after several hours a K_2SO_4-$CoSO_4$ mixture was found, then $CoSO_4$ was stable and melting had occurred. Similarly, if a K_2SO_4-$CoSO_4$ mixture was applied and after several hours only K_2SO_4 was present, then $CoSO_4$ was not stable and a liquid could not be maintained. The observations of these experiments were found to be in good agreement with the calculations.

AIR-COOLED SMALL BURNER RIG RESULTS

To confirm the theoretical analyses and to simulate the conditions of the PFB, a small burner rig (1 atm) was modified so as to allow the use of air-cooled specimens. All specimens were the nickel base alloy IN-738 (8.5 Co, 16 Cr, 3.4 Al, 3.4 Ti, 1.75 Mo, 2.6 W, 0.9 Cb, 1.75 Ta). The gas velocities were about the same as for the PFB low-velocity test section in the Long-Term Materials Test. To simulate the corrosive contaminants present in the PFB combustion gases a distillate fuel was doped. Three series of tests were run: those with Na alone as a fuel contaminant, those with Na and K as fuel contaminants and those with Na-K-Mg as fuel contaminants. Sulfur in the combustion gases was controlled by SO_2 additions to the burner rig air and/or sulfur additions to the fuel. As noted in the thermochemical analysis, it is the SO_3 pressure which determines alloy sulfate (Co and Ni) stability, but this cannot be known precisely in the burner rig or turbine. Although the SO_3 is fixed in the combustion zone at about 5% (the remainder remains as SO_2) and does not change much in bulk value after this, it does change near a catalytic surface (and salt-covered metallic surfaces will have a catalytic effect) and may approach equilibrium values, estimated to be about 50% of the available sulfur at 1500 °F and 10 atm and 25% at 1500 °F and 1 atm. The numbers at 1300 °F are 80% at 10 atm and 50% at 1 atm.

The three Na fuel contaminant tests established that for high sulfur additions ($P_{SO_2} = 3.8 \times 10^{-3}$ atm) hot corrosion was high from 1600 °F through 1300 °F and fell off, reaching about 0.1 of the highest level by 1100 °F. The Na fuel contaminant level was 125 ppm in the fuel in each of these tests. Interestingly, when the SO_2 input level was reduced to 2.7×10^{-5} atm, corrosion nearly ceased below 1600 °F. This was in accord with the thermochemical calculations showing that $CoSO_4$ (the most stable of the alloy sulfates) is not stable in a Na_2SO_4 melt below about $P_{SO_3} = 1.5 \times 10^{-5}$ atm. (For purposes of comparison in the LTMT low-velocity test section $P_{SO_2} = 10^{-3}$ to 10^{-4} atm)

The next three tests were run where the fuel additions were nominally 85 ppm Na and 100 ppm K. These tests simulated the corrosion causing contaminants from coal combustion. Successive runs were made for $P_{SO_2} = 1.4 \times 10^{-4}$ atm, 2.2×10^{-5} atm, and 4.1×10^{-6} atm resulting in considerable low-temperature corrosion, reduced low-temperature corrosion, and finally no low-temperature corrosion, respectively. Thermochemical calculations predicted $P_{SO_3} = 1 \times 10^{-6}$ atm was required to stabilize $CoSO_4$.

Thus, low-temperature corrosion was predicted in the first test. The second test probably ran close to the critical sulfur pressure below which low-temperature corrosion would not occur. The third test ran well below the critical sulfur pressure. These tests confirmed the theoretical thermodynamic calculations and in particular demonstrated the enhancement of corrosion due to the presence of K as predicted by the theory.

Finally, three tests were run to investigate the role of the additive Mg on low-temperature corrosion. (The Mg level was essentially the same in all three tests, about 460 ppm. The sulfur level in terms of SO_2 was 38 x 10^{-4} atm in all the additive tests, as high as the highest level used in any of the previous tests.) Mg was important in the PFB-LTMT deposits, arising from the dolomite used to getter the sulfur. It is common in deposits from the combustion of coal and is used in the inhibition of V corrosion when heavy fuels are burned in gas turbines.

A first additive test run was made with Mg and Na as the fuel contaminants. This test was the same as the most aggressive of the Na tests except for the presence of the Mg. The corrosion results show a substantial reduction in the corrosion compared to the no Mg case. The reduction amounts to at least 0.30 of the original rate over the temperature range 1600-1300 °F. In the second additive test, V was added to the contaminants in the first additive test, as there were theoretical reasons for believing it would inhibit the formation of $CoSO_4$. The other test conditions were held constant. The presence of V may have slightly reduced the already low corrosion rate. It did result in deposits which were much more difficult to remove than those in the first additive test. A final additive test was run with Na, K, and Mg as the contaminants. Again, the corrosion rate when compared to the most aggressive of the Na-K tests was quite low; however, a pitting attack was noted at 1400 °F with the maximum pit size giving a rate about 0.5 of that observed in the most aggressive Na-K test, (This final additive test was at a sulfur pressure of 38 x 10^{-4} versus a sulfur pressure of 1.4 x 10^{-4} for the most aggressive Na+K test.)

Microprobe analysis was performed on selected specimens from the ACSBR tests. The specimens selected were in the 1300-1400 °F ranged from the Na and Na+K tests. Like the LTMT-PFB microstructures in this temperature range layered type corrosion structures were observed and sulfides were confined to the bottom of the layered structured. These were associated with Ni and sometimes Cr. As the temperature was raised the layered structures begin to have internal precipitates appear beneath them, the precipitates being Cr sulfides. This is in the 1400 °F range. At still higher temperatures a porous scale develops, and the amount of internal precipitates increases. These are sulfides and oxides with the former generally being deeper into the matrix. For one of the Na+K tests considerable K was retained in the deposit/scale. This proved to be K_2SO_4-$NiSO_2$ in a porous NiO. The NiO may be a precipitate from the salt melt.

Specimen deposit samples were taken after each run in the ACSBR and analyzed for the fuel contaminants and alloy sulfates. Of principal concern in this study was the amount of alloy sulfate in the deposits. As the formation of these compounds allows a reduction in the melting point of the alkali salt deposit, they are necessary according to theory for low-temperature corrosion to occur. The analyses clearly showed this correlation. At high sulfur levels alloy sulfate formation was high and low-temperature corrosion was substantial. At very low sulfur levels (as were produced using kerosine as a fuel) almost no alloy sulfates were found in the salt deposits and low-temperature corrosion ceased.

As temperatures were reduced alloy sulfates became more stable and were found in higher percentages in the deposits in agreement with the theory. In the additive tests where corrosion was substantially reduced the levels of alkali and alloy sulfates were reduced compared to what they were in comparable tests where only alkali was present. There was a tendency for the amount of alkali collected on specimens to increase in amount as the temperature was reduced from 1600-1300 °F or 1400 °F. Below this the amount of alkali collected fell off. This happened in all 9 tests. This may be related to the air cooling of the specimens. The falling off of deposit collected at 1200 °F and 1100 °F may be a result of lack of liquid formation at these temperatures.

In conclusion the program has shown that there is an increase in hot corrosion where potassium sulfate is present. This was observed in the LTMT tests. This enhancement will be present in all coal environments. This enhancement has two aspects. One, there is an increase in high-temperature hot corrosion (1400-1600 °F), because potassium sulfate lowers the melting point of sodium sulfate. Two, potassium sulfate stabilizes the alloy sulfates nickel and cobalt, particularly the latter, and thus substantially reduces the SO_3 pressure required for their formation. Thus, low-temperature hot corrosion (1100-1400 °F) can occur over a larger range of sulfur levels. These aspects of hot corrosion were demonstrated in tests and examined by thermochemical calculations in this report.

ACKNOWLEDGMENTS

The authors appreciate the assistance of Robin Brobst and Russell Mc Carron concerning the LTMT experience. Tim Michelfelder and Fred Adinolfi provided much support and expertise in the construction and operation of the air-cooled small burner rig. The personnel of the M & P laboratory were most helpful in providing timely metallographic and chemical services. The editorial and related report preparation services of the R & D Center Publications Unit are also greatly appreciated.

1. INTRODUCTION

Most coals contain a large number of impurities, particularly sulfur compounds and sodium and potassium salts, which upon combustion form products that are corrosive at high temperatures. Also, dolomites used to getter sulfur may be significant contributors to the alkali present. Corrosion can be serious in systems using coal-derived liquid or gaseous fuels or where coal combustion gases are directly used for power generation, as in a pressurized fluidized bed coal combustor (PFBC) gas turbine (GT) combined cycle. The alkali and sulfur impurities present in such combustion gases result in condensates containing sodium and potassium sulfates [1]. Such mixtures are more corrosive than salts containing sodium sulfate alone [2,3].

Sodium sulfate can cause severe degradation of hot gas turbine components at temperatures well below the melting point of sodium sulfate. The mechanism of this phenomenon has been the subject of many studies [4-7]. Corrosion is caused by the formation of low melting eutectics, such as Na_2SO_4-$CoSO_4$ (m.pt. ¤ 575 °C) [8]. Potassium sulfate also forms a similar eutectic with $CoSO_4$ (m.pt. = 535 °C) [8]. Therefore, it is expected that K_2SO_4 will also cause low-temperature hot corrosion.

The work reported here is directed at gaining a basic understanding of the low-temperature corrosion observed in the DOE Long-Term Materials Test (LTMT) at the GE (Malta, New York) PFBC. This corrosion occurs in the temperature range 1100-1400 °F on a variety of alloys and protective coatings including Co-, Ni-, and Fe-based materials and Al-rich materials. It has many similarities to the attack of Co-based and Ni-based alloys in the temperature range 1100-1500 °F in the presence of Na_2SO_4 and sufficient levels of SO_3 in oil-fired gas turbines. However, there are some unique features of this process, as observed in the combustion products from the PFBC, which have not been investigated to date.

This study has three tasks:

1. Obtain a more detailed understanding of the corrosion morphology and interface chemistry on selected specimens from the Malta PFBC.
2. Perform thermochemical calculations from data available in the literature to establish the range of conditions for stability of alloy phases, corrosion products, and the chemical compounds observed.
3. Run small burner rig tests to correlate the observations on specimens with predictions from the thermochemical calculations.

2. EXAMINATION OF SPECIMENS LONG-TERM MATERIALS TEST PROGRAM

2.1 INTRODUCTION

Under this task specimens from the low-velocity test section in the Long-Term Materials Test Program (LTMT) were evaluated. This program began when the General Electric Company, under contract to the U.S. Department of Energy (DOE), tested selected turbine materials for times greater than 10,000 hours in a PFBC test facility at Malta, NY. The facility, which was designed and constructed to provide an environment representative of current environmental requirements, was adapted from the 12-inch test rigs at NCB/CURL [9] and Exxon [10] to assure simplicity in design, operation, maintenance, and low operating cost.

Figure 2-1 shows the General Electric Pressurized Fluidized Bed Coal Combustion facility. Coal and dolomite are fed into a mixer at a constant ratio of 100 lb coal/55 lb dolomite. The mixer combines the solids and acts as a storage vessel. A bucket elevator transports the solids from the mixer to either one of two solids feed lockhoppers. From the lockhoppers, the solids flow by gravity into the solids feedhopper and then to the rotary feeder which controls the rate of solids fed to the air transport line feeding the combustor. In the combustion zone, an in-bed heat exchanger removes heat from the bed such that, with a bed temperature of 1750 °F at 150 psia, the excess air is greater than 20 percent.

Hot combustion products leave the combustor and flow through three stages of cyclones before entering the materials test sections. Two test sections, designed to evaluate the corrosion and erosion/corrosion resistance of candidate gas turbine materials in a PFB flue gas environment, are arranged in series. The first of these is the low-velocity test section designed to study long-term materials corrosion effects.

The low-velocity test section is a 4-inch I.D. pipe, fabricated from RA-333 with 240 nipples welded perpendicular to its long axis and enclosed with 50 inches of Fiber-frax® insulation. The test section can accommodate up to 120 uncooled pins and 60 air-cooled points.

Table 2-1 gives the PFB operating conditions and Tables 2-2 and 2-3 give the chemistries for the coal and dolomites used, respectively.

2.2 DEPOSIT CHEMISTRY OF PFB-LTMT SPECIMENS

The chemistry data on the deposits from pins in the low-velocity test section (LVTS) from the PFB in the Long-Term Materials Test Program were reviewed and analyzed. Tables 2-4 and 2-5 give the overall analyses for the alkali and alkaline metals found in the deposits. The pin temperatures are the metal temperatures as measured by a thermocouple embedded within the metal. The 0.250-inch-diameter pins, arranged in cross-flow to the combustion gases from the PFB, were air cooled through a 0.125-inch-diameter hole. The nominal gas temperature in the LVTS was 1500 °F, and this was one of the three test temperatures. With air cooling, pin metal temperatures of 1300 °F and 1100 °F were attained for the other pin temperatures.

®Registered trademark of the General Electric Company.

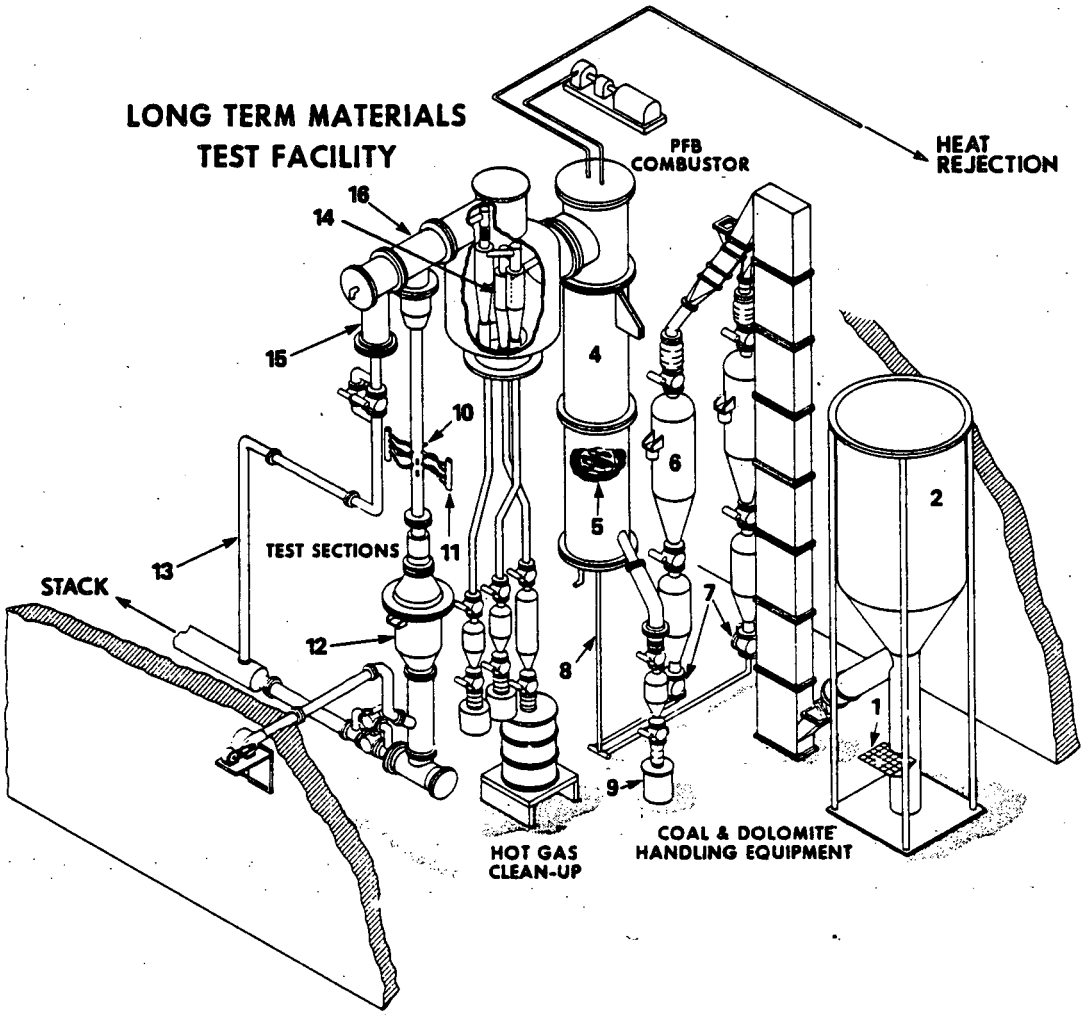

1	COAL/DOLOMITE FEED	9	SPENT BED MATERIAL
2	MIXER	10	LVTS SPECIMENS
3	BUCKET ELEVATOR	11	SPECIMEN COOLING AIR MANIFOLD
4	COMBUSTOR	12	HVTS PRESSURE VESSEL
5	IN-BED HEAT EXCH.	13	BYPASS
6	LOCKHOPPER	14	CYCLONES
7	ROTARY VALVES	15	DUST/ALKALI ANALYSIS
8	AIR TRANSPORT LINES	16	GAS ANALYSIS

Figure 2-1. Long-Term Materials Test Facility.

Table 2-1

LTMT OPERATING CONDITIONS

Combustor	
Coal	Pittsburgh No. 8
Dolomite	Pfizer, National Lime and Stone Co. No. 11
Bed Temperature	1640 - 1660 °F
Bed Pressure	150 psia
Fluidizing Velocity	2.4-2.7 ft/s
Bed Height	6 ft Nominal
Excess Air	30-40%
Ca/S	1.7-2.3
Low-Velocity Test Section (LVTS)	
Gas Pressure	145 psia
Gas Velocity	23 ft/s
Inlet Temp	1500 - 1520 °F
Outlet Temp	1440 - 1480 °F
Cooled Pin Temps	1300 F $^{+}$50 °F, 1100 °F $^{+}$50 °F
High Velocity Test Section	
Temperature	1325 - 1375 °F
Dust Loading	30-90 ppm
Mean Particle Size (Microns)[1]	1.9-3.1
Percent Particles > 10 Microns[1]	2-10
Gas Velocity	800-900 ft/s (Airfoils) 1300-1400 ft/s (Erosion Pin)

[1] Range of 15 analyses

Table 2-2

COAL ANALYSIS
PITTSBURGH NO. 8

(Wt%)

	Range of 3 Analysis	Avg.
Proximate Analysis (As Received)		
Moisture	1.38-1.86	1.63
Ash	14.26-16.87	15.47
Volatile	35.60-37.71	36.68
Fixed Carbon	46.15-46.34	46.22
Btu/lb	12084-12485	12293
Ultimate Analysis (As-Received)		
Moisture	1.38-1.86	1.63
Carbon	66.22-68.38	67.41
Hydrogen	4.65-4.80	4.75
Nitrogen	1.28-1.37	1.34
Chlorine	0.13	0.13
Sulfur	4.79-5.07	4.93
Ash	14.26-16.87	15.47
Oxygen	4.16-4.53	4.34
Ash Analysis		
SiO_2	35.94-39.96	38.47
Al_2O_3	19.21-20.51	20.05
Fe_2O_3	33.60-38.86	35.65
TiO_2	0.84-0.98	0.93
CaO	0.70-1.04	0.84
MgO	0.66-0.70	0.67
K_2O	1.51-1.83	1.69
Na_2O	0.00-0.24	0.14
SO_3	0.74-1.00	0.86

Table 2-3

CHEMICAL ANALYSIS OF DOLOMITES
(Wt%)

	Pfizer	National Lime and Stone No. 20
CO_2 (loss)	43.68	47.16
CaO	31.81	28.98
MgO	22.83	20.29
SiO_2	1.52	1.38
Al_2O_3	0.57	0.78
Fe_2O_3	0.22	0.69
K_2O	0.0	0.03
Na_2O	0.15	0.16
SO_3	0.67	0.45
Cl (ar)	0.24	0.18

Note: Pfizer used first 1923 hours of operation. National Lime and Stone material used for remainder of test.

Table 2-4

CHEMICAL ANALYSES OF DEPOSITS ON LOW-VELOCITY TEST SECTION PIN SPECIMENS (WATER SOLUBLE)

PERCENT IN DEPOSITS

Pin Temperature (°F)	Na	K	Ca	Mg
1500	0.06	0.25	8.6	1.6
1300	0.25	1.5	8.5	1.7
1100	0.19	1.3	8.1	2.2

ENRICHMENT FACTORS

Pin Temperature (°F)	Na	K	Ca	Mg
1500	1	1	1	1
1300	4.2	5.8	1.0	1.1
1100	3.2	5.2	0.9	1.4

Table 2-5

CHEMICAL ANALYSIS OF DEPOSITS ON LOW-VELOCITY TEST SECTION PIN SPECIMENS (ACID SOLUBLE)

PERCENT IN DEPOSITS

Pin Temperature (°F)	Na	K	Ca	Mg
1500	0.32	1.1	9.1	4.3
1300	0.69	3.1	9.8	4.2
1100	0.52	2.3	10.4	4.5

ENRICHMENT FACTORS

Pin Temperature (°F)	Na	K	Ca	Mg
1500	1	1	1	1
1300	1.7	1.9	2.6	0.9
1100	1.3	1.1	4.6	0.9

Table 2-4 gives the water soluble alkali and alkaline metals portion of the deposits only. These are all sulfates. Taking the 1500 °F data as a base line, note that the soluble alkali metals are enriched in the deposits on the cooled pins. Ca and Mg are not enriched on cooled pins. Table 2-5 shows the total concentration of alkali in these deposits. Subtracting the water soluble portion from the total (acid soluble) gives the water insoluble portions which constitute oxides and silicates. The insoluble portions of alkali do not show an enrichment in the deposits on the cooler pins. Insoluble Ca, however, does show an enrichment. This result could be caused by taking the difference between large numbers which are not known with sufficient precision.

One explanatory source for the enrichment of the alkali sulfate compounds is that only these species are vaporized, and presumably only these species are in a form that is affected by the cooling of the metal below the gas temperature. It is known that the collection of condensible vapors and submicron particles is enhanced by cooling surfaces to temperatures below the surrounding gas temperature.

In general, the LVTS deposits were a mixture of flyash and calcined and sulfated dolomite. Over 99.9% of all water soluble components in the deposits were sulfates. Chlorides were present in all deposits at the ppm level.

It is the alkali sulfates which are responsible for hot corrosion, namely the water soluble alkali. Generally alkali levels in a deposit above 1% are thought to be of concern as corrosion may occur. Of course, as noted in Tables 2-4 and 2-5, significant fractions of the alkali were only present in acid soluble structures (silicates). In this form they are not believed to be corrosive because they probably do not contribute to the salt melt at the temperatures in the LVTS. Corrosion rates for the pins in the LVTS of the LTMT program were about 1 to 5 mils per thousand hours.

It should be noted that the deposits encountered in the LVTS differ from the usual gas turbine deposits in that they contain large amounts of K_2SO_4 relative to Na_2SO_4. The addition of K_2SO_4 to Na_2SO_4 causes a significant reduction in the salt melting point. As the work will show in Task 2 the presence of K_2SO_4 increases the stability of $CoSO_4$ and hence increases the range of what is called low-temperature hot corrosion.

2.3 PFB/LTMT CORROSION MORPHOLOGIES

2.3.1 IN-738

Selected specimens from the Long-Term Materials Test Program*† (LTMT) have undergone metallographic and microprobe examination. Two photomicrographs are shown for the alloy IN-738 for the purposes of comparison with the structures obtained in the first air-cooled small burner rig (ACSBR) test.

Figures 2-2 and 2-3 show corrosion specimens for 1500 and 1300 °F from the LTMT pressurized fluidized bed low-velocity test section, and Figures 2-4 and 2-5 show corrosion specimens from the ACSBR (see Task 3). Times in test differ greatly - 5785 hours and 3098

*R.L. McCarron and R.P. Brobst, Gas Turbine Blade Materials' Corrosion in the Effluent from a Pressurized Fluidized Bed Combutor, ASME 84-GT-208

†Long-Term Materials Test Program, Final Report Dec. 1984, Contract DE-AC21-79ET15457

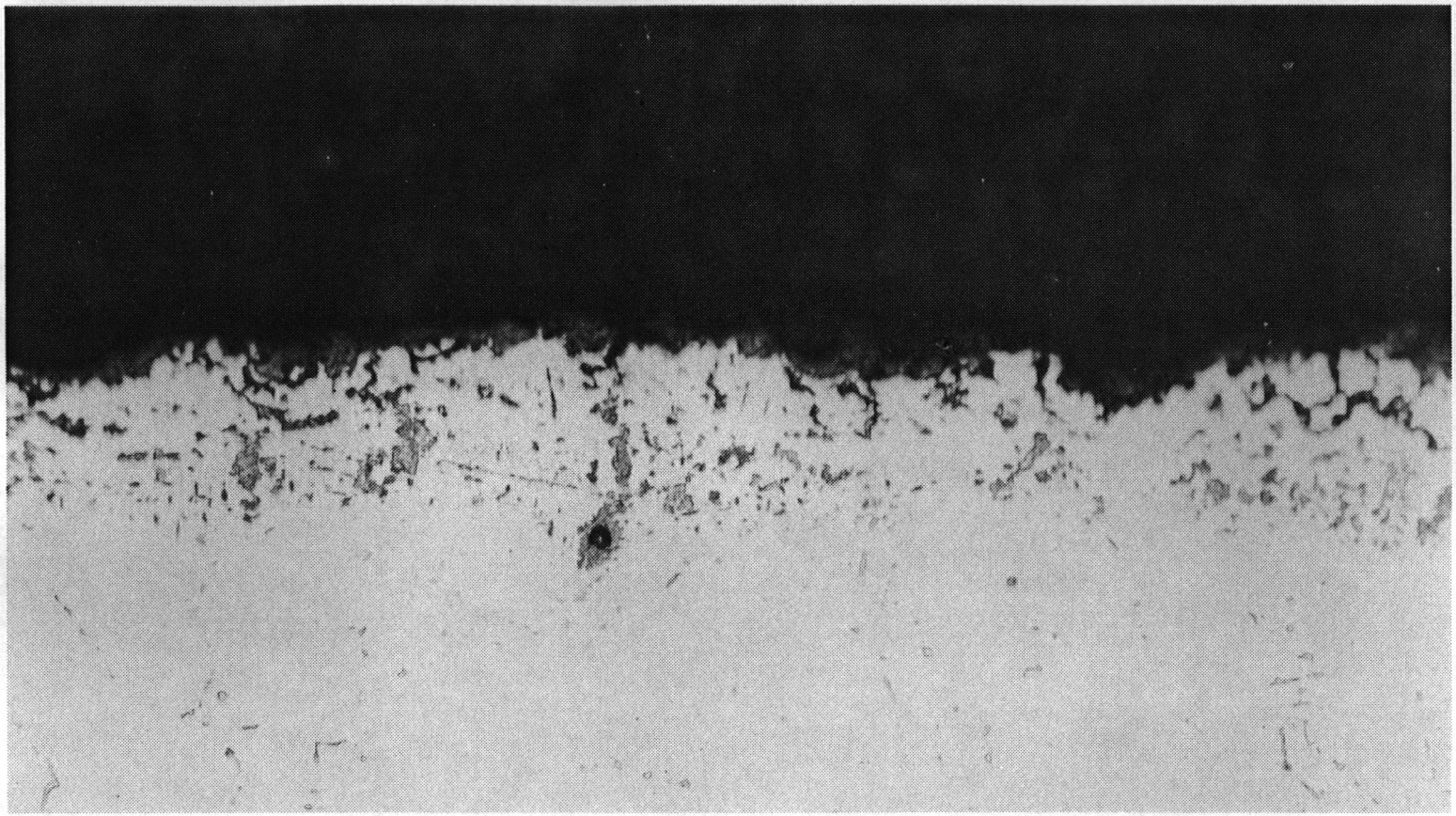

Figure 2-2. **Low-Temperature Corrosion Study, Specimens from LTMT IN-738, 1500 °F, 400X, As Polished.**

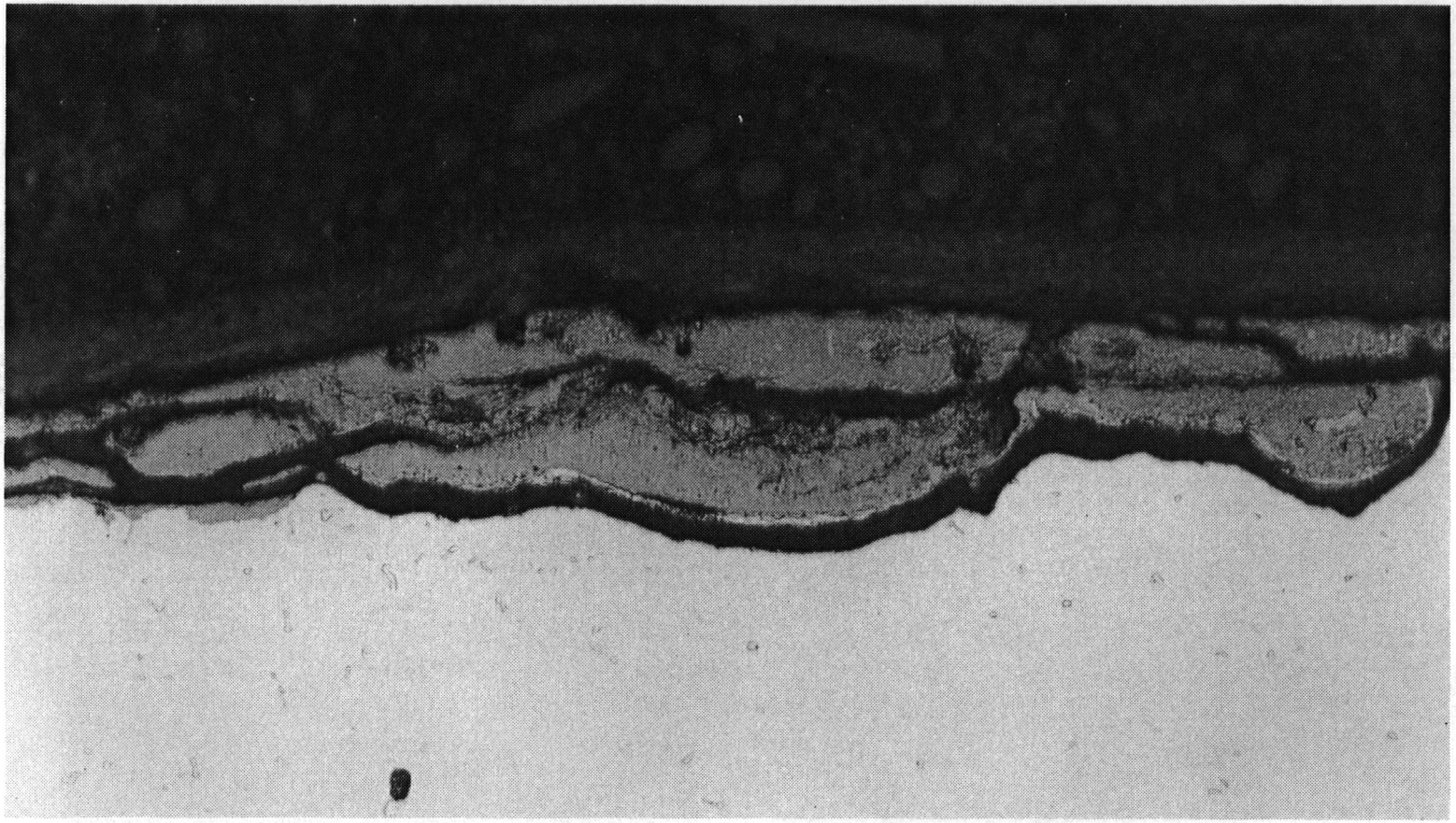

Figure 2-3. **Low-Temperature Corrosion Study, Specimens from LTMT IN-738, 1300 °F, 400X, As Polished.**

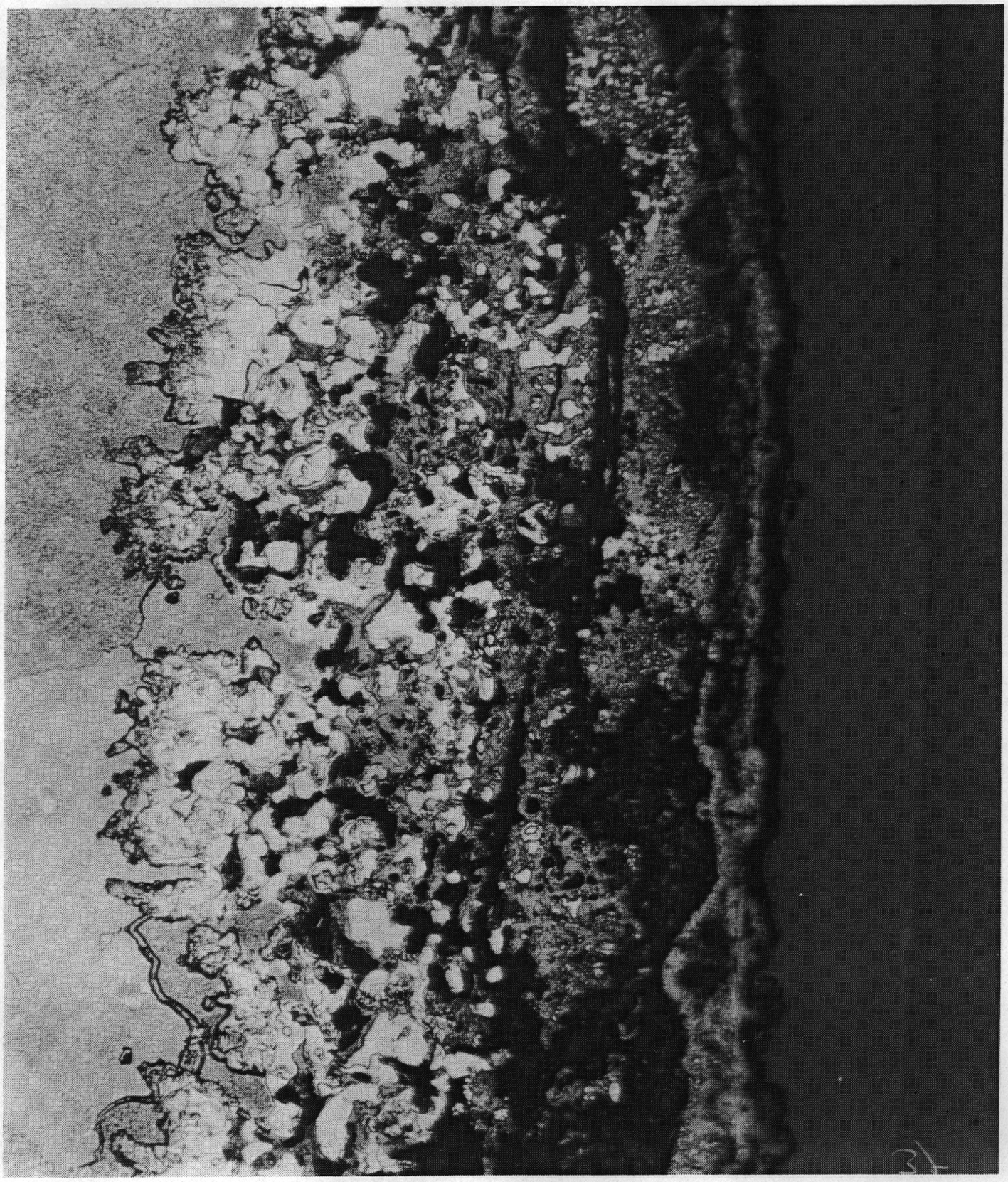

Figure 2-4. **Low-Temperature Corrosion Study, Test No. 3, ACSBR 1500 °F, IN-738, 400X, As Polished.**

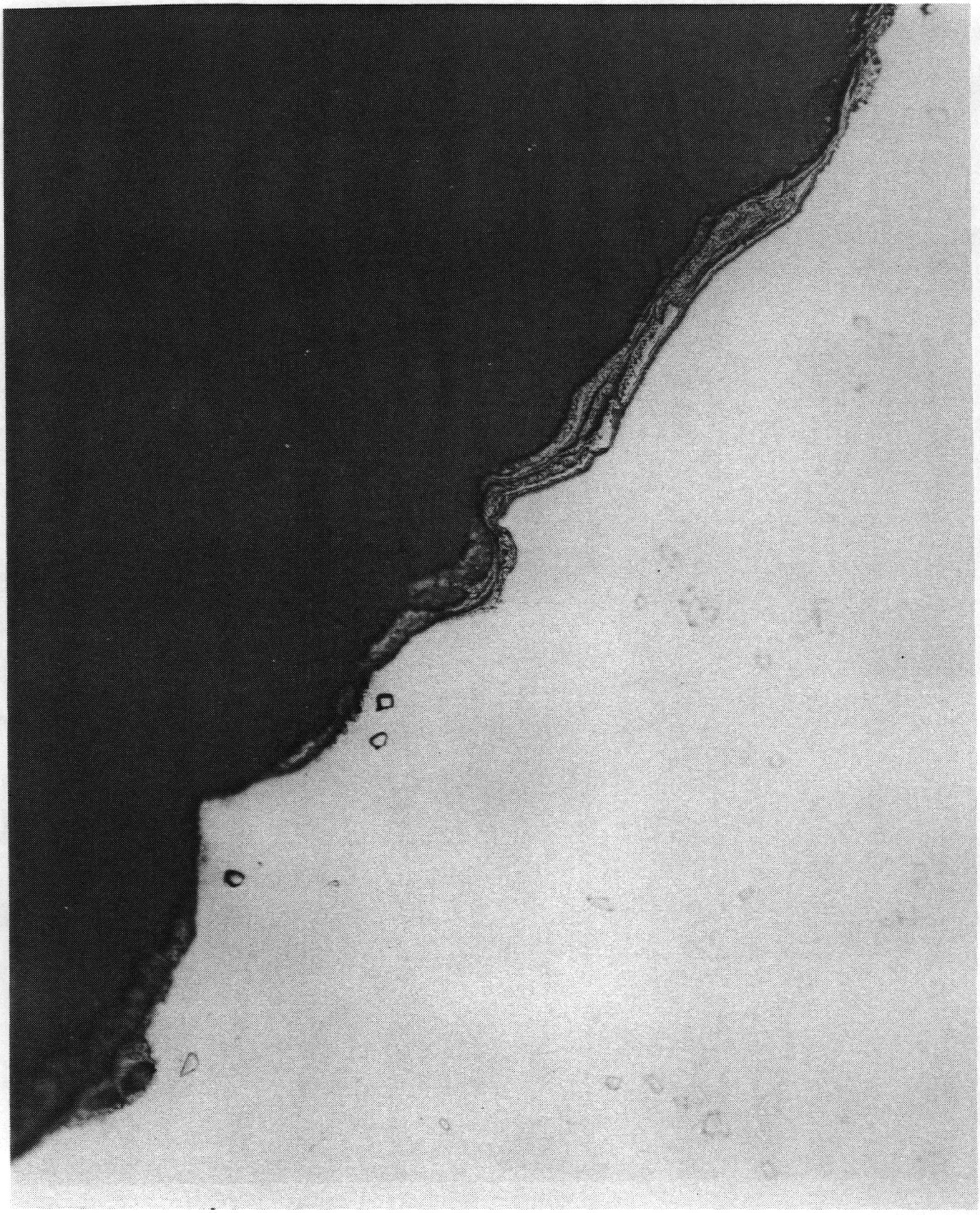

Figure 2-5. **Low-Temperature Corrosion Study, Test No. 1, ACSBR 1300 °F, IN-738, 400X, As Polished.**

hours for the 1500 °F and 1300 °F LTMT pins, respectively, and 217 hours for the ACSBR specimens, but the corrosion structures show similarities, especially the lower temperature ones. The 1300 °F specimens show a dense oxide layer and no internal attack, whereas the 1500 °F specimens show internal attack. For the ACSBR 1500 °F specimens, the internal structure probably contains more sulfides, indicative of higher SO_x pressures present in the ACSBR. Of course corrosion rates in the ACSBR are higher than were seen during the LTMT because of the much higher alkali levels in the ACSBR test.

Microprobe spectra have been taken on the IN-738 [Ni(bal), Co(8.5), Cr(16), AL(3.4), Ti(3.4), Mo(1.75), W(2.6), Cb(0.9) Ta(1.75)] specimens from the LTMT-PFB. In Figures 2-2 and 2-3 the corrosion morphologies for the 1500 °F and 1300 °F specimens, respectively, were shown. Figure 2-6a shows the spectra of the IN-738 matrix, and Figure 2-6b shows the spectra for the corrosion product at the combustion gas-scale interface. It is observed that the corrosion product is primarily Al oxide rich with Al > Ti > Cr. Probe spectra of the corrosion product further into the alloy showed little change in this spectra. For the 1300 °F specimen, the spectra near the scale-combustion gas interface are shown in Figure 2-7a, and near the scale-matrix interface in Figure 2-7b. Of course the 1300 °F specimen shows the low-temperature corrosion structure as shown in Figure 2-3, having no internal structure. But there are gradients in the scale. The scale near the gas interface is high in Cr with lesser amounts of Ti and Al. This scale is mostly oxide. The scale near the matrix interface is high in Cr, Ti, and Al also but contains sulfides. It should be noted that at 1500 °F the IN-738 forms an Al-rich scale whereas at 1300 °F the scale contains considerable Cr.

One of the interesting features of the low-temperature structure is the presence of sulfides at the bottom of the corrosion scale. For the 1300 °F IN-738 pin, the electron image in Figure 2-8a indicates that the region at the bottom of the scale is rich in sulfides. This is also shown in the sulfur map in Figure 2-8b. Figures 2-9a and 2-9b are maps for Ni and Cr, respectively. There seems to be a gap between the metal matrix and the bottom of the scale. All of the sulfides appear to be confined to the scale side of the gap. There are some bands in the scale, however, which also contain high concentrations of sulfides. For higher temperatures specimens, it has been observed that the sulfides appear in the metal matrix as internal precipitates. Ni increases near the bottom of the corrosion scale, and probably the Cr decreases. This became more obvious when spectra were taken in the high Ni and low Ni regions near the bottom of the scale (see Figures 2-9c and 2-9d). Note that Co is almost absent from the low-temperature scale, although it may be slightly enhanced in the high sulfide region at the bottom of the scale. Some Al is present in the low-temperature scale, but much less than in the high-temperature scale. There may also be some enhancement of Al near the bottom of the scale where the sulfides appear.

2.3.2 FSX-414

Specimens of the cobalt base alloy FSX-414 [Ni(10), CR(29), Fe(1), W(7.5)] at 1500 °F and 1300 °F were also studied. The 1100 °F alloy showed no corrosion. Figures 2-10 and 2-11 show the corrosion structures at 1500 °F and 1300 °F, respectively. The outer oxide scale at 1500 °F is high in Cr and contains the matrix elements Co and W. The light-colored internal precipitates are also rich in Cr and are oxides. The dark precipitates follow grain boundaries, are rich in Cr and W, and contain sulfides. Figure 2-12a shows the x-ray spectra for the outer scale. Figures 2-12b and 2-12c show the spectra of the light-colored scale and the dark-colored precipitates, respectively.

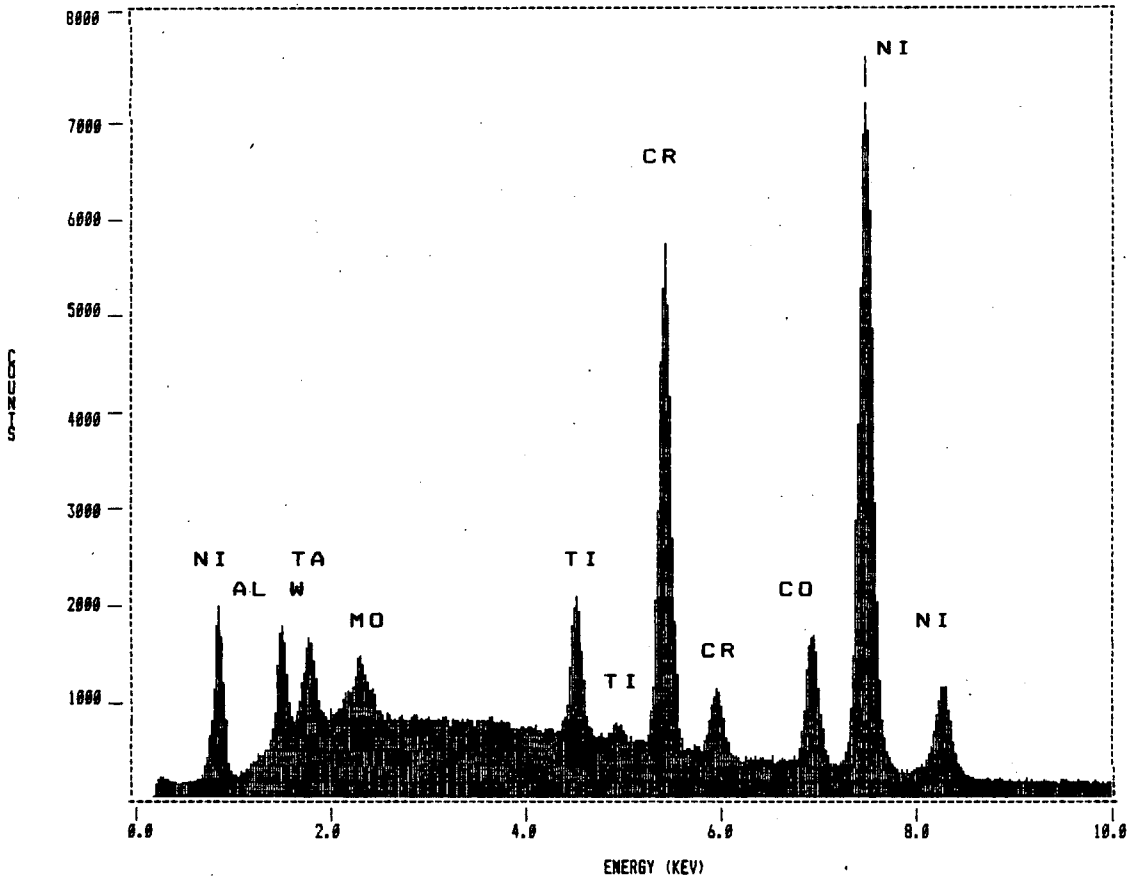

Figure 2-6a. Microprobe Spectra, IN-738: Matrix.

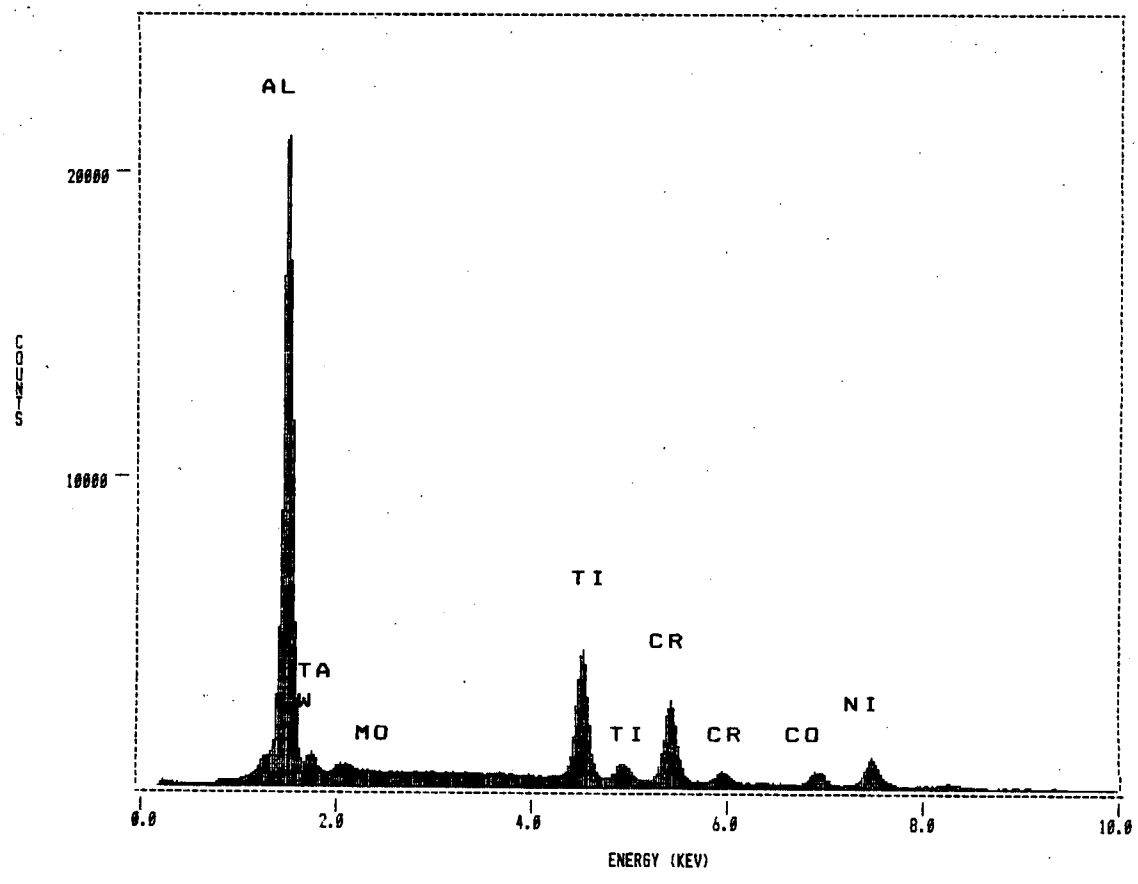

Figure 2-6b. Microprobe Spectra, IN-738: Corrosion Scale, 1500 °F Specimen.

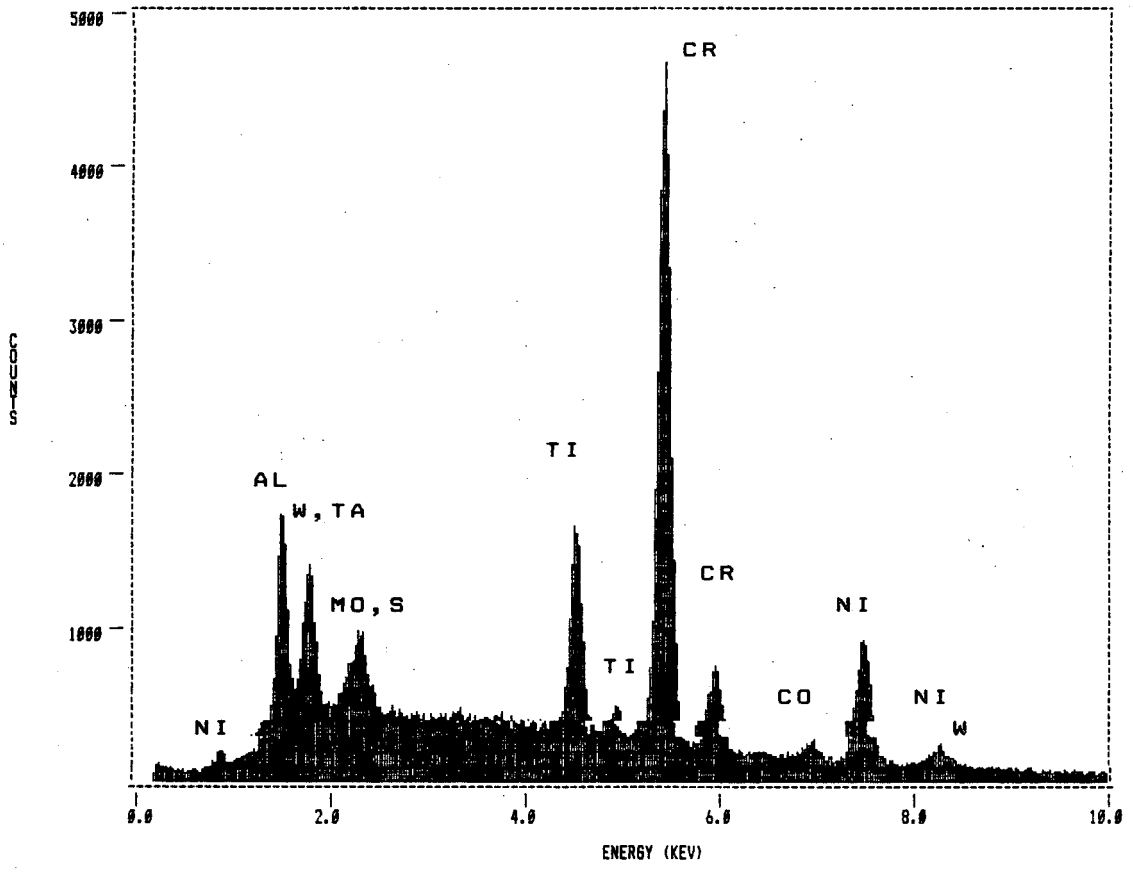

Figure 2-7a. Microprobe Spectra, IN-738: Outside Scale, 1300 °F Specimen.

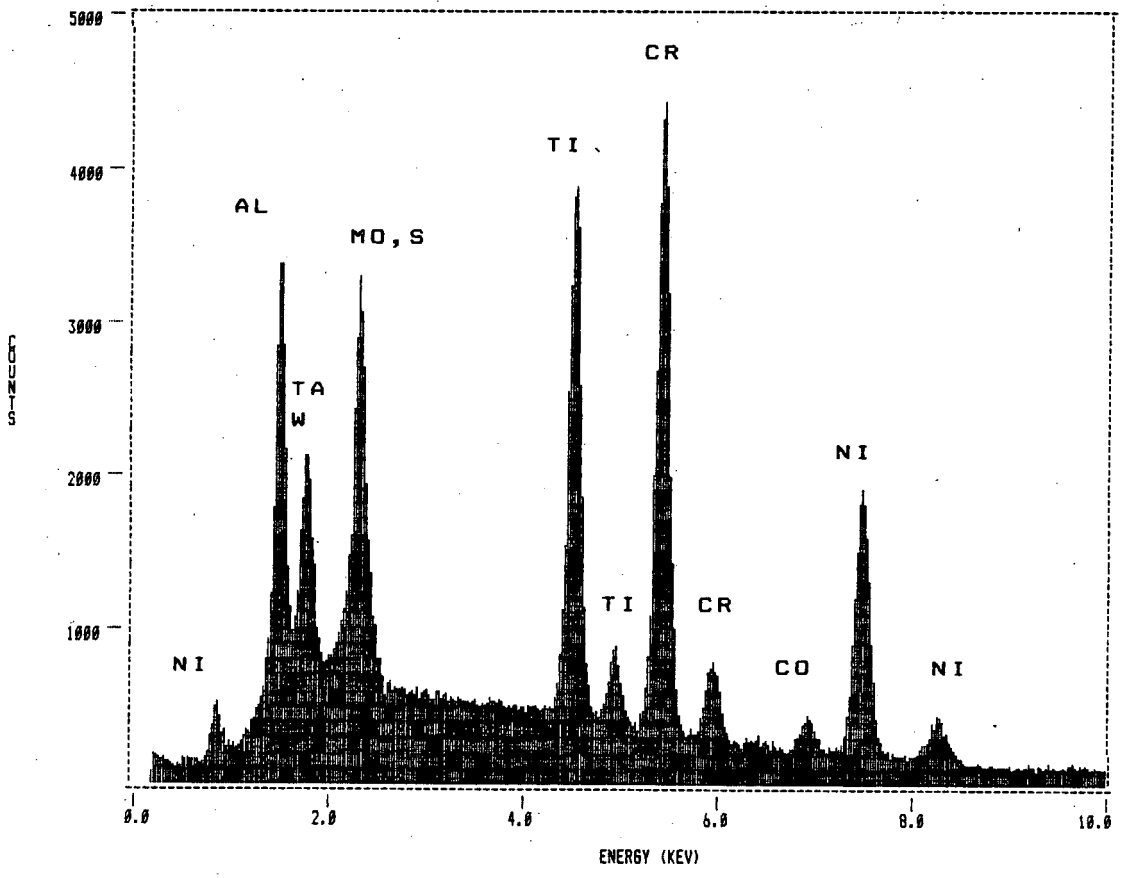

Figure 2-7b. Microprobe Spectra, IN-738: Corrosion Near Matrix, 1300 °F Specimen.

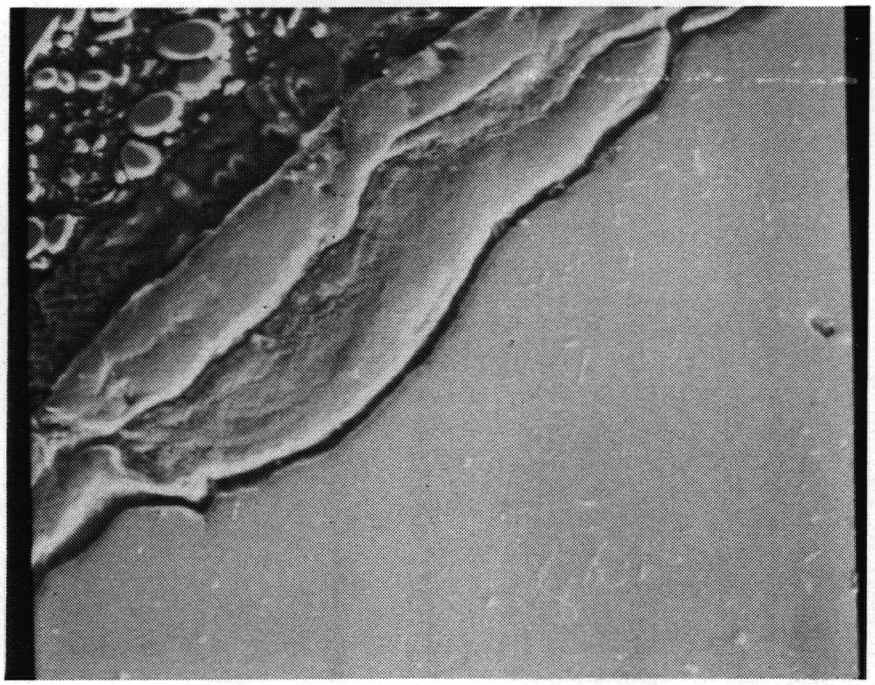

Figure 2-8a. Electron Image, 400X, LTMT 1300 °F, Pin, IN-738.

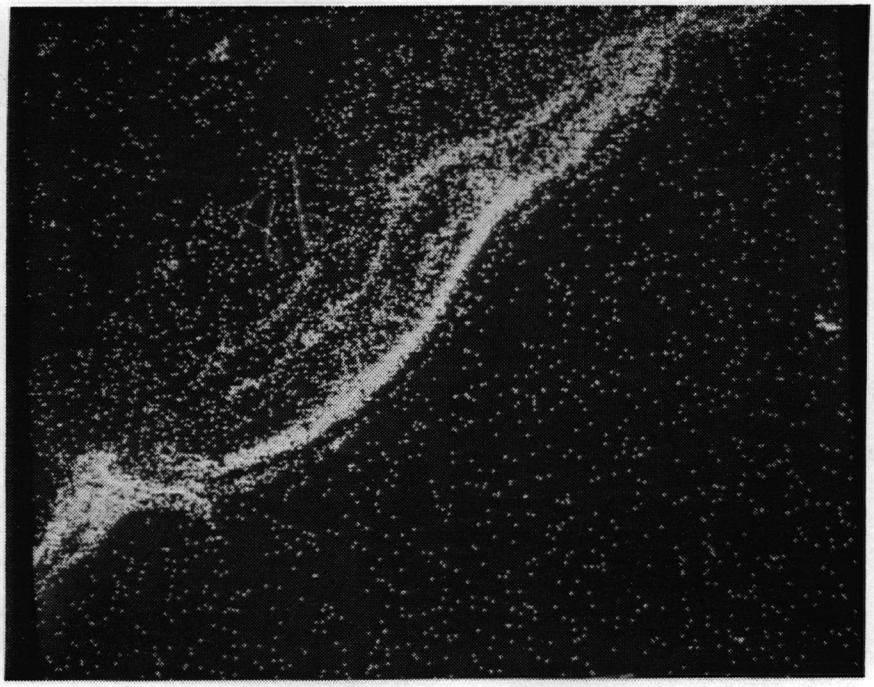

Figure 2-8b. Sulfur Map, 400X, LTMT 1300 °F, Pin, IN-738.

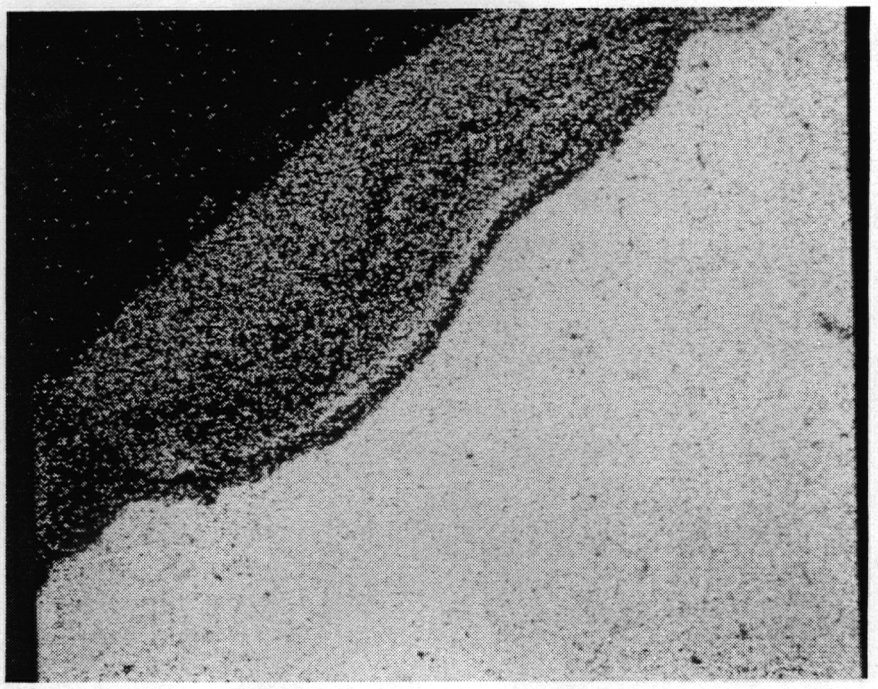

Figure 2-9a. Nickel Map, 400X, LTMT, 1300 °F Pin, IN-738.

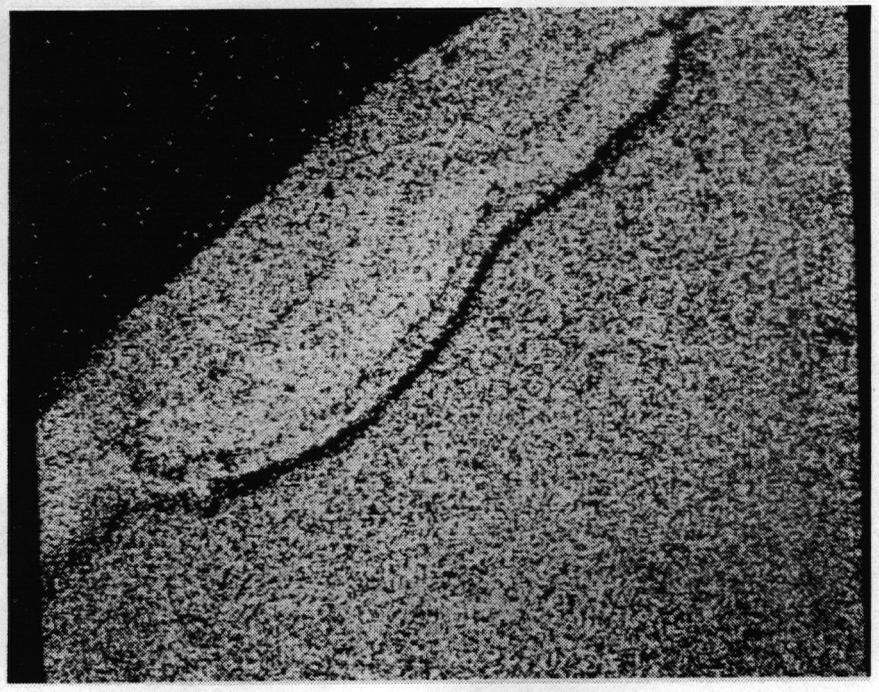

Figure 2-9b. Chromium Map, 400X, LTMT, 1300 °F Pin, IN-738.

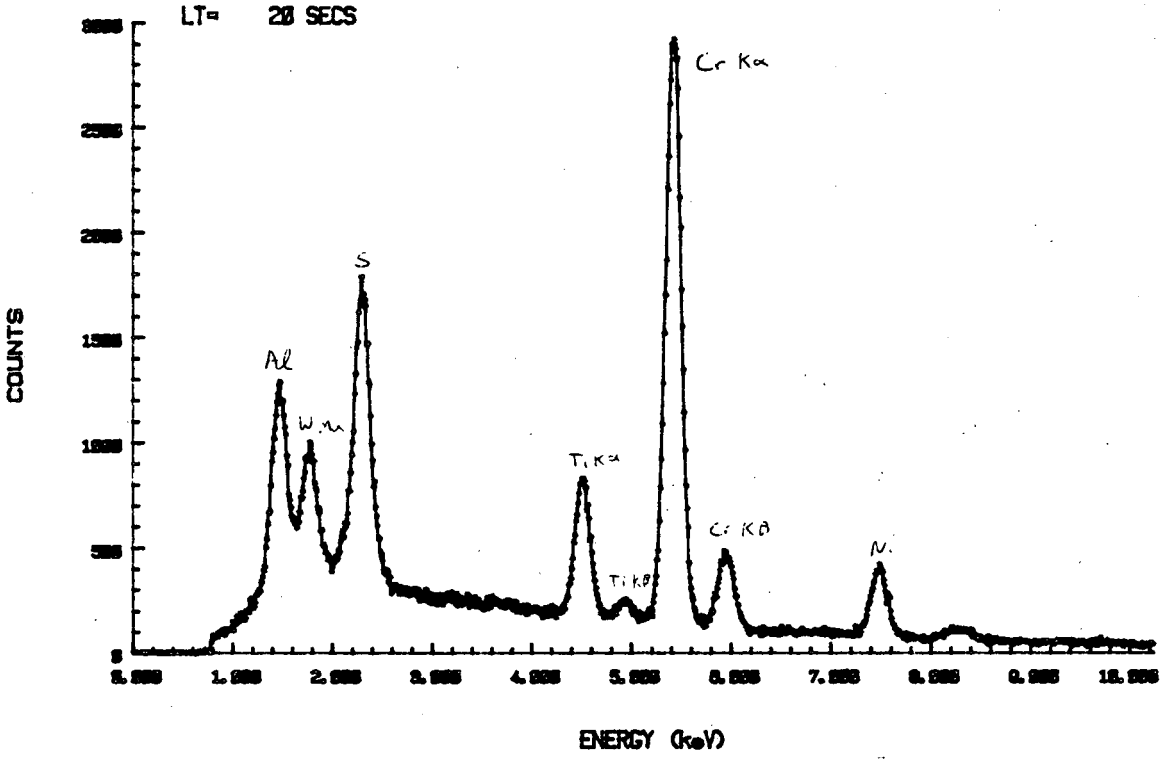

Figure 2-9c. IN-738 Low Ni/S Area

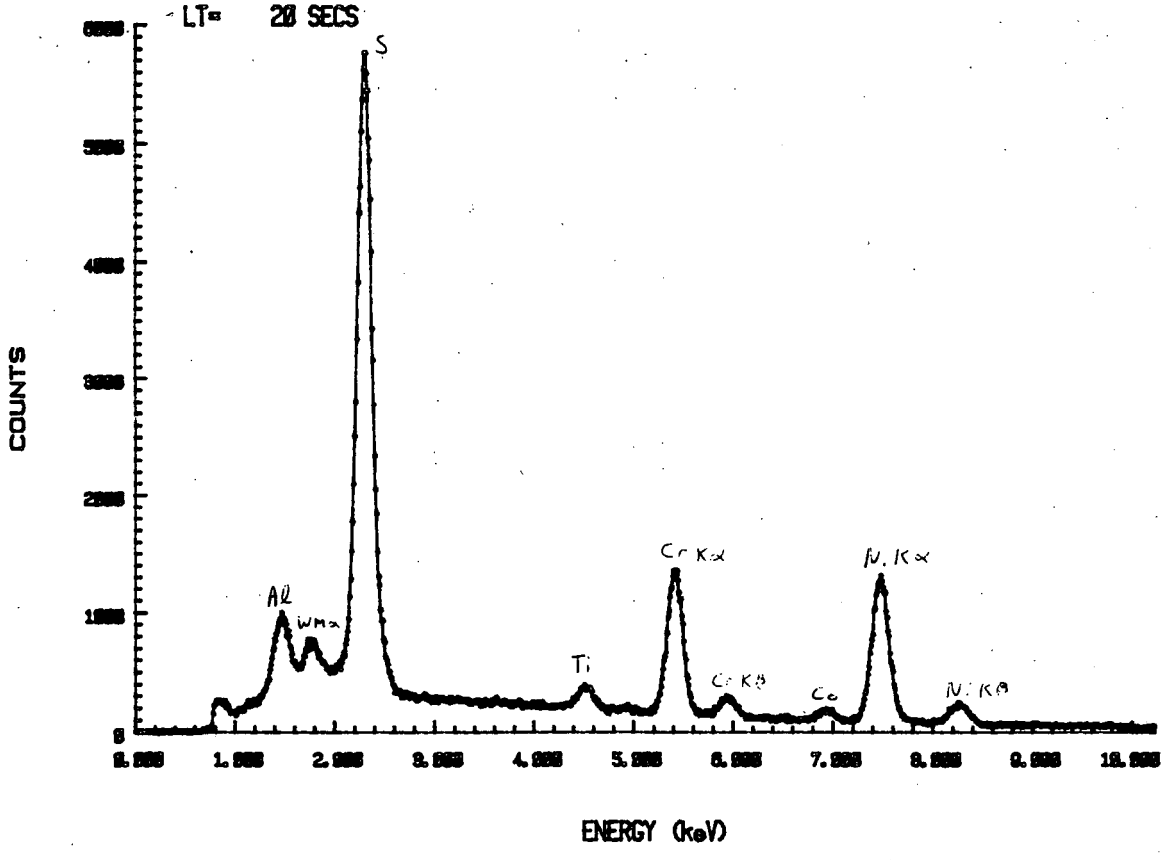

Figure 2-9d. IN-738 High Ni/S Area

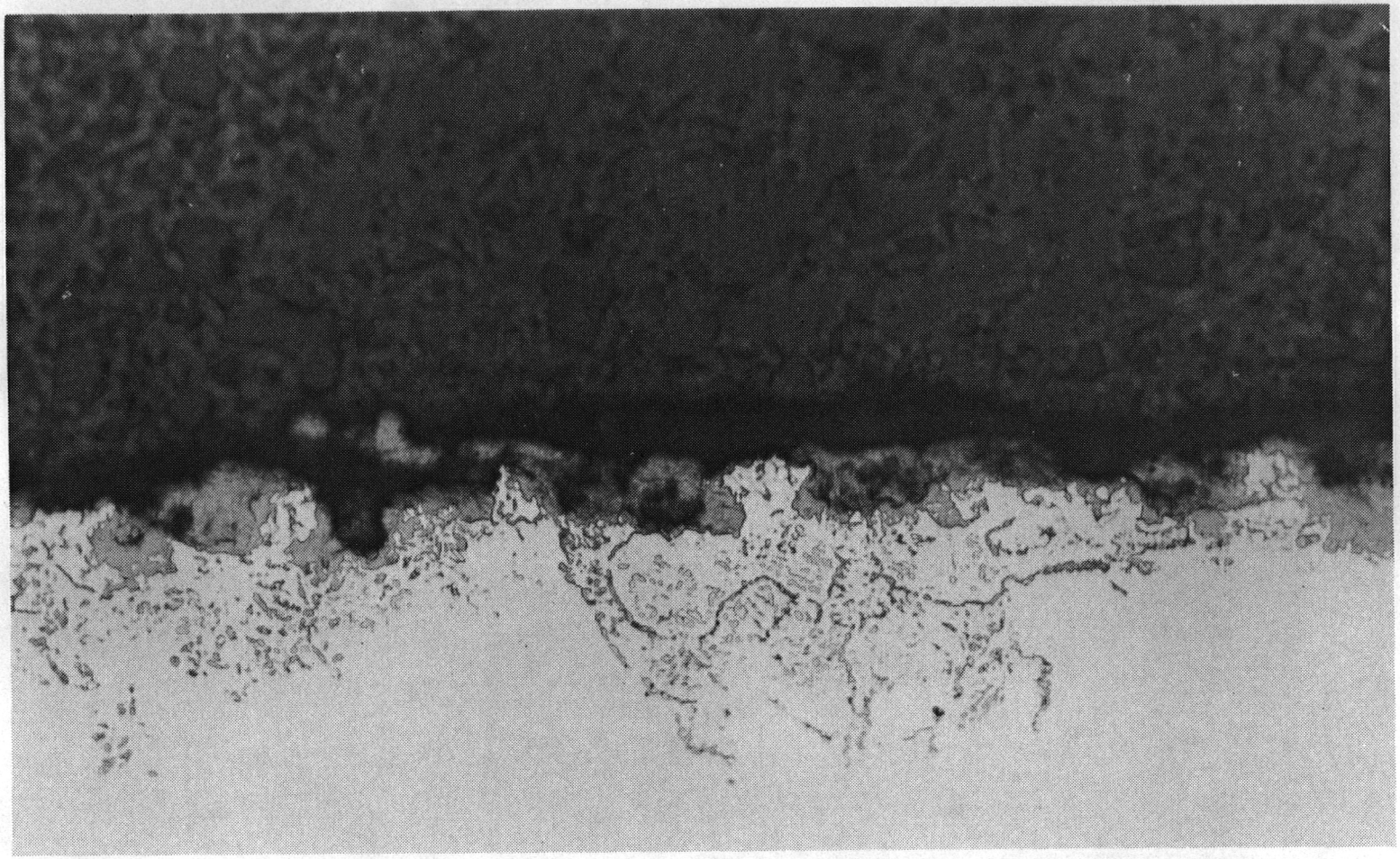

Figure 2-10. **Specimen from LTMT, FSX-414, 1500 °F, As Polished.**

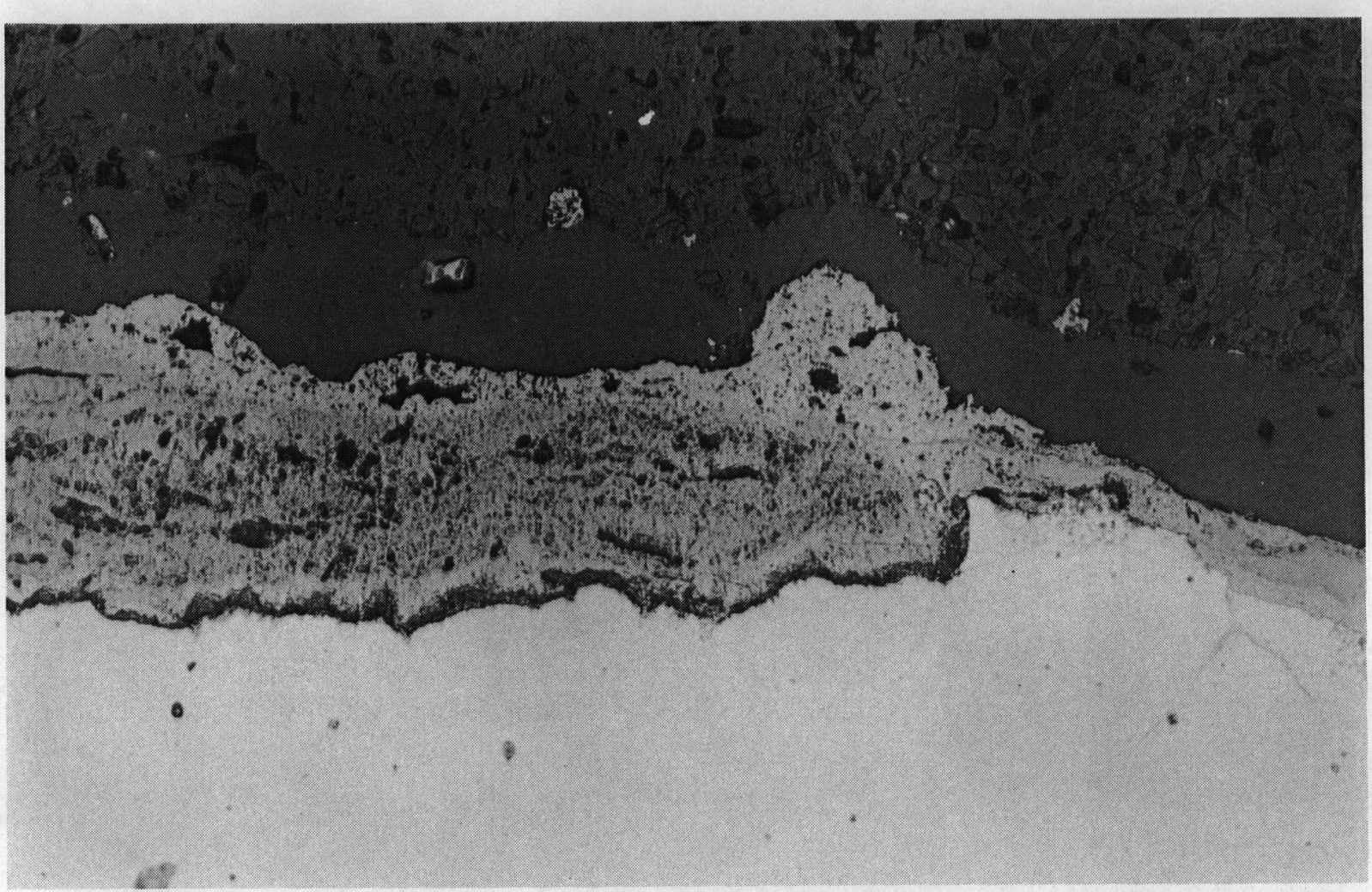

Figure 2-11. Specimen from LT-MT, FSX-414, 1300 °F, As Polished

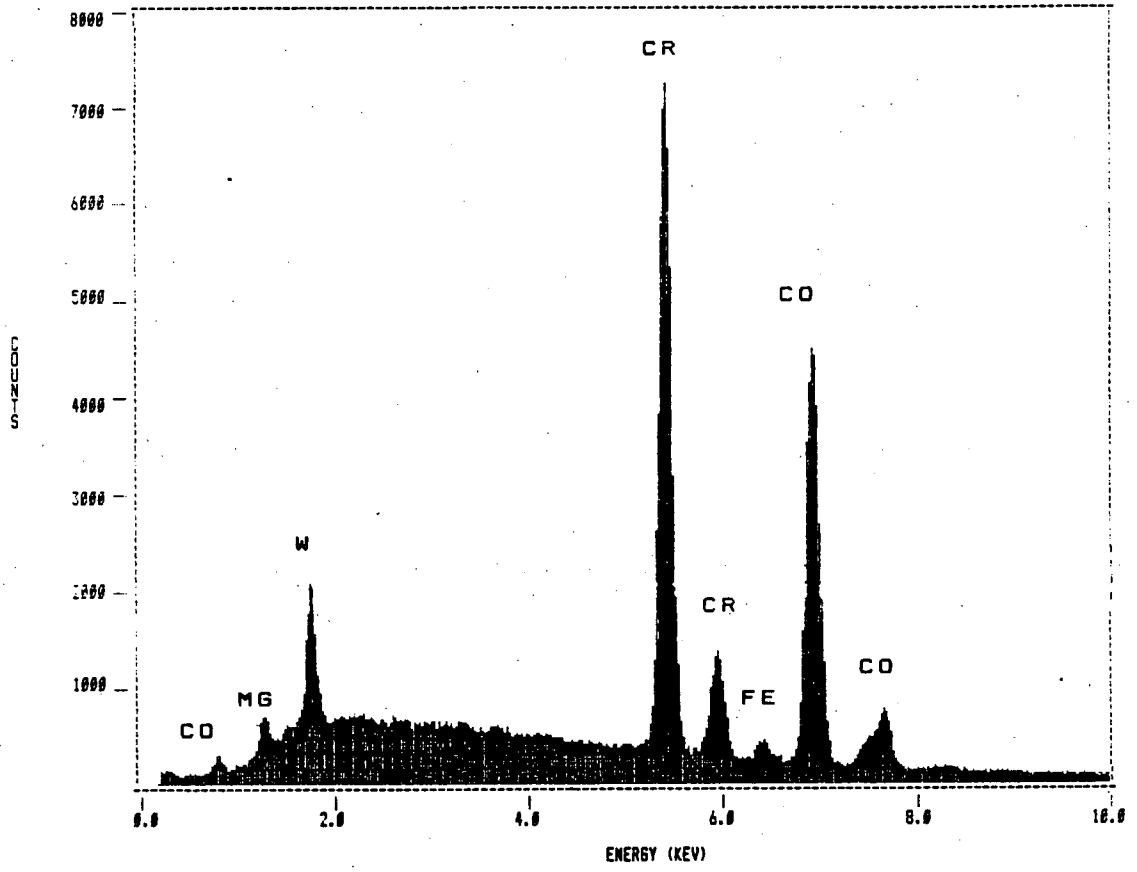

Figure 2-12a. Microprobe Spectra, Outer Scale FSX-414, 1500 °F.

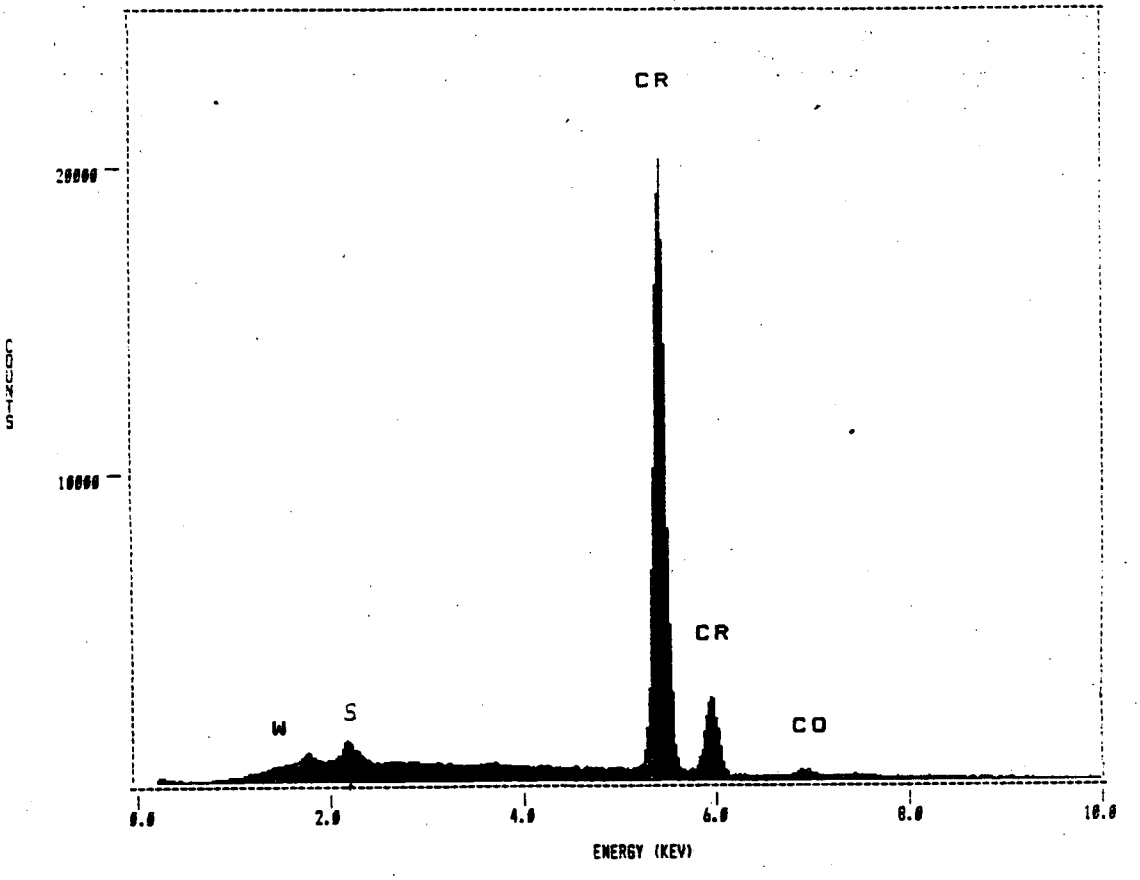

Figure 2-12b. Microprobe Spectra, Light-Colored Internal Precipitate, FSX-414, 1500 °F.

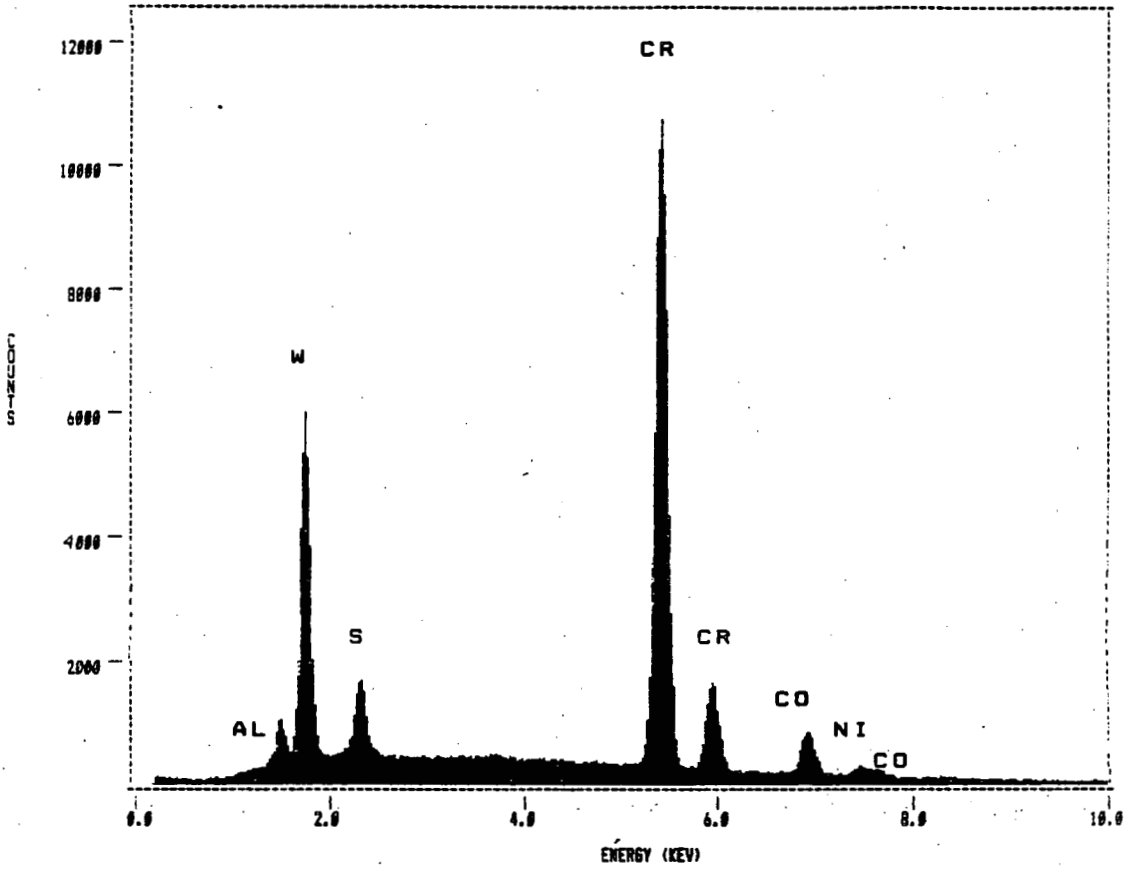

Figure 2-12c. **Microprobe Spectra, Dark-Colored Grain Boundary Precipitate, FSX-414, 1500 °F.**

The 1300 °F corrosion morphology is typical of the low-temperature type. This porous duplex scale is part of a shallow pit. The current image for the specimen is given in Figure 2-13a. Again, as for IN-738, the sulfides are confined to a band just at the bottom of the corrosion scale as shown in Figure 2-13b. An interesting feature of the FSX-414 scale is that the darker portion on top is nearly pure Co oxide, whereas beneath this is a scale that is largely Cr oxide. This feature is shown in Figures 2-14a and 2-14b. The outer Co oxide scale is thought to be a result of precipitation from the salt melt. The sulfides in this scale appear to be associated almost entirely with Cr. The Ni, a map of which is shown in Figure 2-14c, appears to be associated with Co. It was found the W followed Cr.

The corrosion scale to the right of the shallow pit in Figure 2-11 showing the grain boundary precipitate, contains Cr and Co oxides. Sulfides are present, particularly along the grain boundary, the metal-scale interface, and the fine internal precipitates.

2.3.3 CoCrAlY over IN-738

The coated specimens evaluated included CoCrAlY over IN-738. The coating was produced by physical vapor deposition and had the nominal composition Co(bal), Cr(30), Al(5), Y(0.4). The specimen at 1500 °F showed no attack and was not evaluated. The corrosion microstructures of the specimens at 1300 °F and 1100 °F are shown in Figures 2-15 and 2-16. Both specimens show a typical pitting morphology associated with low-temperature hot corrosion. In addition, the 1300 °F specimen shows attack along a leader-type defect.

Microprobe evaluation has shown that the corrosion scale at the interface with the metal matrix is sulfide rich containing both Al and Cr. The sulfur map in Figure 2-17 for the pit in the 1100 °F specimen and the sulfur map in Figure 2-18 for the leader defect in the 1300 °F specimen show that the sulfur tends to segregate along the margin of the corrosion product. At higher temperatures, the sulfur is able to diffuse into the metal matrix along grain boundaries.

The structures sitting above the corrosion pits are interesting. In particular, the porous material above the pit in Figure 2-16 is found to contain mostly Co. It is believed this material is a precipitate of cobalt oxide. The cobalt in the coating dissolved in the sulfate melt and then precipitated later as the oxide in the liquid salt.

2.3.4 Platinum Aluminide IN-738

The next coating considered was the platinum aluminide, RT22. The coating is produced by applying a Pt plate to the base metal followed by an Al pack at about 1850 °F. The resultant structure puts considerable Pt on the outside of the coating (about 35 weight %) with the concentration falling off as the base metal is approached (about 5%). Figures 2-19, 2-20 and 2-21 give the microstructures of the specimens for the three test temperatures.

At 1500 °F, the coating was almost completely penetrated by corrosion in 5785 hours. The corrosion penetration was about 2.6 mils, just about the coating thickness. The outer scale was almost entirely Al oxide. Near the scale-alloy interface (see arrow in Figure 2-19), elements from the alloy were found as shown in the microprobe spectra given in Figure 2-22. No Pt was found in the scale.

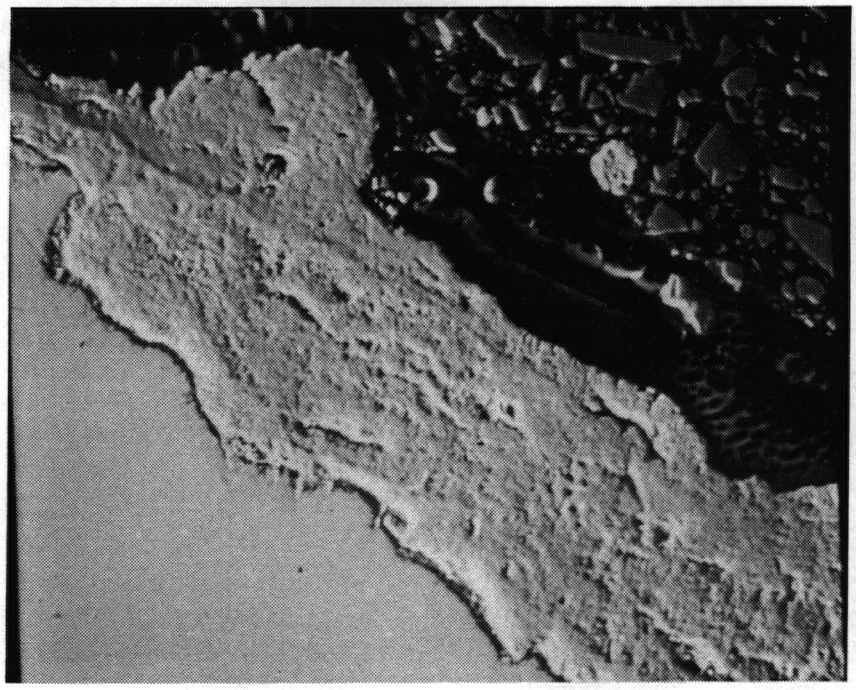

Figure 2-13a. Current Image, 400X, LTMT, 1300 °F Pin, FSX-414.

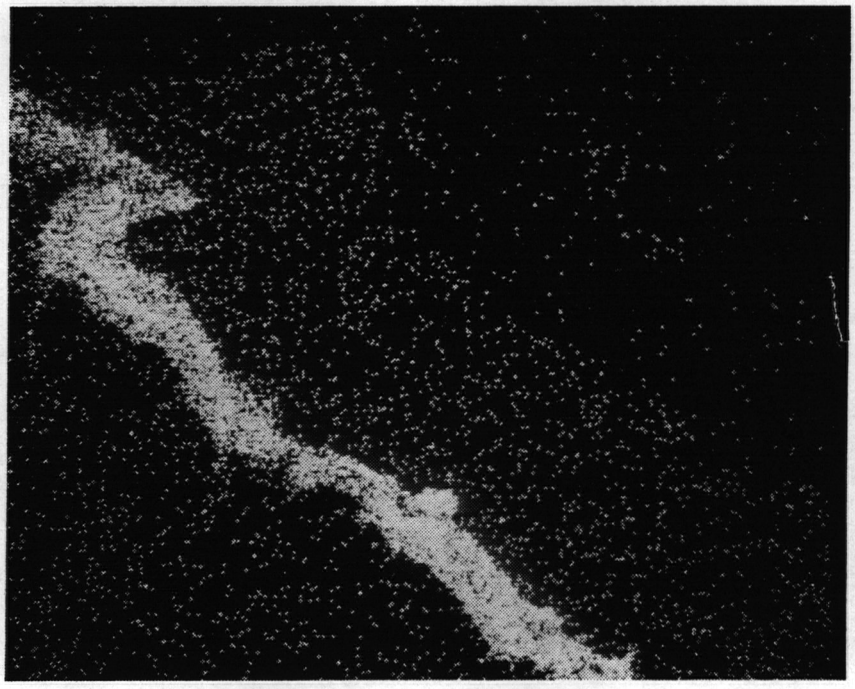

Figure 2-13b. Sulfur Map, 400X, LTMT, 1300 °F Pin, FSX-414.

Figure 2-14a. Cobalt Map, 400X LTMT, 1300 °F Pin, FSX-414.

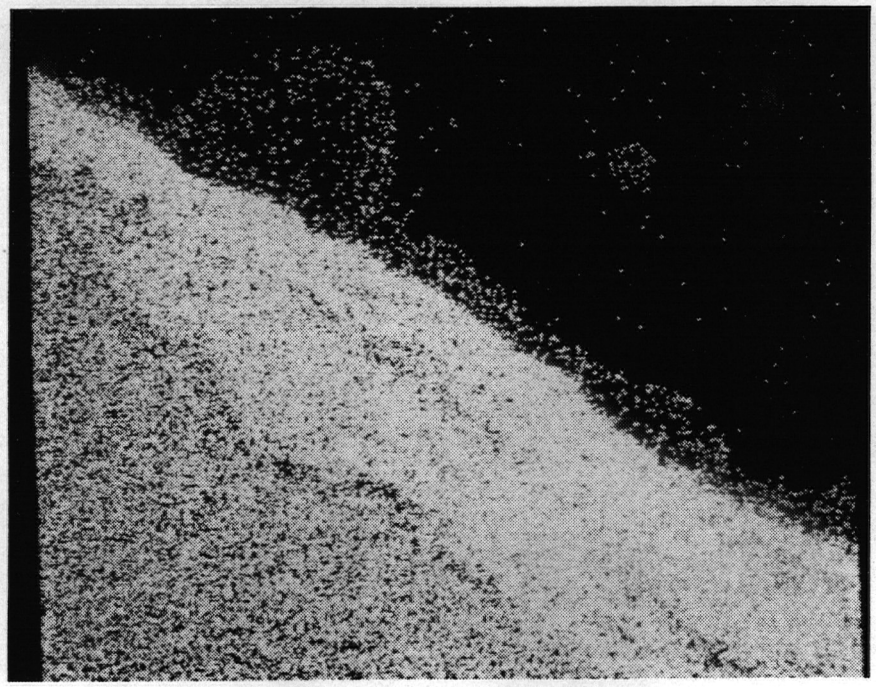

Figure 2-14b. Chromium Map, 400X, LTMT, 1300 °F Pin, FSX-414.

Figure 2-14c. Nickel Map, 400X, LTMT, 1300 °F Pin, FSX-414.

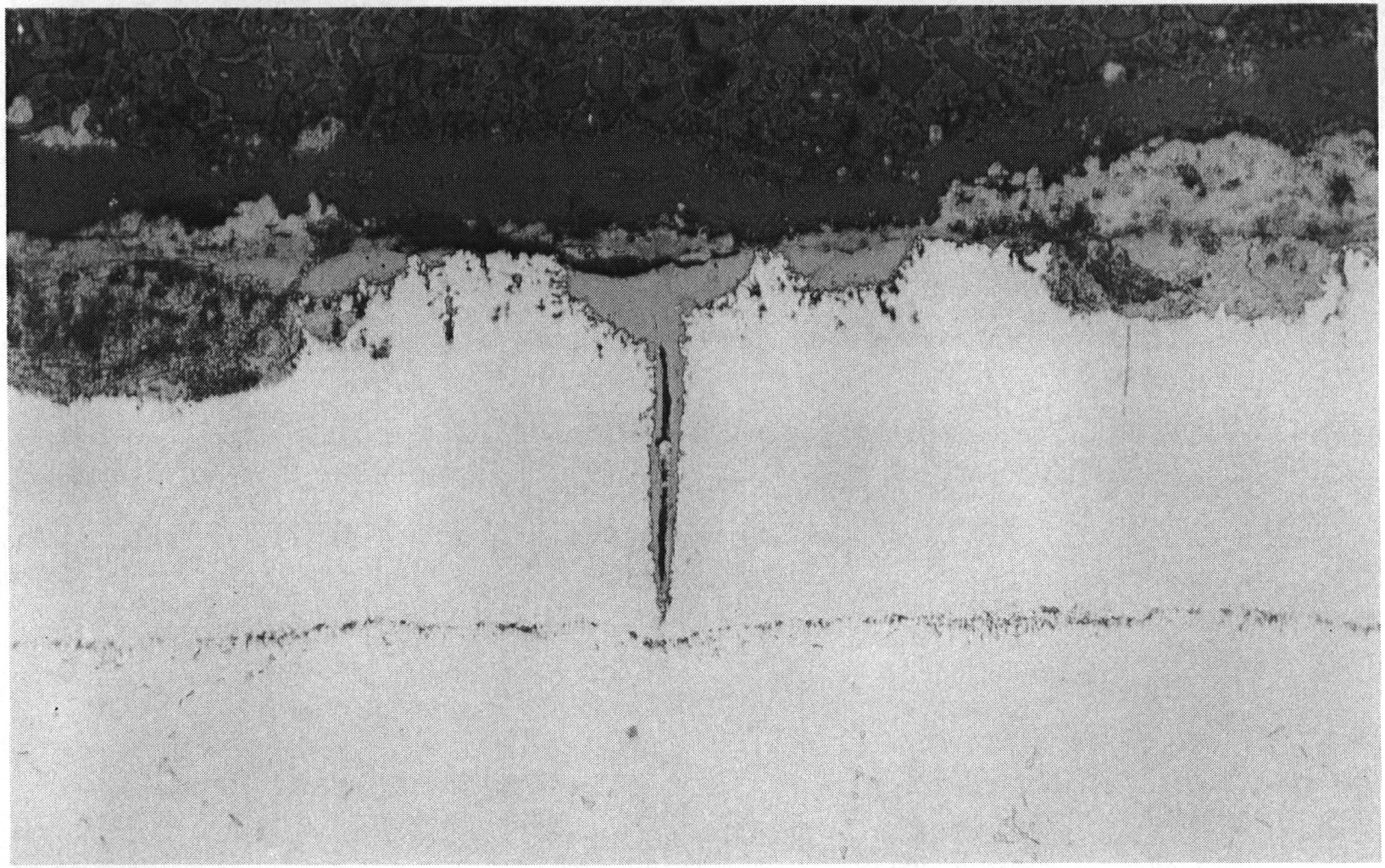

Figure 2-15. LTMT, CoCrAlY over IN-738, 1300 °F, 400X As Polished.

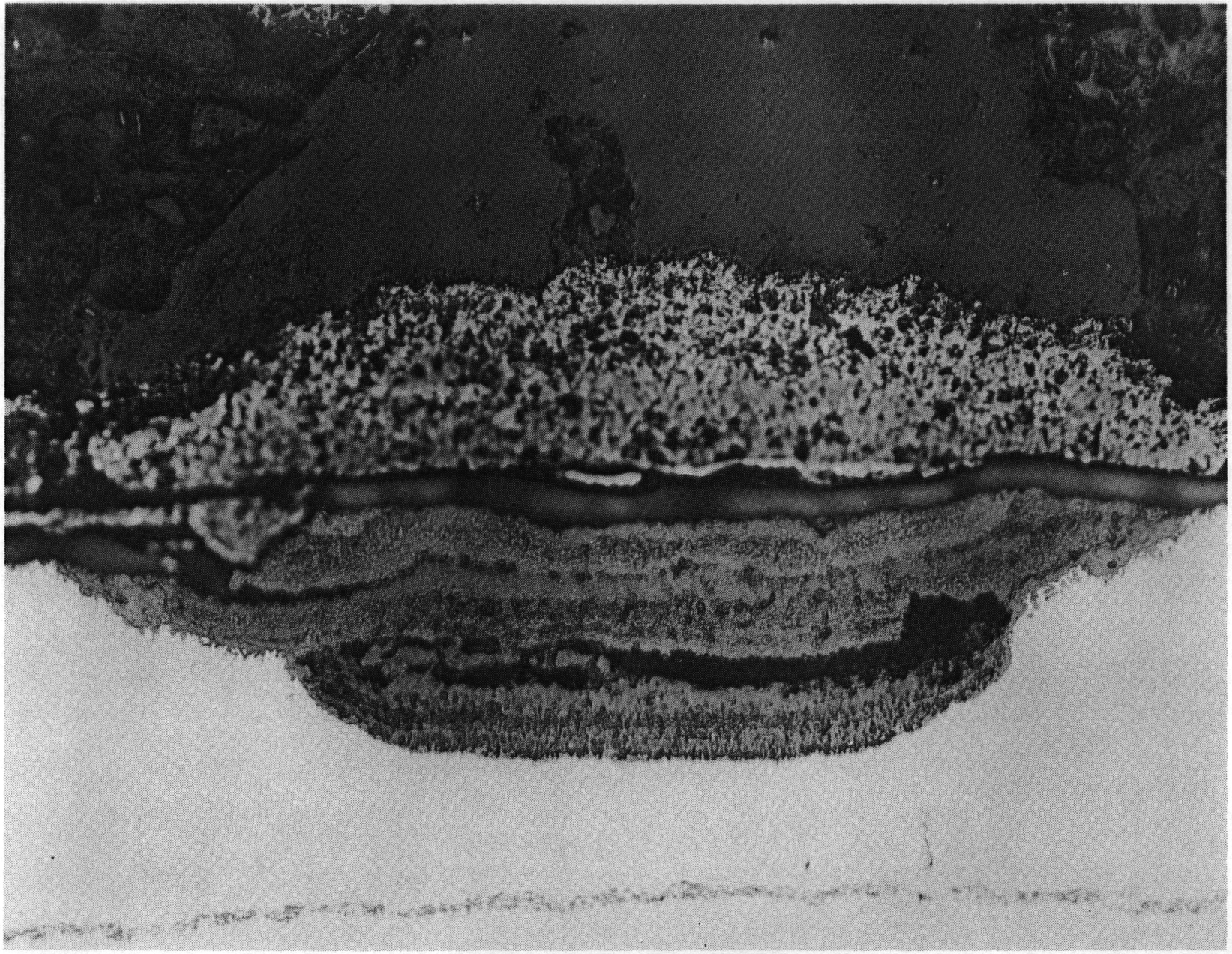

Figure 2-16. LTMT, CoCrAlY over IN738, 1100 °F, 400X As Polished.

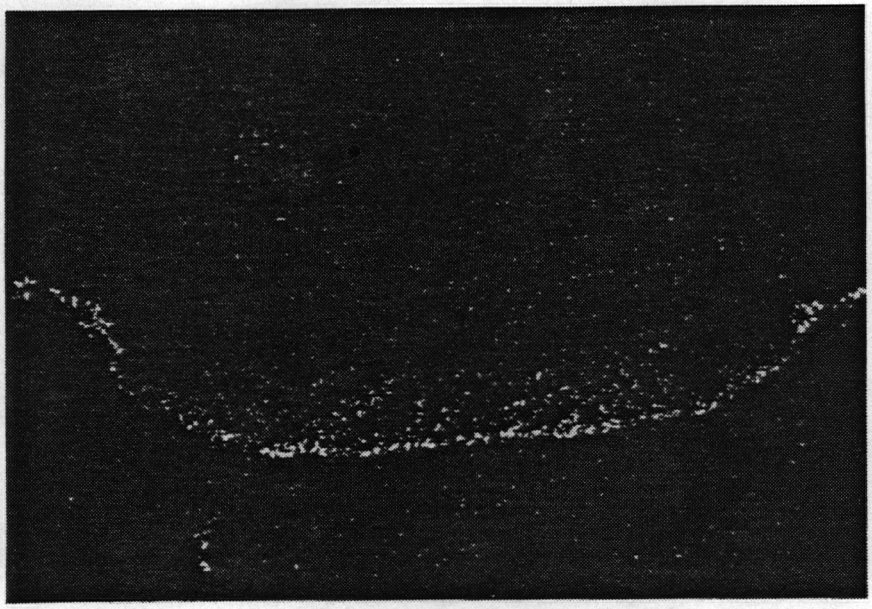

Figure 2-17. Sulfur Map, 1100 °F Specimen.

Figure 2-18. Sulfur Map, 1300 °F Specimen.

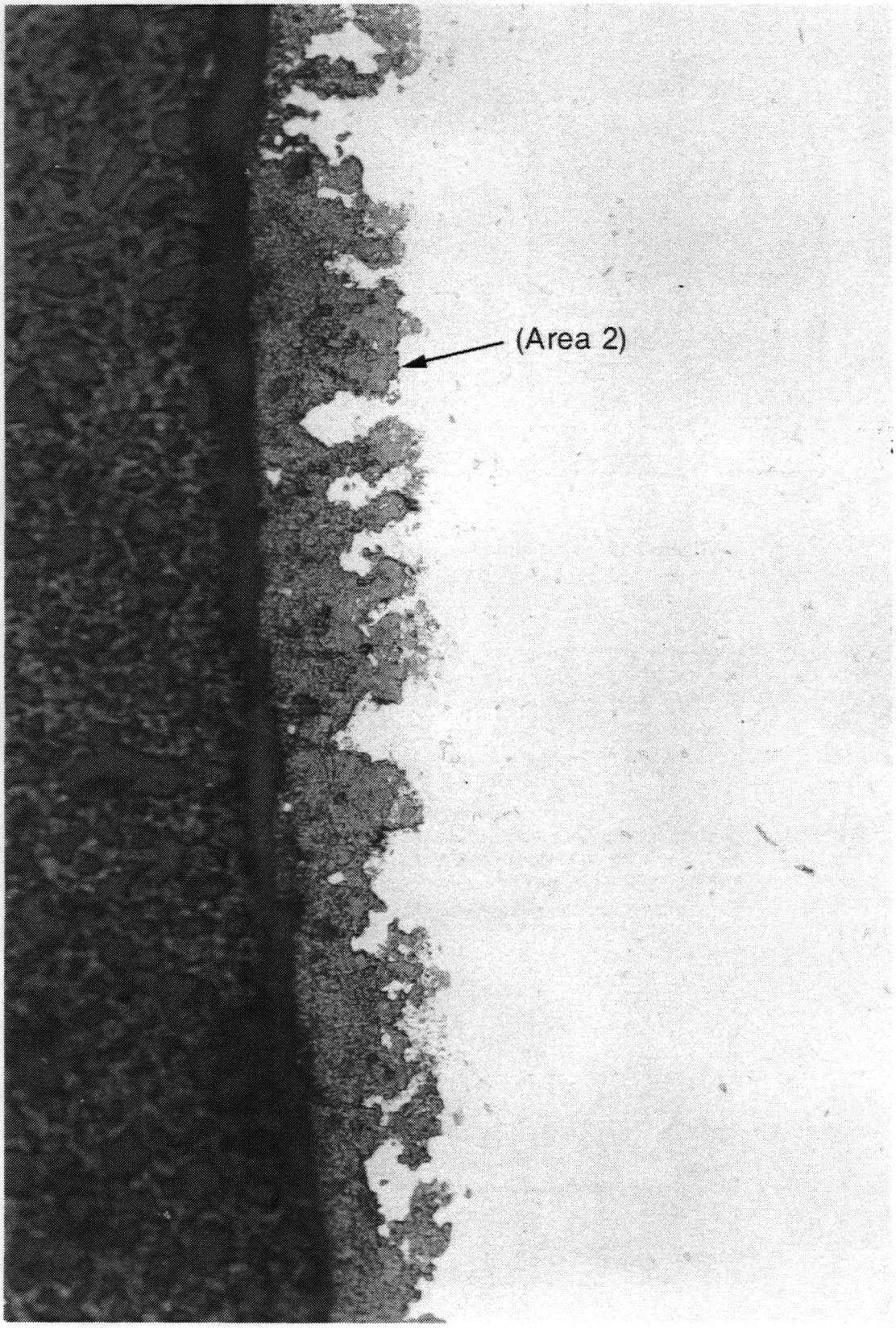

Figure 2-19. LTMT, RT22 over IN-738, 1500 °F, 400X, As Polished.

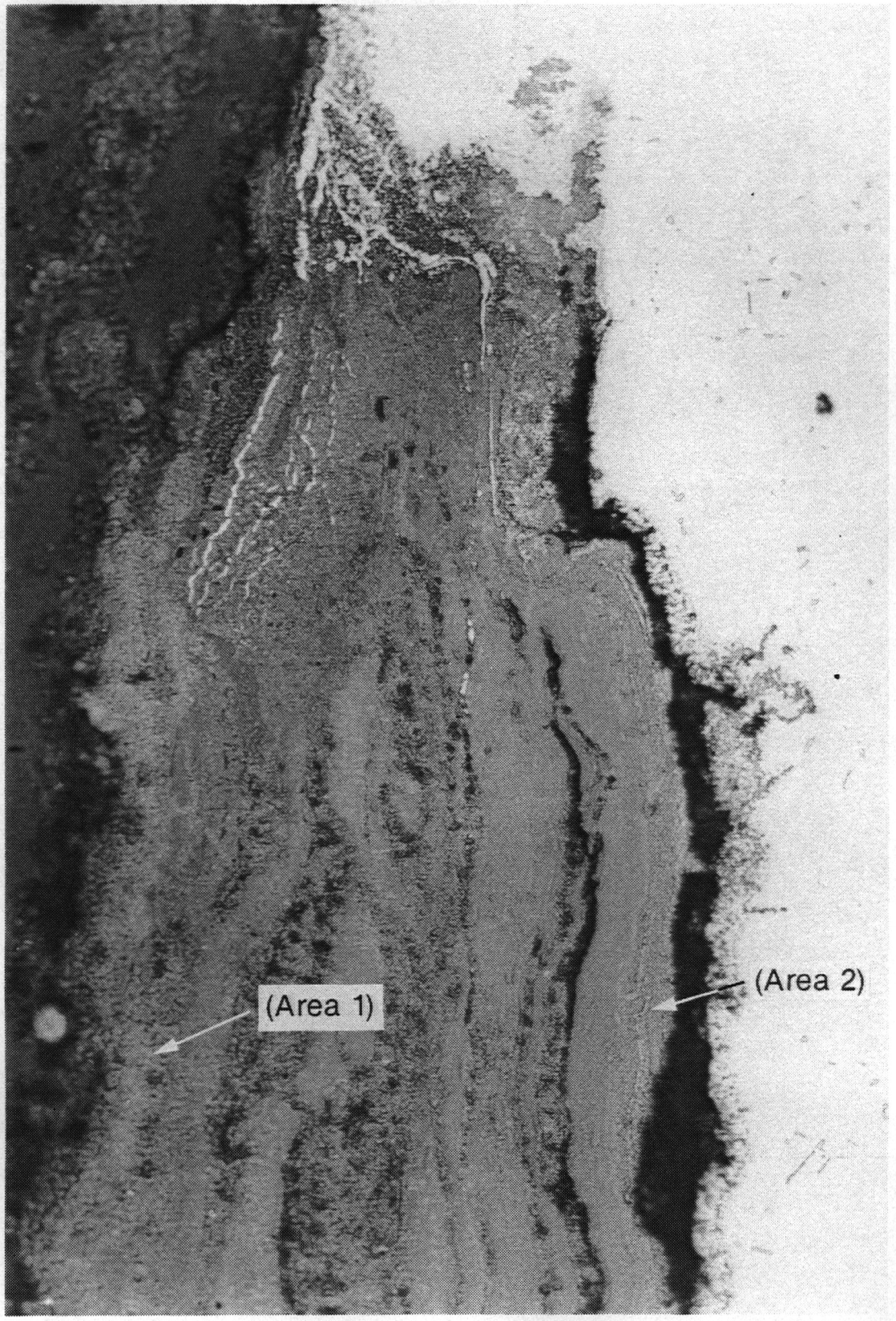

Figure 2-20. LTMT, RT22 over IN-738, 1300 °F, 400X, As Polished.

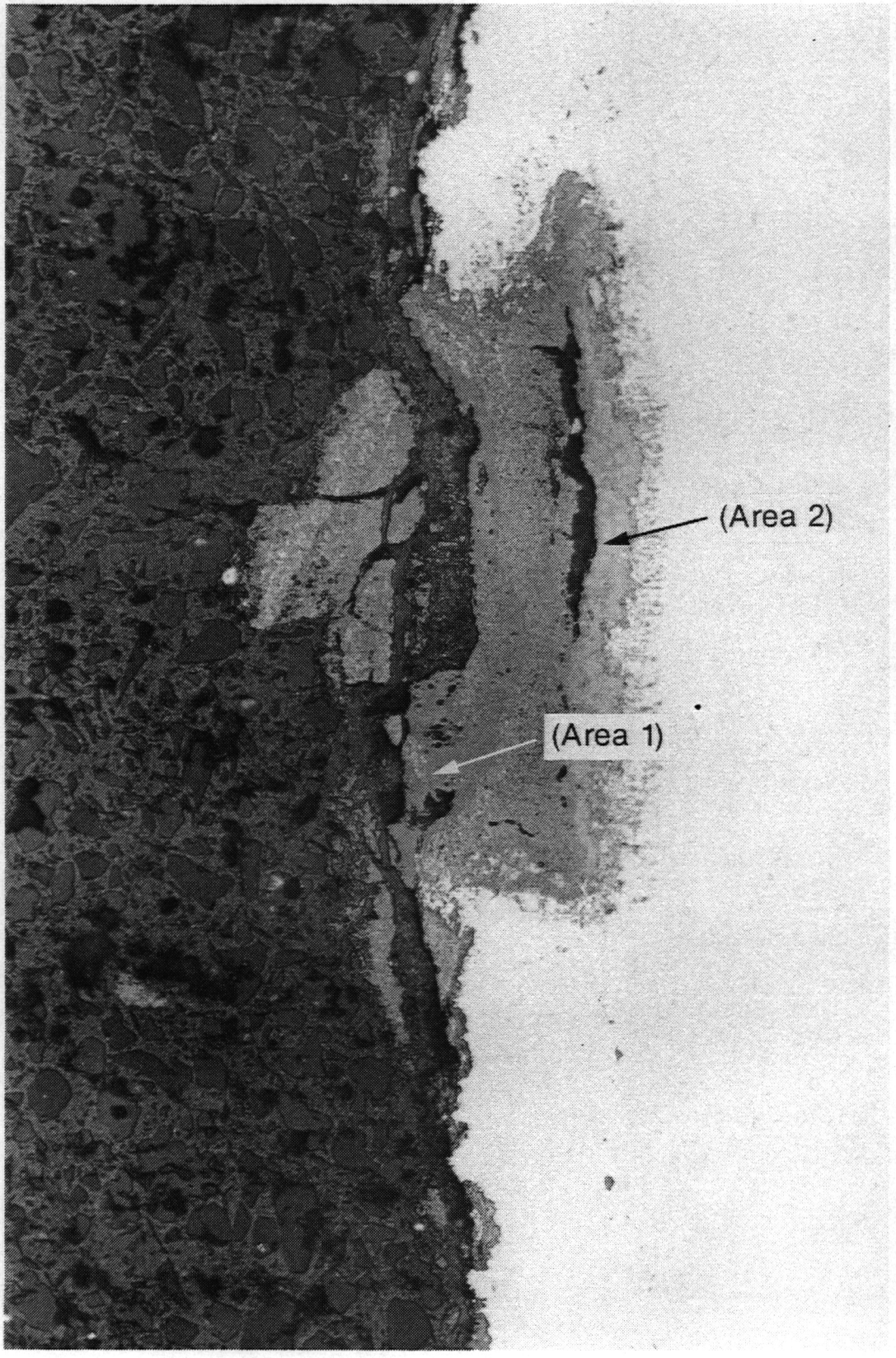

Figure 2-21. LTMT, RT22 over IN-738, 1100 °F, 400X, As Polished.

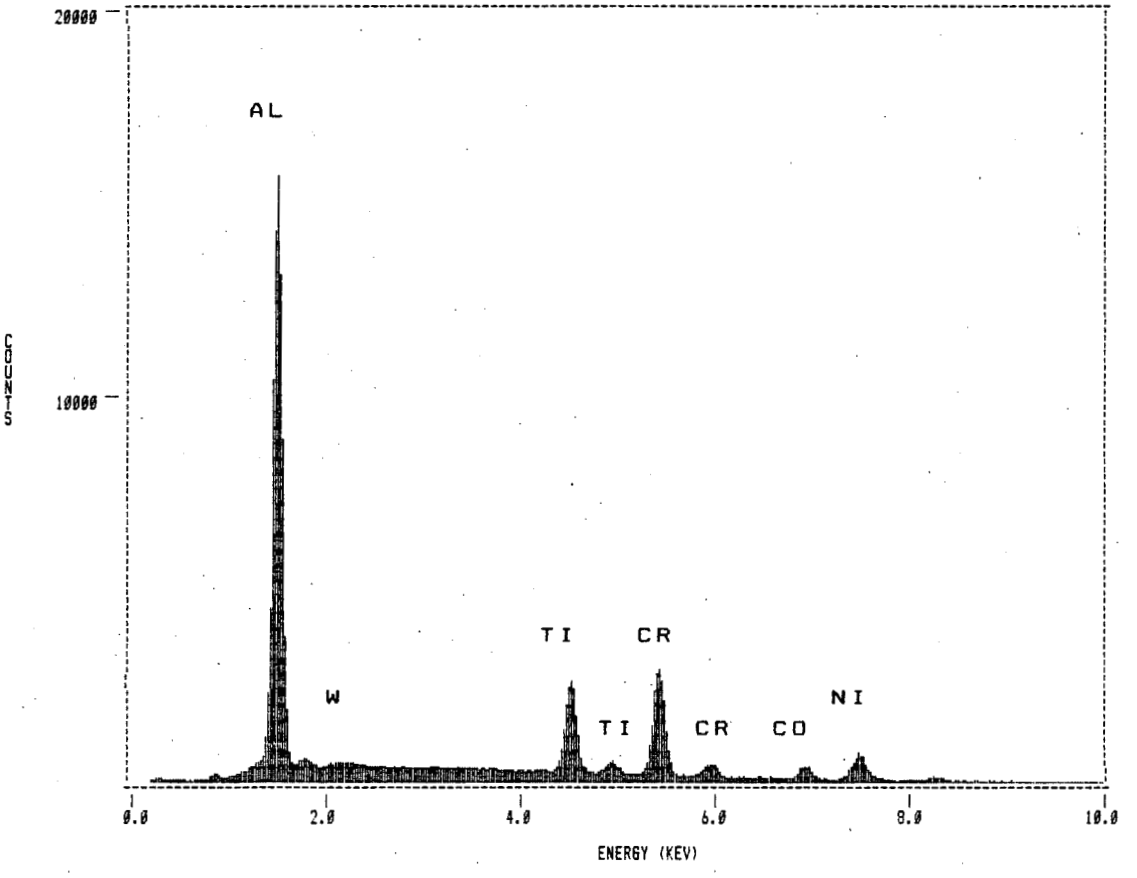

Figure 2-22. **Microprobe Spectra (Area 2) Near Scale - Alloy Interface, 1500 °F Specimen.**

For the 1300 °F specimen, a typical low-temperature, hot-corrosion morphology has developed. Figure 2-20 shows a portion of a large pit. The specimen was in test 5785 hours. The coating has been penetrated and attack into the alloy is occurring. The outer scale was mostly Ni. This outer portion is believed to be mostly precipitated Ni from the Ni which was originally in the molten salt. This precipitation is believed to occur when oxygen reacts with dissolved Ni in the molten salt. The portion of the scale near the bottom of the pit is sulfide rich, which is what is usually seen in this form of attack. Microprobe spectra for the inner and outer portions of the scale are given in Figures 2-23 and 2-24, respectively. A sulfur map for a portion of the pit shown in Figure 2-20 is given in Figure 2-25.

The 1100 °F specimen corrosion morphology is given in Figure 2-21. Again a low-temperature, hot-corrosion morphology has developed. Microprobe spectra are given in Figures 2-26 and 2-27. Again there is mostly Al in the outer scale and Al and Cr towards the bottom of the pit along with other elements from the alloy. Also, some Pt is present. This specimen was in test 5228 hours and corrosion into the alloy was beginning to occur. Figures 2-28 and 2-29 show platinum and S maps, respectively, in the coating near the pit edge. Again the sulfur is confined mainly to the pit bottom and edge. This degree of attack at 1100 °F is unusual compared to what has been seen in the air-cooled small burner rig specimens. However, there is a great deal of difference in the times of exposures. (The burner rig tests have been for 200 hours.) There is some indication in the burner rig tests, where both of the contaminants Na and K (the principal contaminants of coal) are present, the attack is beginning at 1100 °F.

The metallography of the LTMT materials reviewed here show the differences between high (1600-1400 °F) and low-temperature (1400 °F - 1100 °F) structures. The high-temperature structure has internal precipitates and the low-temperature structure does not. The low-temperature structure is mainly scale sitting on matrix metal. EDAX shows that the sulfides reside at the scale-matrix interface, but within the scale. This is in contrast to the high-temperature case where the sulfides appear as precipitates within the matrix.

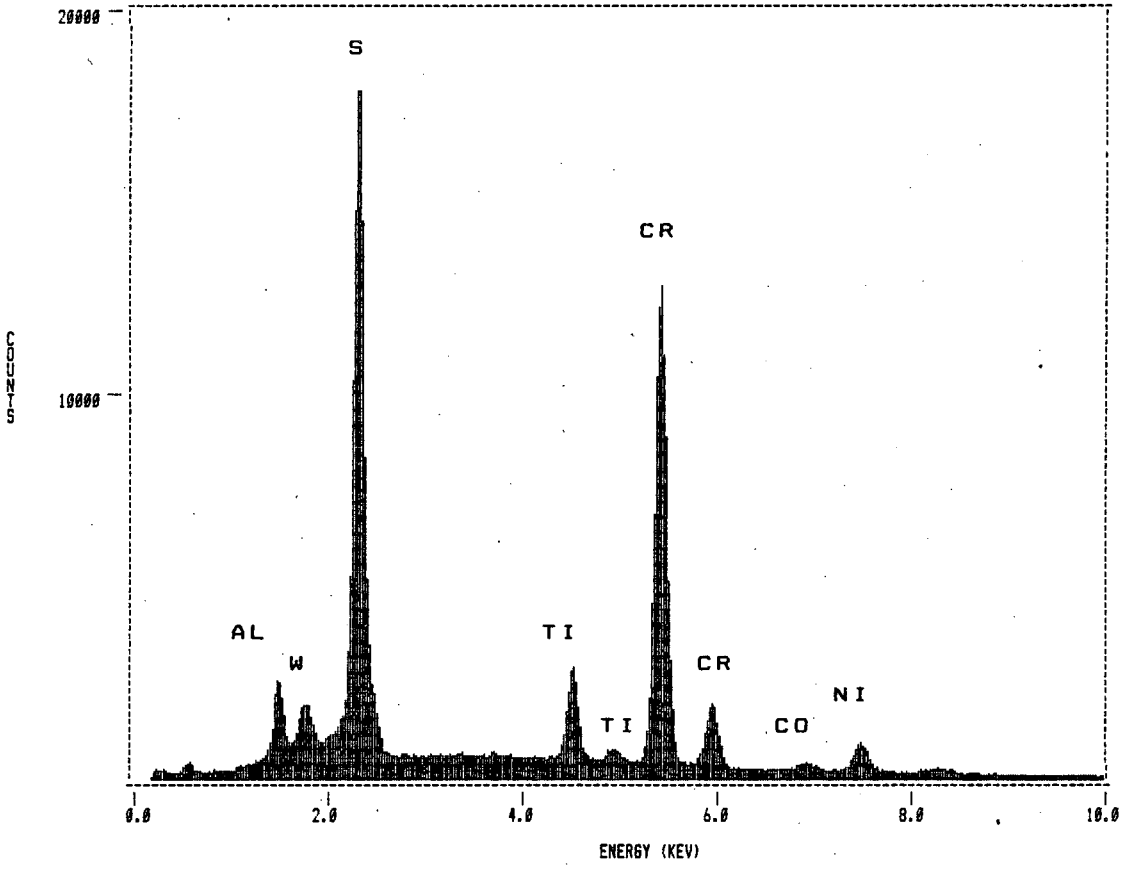

Figure 2-23. Microprobe Spectra (Area 2) Inner Scale, 1300 °F Specimen.

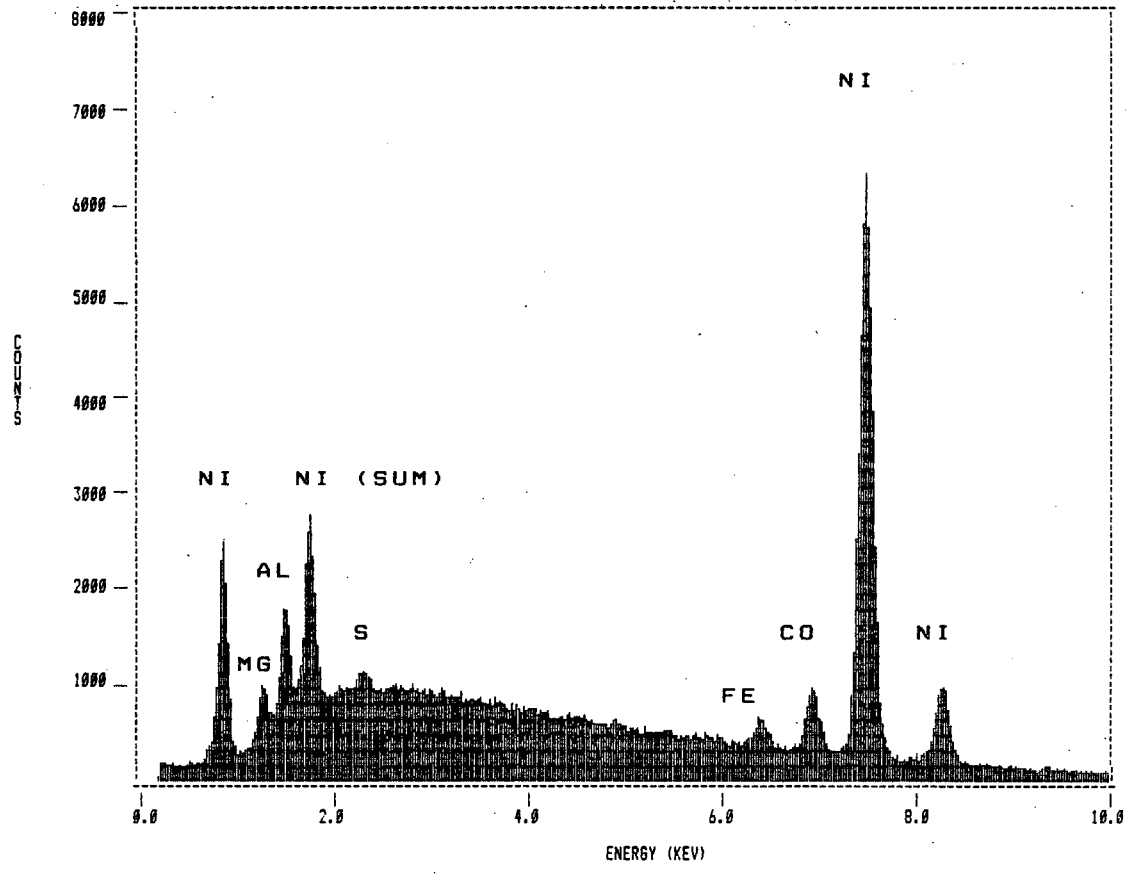

Figure 2-24. Microprobe Spectra (Area 1) Outer Scale, 1300 °F Specimen.

Figure 2-25. **Sulfur Map, 580X, 1300 °F Specimen at Bottom of Pit, Scale-Alloy Interface (image is reversed).**

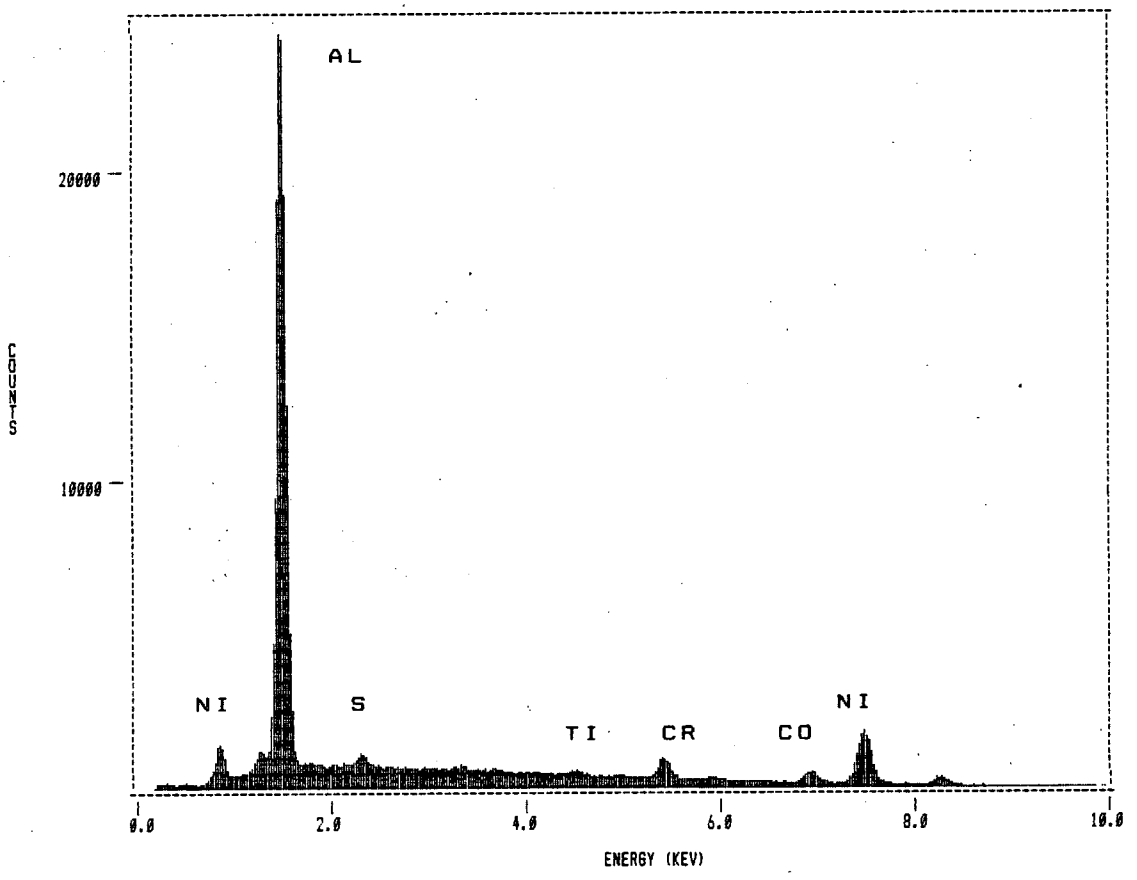

Figure 2-26. Microprobe Spectra (Area 1), Outer Scale, 1100 °F Specimen.

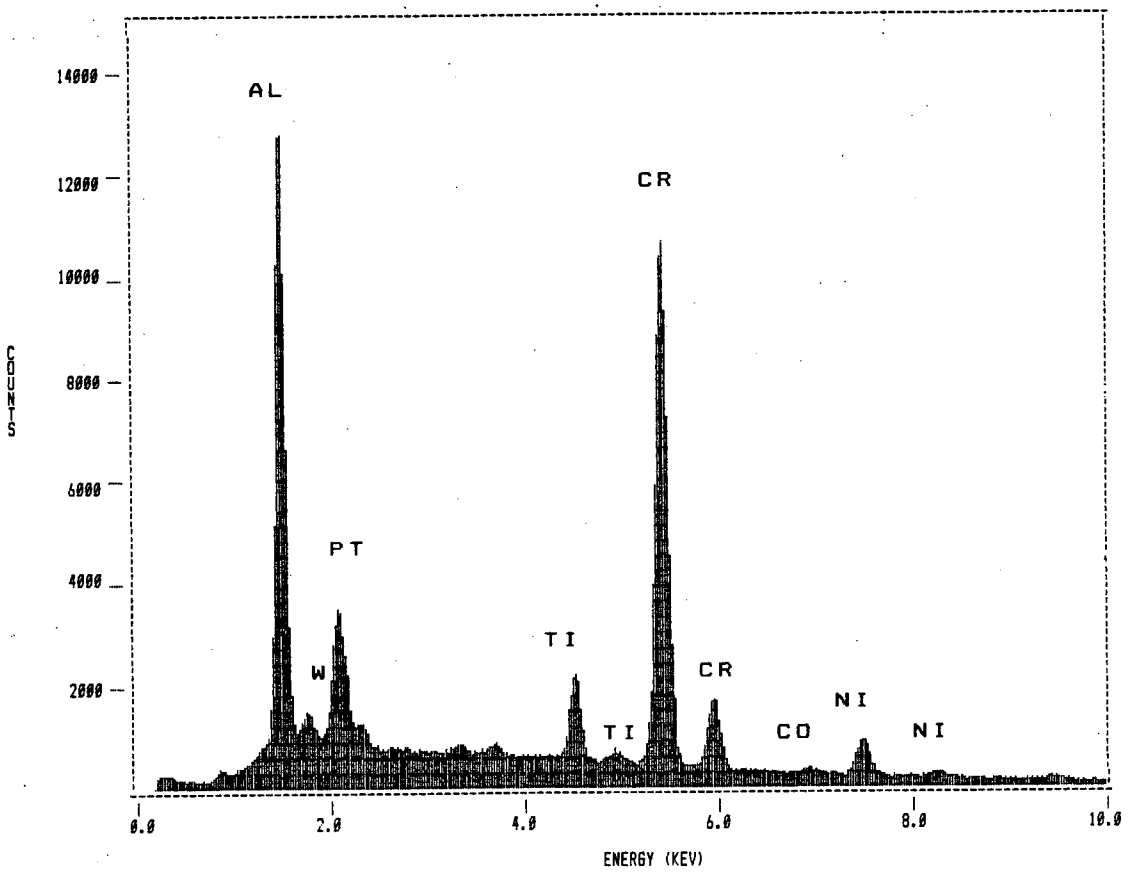

Figure 2-27. Microprobe Spectra (Area 2), Pit Bottom, 1100 °F Specimen.

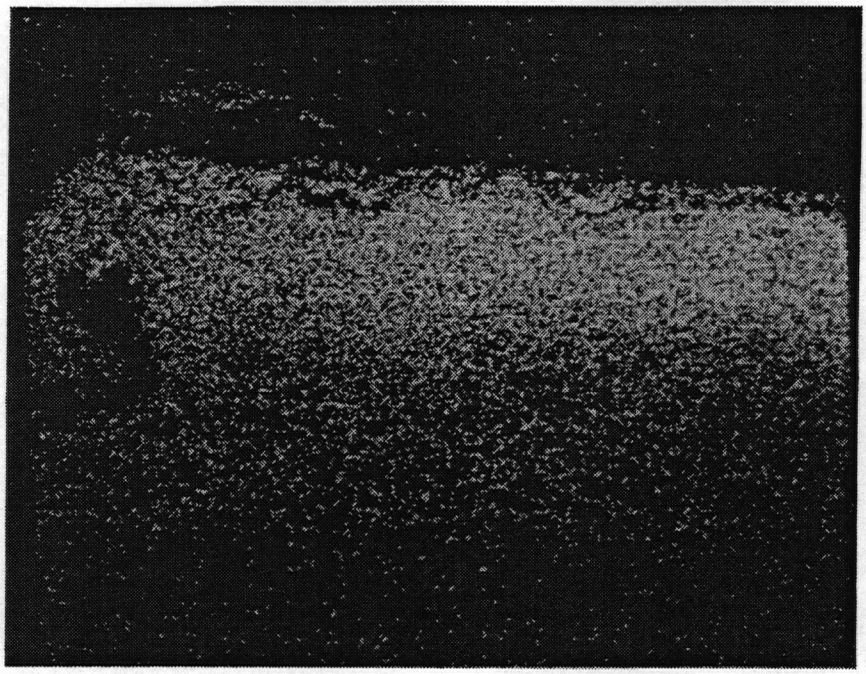

Figure 2-28. **Pt Map (left-hand edge of pit in Figure 2-21, image reversed), Coating and Pit, 1100 °F Specimen, 560X.**

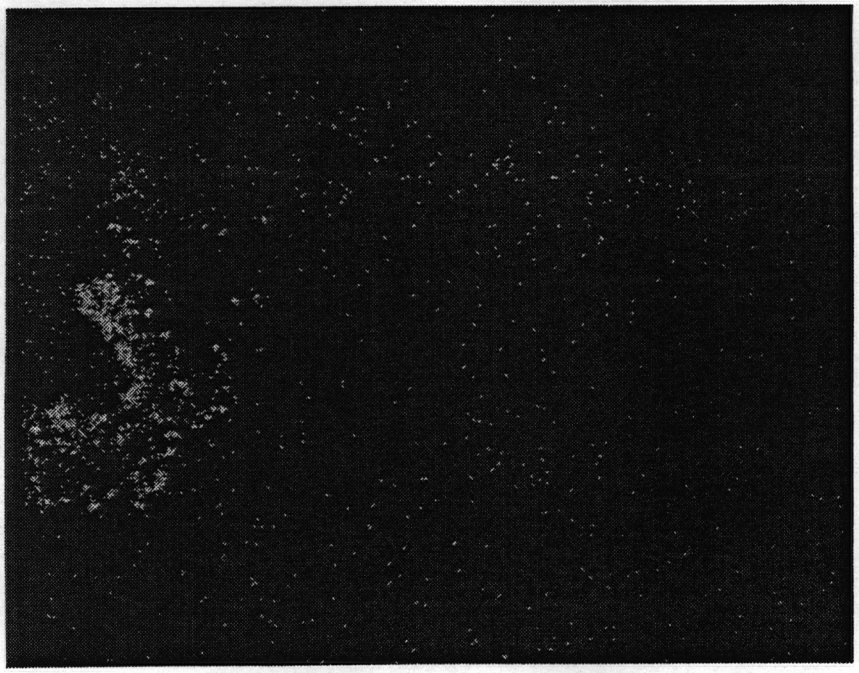

Figure 2-29. **S Map (left-hand edge of pit in Figure 2-21, image reversed), Coating and Pit, 1100 °F Specimen, 560X.**

3. THERMOCHEMICAL CALCULATIONS

3.1 INTRODUCTION

Under gas turbine conditions, the formation of low melting Na_2SO_4- $CoSO_4$ eutectic occurs by interaction of the sodium sulfate salt with the cobalt oxide originating from the alloy component and SO_3 in the gas. The partial pressures of SO_3 required to stabilize this eutectic have been calculated and measured by Luthra and Shores [4]. Similar calculations and measurements have subsequently been performed for this and the Na_2SO_4- $NiSO_4$ system by others [11-13]. The purpose of the present study was to determine the conditions under which binary K_2SO_4-$CoSO_4$ and ternary Na_2SO_4-K_2SO_4-$CoSO_4$ eutectics can form. Whereas the binary Na_2SO_4-$CoSO_4$ and K_2SO_4-$CoSO_4$ phase diagrams are known, the ternary diagram is unknown. Therefore, another purpose of the present study was to estimate the liquidus compositions in the ternary Na_2SO_4-K_2SO_4-$CoSO_4$ system.

3.2 THERMODYNAMIC BASIS

The liquids containing Na_2SO_4, K_2SO_4, and $CoSO_4$ can form on alloys containing cobalt by interaction of cobalt oxides with SO_3 in the gas. The sulfation reactions are

$$1/3\ Co_3O_4(s) + SO_3(g) = \underline{CoSO_4}\ (s,l) + 1/6\ O_2(g) \qquad (1)$$

$$CoO(s) + SO_3(g) = \underline{CoSO_4}\ (s,l) \qquad (2)$$

Here, the underline indicates that $CoSO_4$ is present at an activity of less than unity. At P_{O_2} of 1 atm, Co_3O_4 is more stable than CoO at temperatures below 947 °C. Thus, reaction (1) would fix the minimum SO_3 pressures required to stabilize the liquid at temperatures below 947 °C, while reaction (2) would fix the SO_3 pressures at higher temperatures.

Unless otherwise indicated, the thermodynamic data used in this work were obtained from JANAF Tables and supplements [14]. Unfortunately, there are no reported data for $CoSO_4$ [1]. Free energy values for $CoSO_4$ were estimated from an analysis of the Na_2SO_4-$CoSO_4$ phase diagram, as described later in this report.

The minimum activity of $CoSO_4$ required to stabilize the liquid phase depends on the composition of the liquidus line (in the two-component systems) or of the liquidus surface (in the three-component system). One can calculate these activities from the phase diagram if one assumes a model for how the activities depend upon temperature and composition. Ideal solution models are inappropriate. Inspection of the binary phase diagrams shows that the solutions are far from ideal. In these analyses the next most complicated models were adopted, either a regular solution or a sub-regular solution [15] model. In either model the entropy of mixing is the same as in an ideal solution [16-18]. The enthalpy of mixing is not assumed to be zero, however, as it is in an ideal solution. In the regular solution model the enthalpy of mixing is described by one additional empirical parameter, in the sub-regular model by two. Analyses of the phase diagrams with these models are described in Appendix A. There the binary phase diagrams appear in Figures A-1, A-2, and A-6. From a thermochemical analysis of these the ternary phase diagrams given in Figures A-4 and A-5 were constructed. The significance of these calculations is shown in the stability diagram given in Figure 3-1. This Figure shows the field of stability of a liquid sulfate salt melt, which is the region above any one of the three curves. Considering the curves labelled Na_2SO_4 and Na_2SO_4-K_2SO_4 it is seen that the SO_3 partial pressure necessary to stabilize a liquid in the latter case is about an order of magnitude below that for Na_2SO_4.

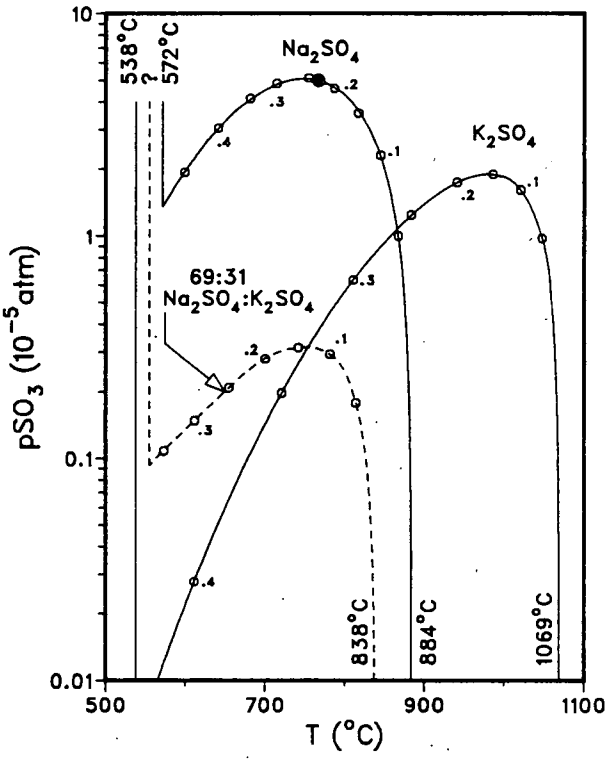

Figure 3-1. **SO_3 partial pressures at the freezing point calculated as described in Appendix A for K_2SO_4-$CoSO_4$-Na_2SO_4 mixtures containing Na_2SO_4:K_2SO_4 mole ratios of 100:0, 0:100, and 69:31. The point marked with the solid circle on the upper curve is at $5x10^{-5}$ atm and 767 °C and was fitted exactly in the analysis of the Na_2SO_4-$CoSO_4$ binary. Choosing a higher or lower P_{SO_3} at this point scales all these curves up or down together. Points at a 69:31 mole ratio along the dashed curve were taken from the dashed lines in Figures 3-4 and 3-5. The partial pressure maximum in this curve is the lowest maximum in the ternary system, but the maxima are not much higher for all Na_2SO_4:K_2SO_4 mole ratios between about 1:9 and 9:1, as will be evident from examination of Figure 3-5. Between 700 and 884 °C the SO_3 partial pressure required to form a liquid is substantially lower for K_2SO_4 alone or for K_2SO_4-Na_2SO_4 mixtures than it is for Na_2SO_4 alone. Circles on curves are mole fractions of cobalt sulfate in the sulfate melt.**

In particular considering the case of a metal temperature of 700 °C (1292 °F) it is seen that a SO_3 partial pressure of about 4 x 10^{-5} atm is required for the Na_2SO_4 case and the melt will be about 35 mole percent cobalt sulfate. For a 69:31 (molar ratio) Na_2SO_4-K_2SO_4 melt the minimum SO_3 partial pressure required for liquid formation is 3 x 10^{-6} atm and the melt would contain about 20 mole percent cobalt sulfate.

Figure 3-1 clearly shows the stabilizing effect of potassium and thus its enhancement of hot corrosion. Its presence allows liquid formation at lower temperatures and lower SO_3 pressures, and it is clear the presence of a liquid is necessary for hot corrosion.

3.3 MELTING EXPERIMENTS IN K_2SO_4-$CoSO_4$

Experiments were conducted to verify the predictions of the calculations given in Appendix A and shown in Figure 3-1 by investigating the onset of melting in the K_2SO_4-$CoSO_4$ system as a function of SO_3 partial pressure. The SO_3 levels required to stabilize a K_2SO_4-$CoSO_4$ liquid depend on the partial pressure of oxygen. At high oxygen partial pressures, Co_3O_4 is more stable than CoO. Consequently, the SO_3 pressures required to stabilize the liquid phase would be fixed by reaction 1. The SO_3 partial pressure varies directly with P_{O_2}. At lower partial pressures of oxygen (depending on temperature), CoO is more stable than Co_3O_4. Consequently, reaction 2 would fix the SO_3 partial pressures. The SO_3 partial would be independent of oxygen partial pressure and is shown in Figure 3-2 along with that for Co_3O_4. At an oxygen partial pressure of 1 atm, Co_3O_4 is more stable than CoO at temperatures below 947 °C. Consequently, the two curves intersect at 947 °C.

The experiments were conducted on thin foils of pure cobalt. Samples of pure cobalt 13 x 13 x 0.2 mm in dimensions were oxidized for 96 hours at 800 °C in air. This should result in a thick oxide film primarily containing CoO but also containing a thin layer of Co_3O_4 on the surface. No attempt was made to determine the thickness of these films, but the weight gains suggested that about 50% of the cobalt sample had oxidized. The oxidized samples were then coated with either 2.5 mg/cm^2 of K_2SO_4 or 5.0 mg/cm^2 of K_2SO_4-50 mole % $CoSO_4$. The samples were then exposed in oxygen containing 23 ppm (SO_2 + SO_3) at 700 to 900 °C. A platinum catalyst was used near the sample to ensure equilibrium between O_2, SO_2, and SO_3. Whether a liquid formed on the surface was then determined by the techniques discussed below.

The first technique was similar to that described in Reference 4. It consisted of exposing the cobalt sample coated with K_2SO_4 at the desired temperature for times of the order of 2 hours. The exposed sample was then observed under a low magnitude viewer to look for signs of melting. Although success was had in using this approach with sodium sulfate, the experiments with K_2SO_4 were ambiguous. It was not possible to say conclusively whether the salt on the surface had melted. Therefore, this approach was abandoned.

The second approach consisted of exposing salt-coated samples at 700 to 900 °C for periods up to 24 hours in the above gas mixture. The exposed samples were then rapidly cooled to room temperature. The salt on the surface was then dissolved in hot water and its composition analyzed chemically. Table 3-1 gives a summary of the results of different experiments. The K_2SO_4-$CoSO_4$ phase diagram suggests that there is little or no solid solubility of $CoSO_4$ in K_2SO_4. Therefore, the presence of a significant amount of $CoSO_4$ in the salt indicates that the salt had melted. If salts had completely equilibrated with the samples, then the compositions of the final salts at any temperature would be the same, irrespective

Table 3-1

RESULTS OF SULFATION EXPERIMENTS IN O_2 - 0.0023% (SO_2 + SO_3)

Starting Salt*	Temp °C	Time, hours	Mole % $CoSo_4$ in Salt	Conclusion - Molten Salt?"
KS	900	6.16	1.7	No
KS	800	6.33	0.1	No
KS	750	22.5	2.6	No
KS	725	22.5	11.0	Yes
KS	700	6.25	15.4	Yes
KS-CS	900	17.25	0.2	No
KS-CS	800	6.25	0.7	No
KS-CS	775	6.25	2.7	No
KS-CS	750	6.25	26.9	Yes
KS-CS	700	6.25	49.6	Yes

* KS: K_2SO_4;
KS-CS: K_2SO_4 - 50 m/o $CoSO_4$

of whether the starting salt was K_2SO_4 or K_2SO_4-50% $CoSO_4$. The results suggest that complete equilibrium has not been achieved. There was, however, a good agreement between the conclusions regarding the melting for both of these salts. The experimental results are compared to the predicted curves in Figure 3-2. Since the experiments were conducted at PO_2 = 1 atm, where Co_3O_4 is stable, the experimental results should be compared with the results of calculations for Co_3O_4. The agreement between the theoretical calculations and the experimental results is remarkable.

It would have been helpful to conduct experiments to check the SO_3 pressures required to form liquids on 69:31 mixtures of Na_2SO_4 and K_2SO_4. However, Figure 3-1 shows that at temperatures significantly away from the melting point of this salt (i.e., below about 800 °C), the SO_3 pressures required to stabilize liquids for this salt are similar to those for K_2SO_4. It is felt that the experimental technique is not sensitive enough to determine the difference between the two.

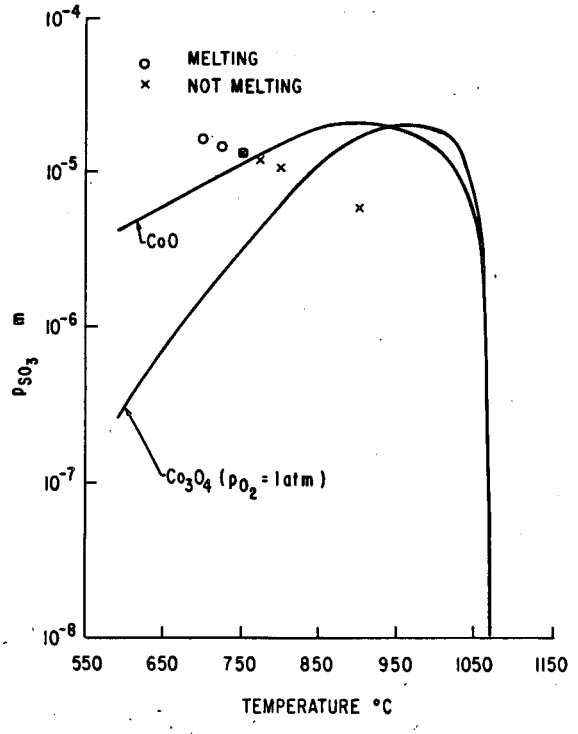

Figure 3-2. **Calculated values of the minimum P_{SO_3} required to form a K_2SO_4-$CoSO_4$ liquid from Co_3O_4 at P_{O_2} = 1 atm and from CoO. The P_{SO_3} levels for CoO are independent of P_{O_2}, whereas those for Co_3O_4 decrease with P_{O_2}. Also shown are the results of experiments conducted on oxidized cobalt samples. "O" points indicate the conditions where the salt had melted while "X" points indicate those where the salt had not melted.**

3.4 DISCUSSION

The SO_3 levels required to stabilize the liquids are lower in the presence of K_2SO_4 because the activities of $CoSO_4$ are lower. The lower $CoSO_4$ activities along the liquidus lines (surfaces) arise due to considerably more negative heats of mixing in K_2SO_4-$CoSO_4$ mixtures than in Na_2SO_4-$CoSO_4$ mixtures. This can be seen readily from the empirical parameters listed in lines 2 and 4 of Table A-2. For example, for 50:50 mixtures, where all mole fractions are equal to 0.5, the excess free energy of mixing in the K_2SO_4-$CoSO_4$ liquid is about -5900 cal/mol while that in the Na_2SO_4-$CoSO_4$ liquid is about -2800 cal/mol. The difference is not small in comparison to RT, which, for example, at 700 °C is 1900 cal/mole.

That the excess free energy values are more negative in the K_2SO_4-$CoSO_4$ system than in the Na_2SO_4-$CoSO_4$ system suggests that the net attractive interaction between K^+ and Co^{++} ions is stronger than that between Na^+ and Co^{++} ions in these sulfate melts. Similar results have been noted in other binary salt mixtures by Blander [18]. He observes that in liquid salts with one monovalent cation, one divalent cation, and common anion, the heat of mixing is more negative (the energy of interaction is more attractive) the larger the disparity between the monovalent ion radius and the divalent ion radius. That is the situation in the present case, where the ionic radii of K^+, Na^+, and Co^{++}* are 1.33, 0.95, and 0.74 angstroms, respectively.

The results in Figures A-5, 3-1, and 3-2 have important implications with reference to low-temperature hot corrosion in gas turbines. Low-temperature hot corrosion is observed in the temperature range of 600 to 800 °C. It is normally believed that a liquid film is necessary for hot corrosion to occur. The SO_3 levels required to stabilize a liquid film on cobalt based alloys are much lower in the presence of K_2SO_4 in comparison to salts containing only Na_2SO_4. Therefore, low-temperature hot corrosion would occur much more readily in the presence of K_2SO_4 in the salt. Once a liquid film is obtained, the rate of further corrosion may be related to the driving force for sulfation, which in turn is related to the difference in partial pressure of SO_3 in the gas and that required to stabilize the liquid phase. Therefore, under the conditions where both the Na_2SO_4-$CoSO_4$ and the K_2SO_4-$CoSO_4$ eutectics are stable, the corrosion is expected to be more severe in the presence of K_2SO_4. In systems with coal combustion gases, salts containing both the Na_2SO_4 and K_2SO_4 are expected to condense. Therefore, low-temperature hot corrosion is expected to be worse in systems with coal combustion gases in comparison to systems using petroleum-derived fuels, which normally contain only the sodium impurities.

* Pauling, P. The Nature of the Chemical Bond, 3rd Ed., Cornell University Press, 1960

4. AIR-COOLED SMALL BURNER RIG (ACSBR) CONFIRMATORY TESTS

4.1 INTRODUCTION

Burner rig tests were run with the aim of trying to simulate the PFB low-velocity test section conditions and to verify the results of the theoretical calculations, given in Task 2.

To this end a small burner rig was modified to accept air-cooled specimens (see Figure 4-1). The test specimens were the same as used in the low-velocity test section of the PFB and consisted of tubes 0.25 inches in diameter with a 0.125-inch axial cooling hole through which air passed to achieve a desired metal temperature. The required cooling air was 0 to 0.4 cfm per tube to achieve cooling of 0 to 500 °F below the combustion gas temperature. The combustion gas temperature was held at 1600 °F for all tests. The burner rig air and fuel flows were 35.5 lb/h and 5.5 cc/min, respectively. The combustion gas velocity was calculated to be about 90 ft/s compared to 23 ft/s in the LVTS in the LTMT. (See Table 2-1.) The specimen heat transfer coefficient has been determined to be about 20 Btu/ft^{2}h F. In terms of geometry and gas flows the air-cooled small burner rig (ACSBR) was quite similar to the low-velocity test section of the PFB. The PFB-LVTS data are given in Table 2-1.

The primary consideration, according to Figures A-5 and 3-1, in determining the temperature regime over which low-temperature corrosion will occur is the SO_3 partial pressure. For the PFB-LVTS the SO_2 partial pressure (all sulfur counted as SO_2) is estimated to be about 10^{-3} atm. This is assuming 95% capture of the sulfur in the 5% sulfur coal. Of course it is the SO_3 partial pressure that determines the stability of the alloy sulfates. It is known from boiler and gas turbine experience that about 5 to 10% of the sulfur in the combustion gases is converted to SO_3, the remainder being SO_2.* However, it is probably considerably higher over a metal surface, which may act as a catalyst and cause the SO_3 to approach equilibrium levels, about 60% of the sulfur in the combustion gases (at 1350 °F and 10 atm). Appendix B gives the fraction of sulfur converted to SO_3 under equilibrium conditions. Based on Figures A-5 and 3-1, SO_3 levels in the PFB-LVTS are probably well above what is necessary to stabilize the alloys sulfates, even in the absence of K_2SO_4.

In the ACSBR tests the sulfur levels were varied from test to test by adding SO_2 to the primary air and by varying the sulfur in the fuel. In this way sulfur levels counted as SO_2 were varied between 3.8×10^{-3} and 4.1×10^{-8} atm and the results compared with Figures A-5 and 3-1.

After construction of the ACSBR, a preliminary run over a period of 48 hours was made. Thermocouples welded to the trailing edge of each tube survived this test and demonstrated good control, and stability was possible with an air control valve on each pin, as shown in Figure 4-1. Subsequent testing over longer times showed that sometimes thermocouples became inoperable or erratic because of corrosion. However, because the ACSBR combustion gas flow temperature as well as pin cooling air flow were held fixed throughout the run, outer metal temperatures are assumed to stay close to their new and

*It is believed that the SO_3 levels in the combustion gases are somewhat frozen at the values attained during combustion, where they are determined by the temperature, the sulfur level, and concentrations of atomic oxygen. The SO_3 content of the combustion gases only increases downstream of the combustion zone where it passes over surfaces which may act as catalysts.

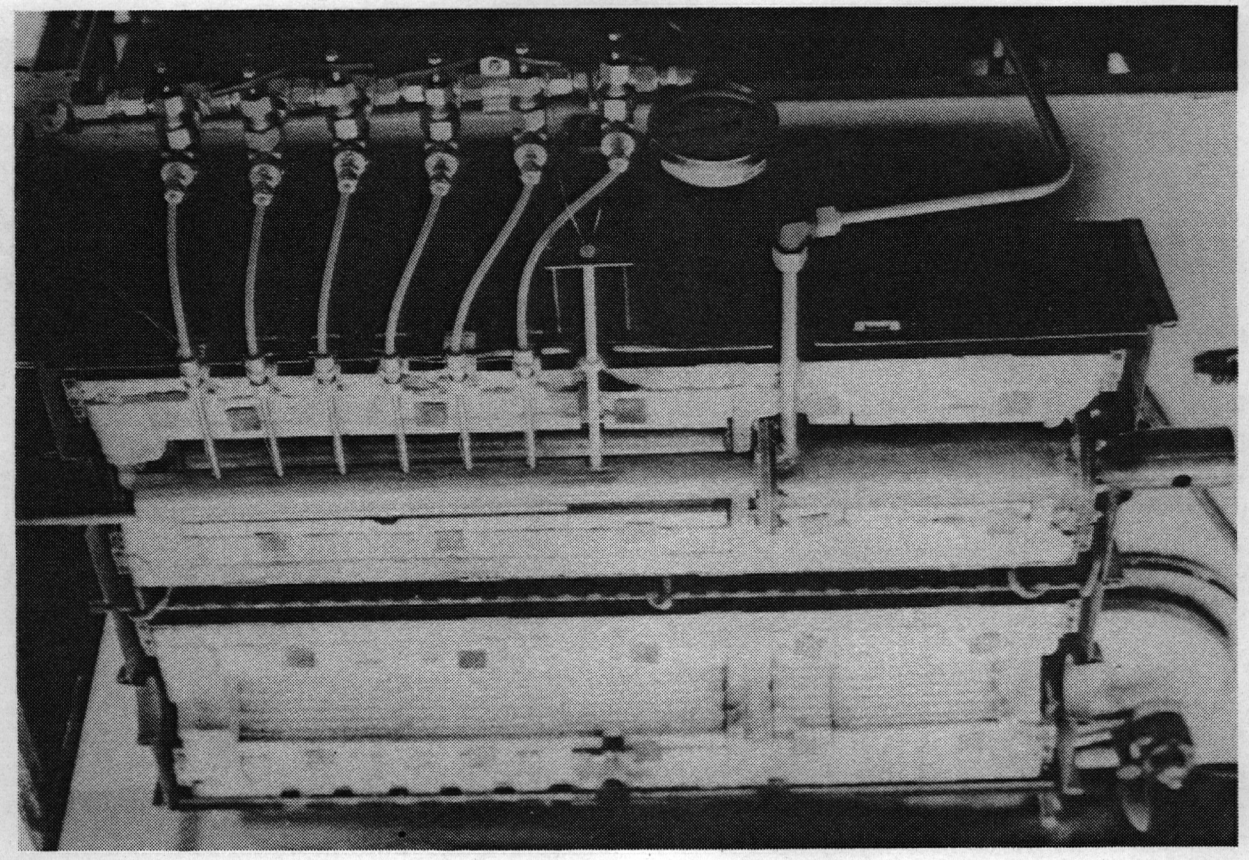

Figure 4-1. Air-Cooled Small Burner.

clean values in spite of the effects of corrosion.** But it should be noted that the combined effects of variations of combustion gas temperature, cooling air flow, and corrosion scale probably meant that specimen temperatures could not have been maintained better than +25 °F during the course of a test.

The corrosion testing performed is given in Table 4-1. One alloy was used in all the tests, IN-738 (Ni(bal), Co(8.5), Cr(16), Al(3.4), Ti(3.4), Mo(1.75), W(2.6), Cb(0.9), Ta(1.75)). Nine tests were run. They consisted of three groups of three: the Na contaminant tests, the Na+K contaminant tests, and the additive tests. In the first two groups of tests the sulfur levels were varied to determine the effect of this variable and check on the thermochemical predictions. In the last group of tests the most corrosive conditions of the first two groups of tests were duplicated, but an additive was put in the fuel.

The alkali levels used in the tests were based on levels normally used in small burner rig accelerated testing in the GE Gas Turbine Development Laboratory. The levels are equivalent to about 5 ppm alkali in a gas turbine fuel or about 5 times the amount allowed in the gas turbine fuel specification. The sulfur levels chosen as air-side additions of SO_2 to the small burner rig are an attempt to achieve P_{SO_3} levels in a one atm rig equivalent to those found in gas turbines where the total pressures may be 10 atm.

The results of these tests in terms of corrosion are given in Table 4-2. It is observed that low enough sulfur levels were attained in the first two groups of tests to nearly eliminate low-temperature corrosion (1400 °F-1100 °F). This occurred in Tests 2 and 6. For Tables 4-1 and 4-2 all the sulfur present is considered as SO_2. As has been discussed the SO_3 level determines the sulfate stability and is probably somewhere between 0.1 and 0.4 of the tabulated values, the 0.4 value being about equilibrium in the ACSBR (1 atm) at 1350 °F. It is also observed that the additive tests were quite effective in substantially reducing corrosion at the highest sulfur levels. This even occurred at 1600 °F where reductions in sulfur level had little effect and did not reduce corrosion rates.

4.2 SODIUM TEST RESULTS

Corrosion data given in Table 4-2 give the maximum penetration (the depth of internal oxides and/or sulfides from the original interface) of corrosion for each pin. Corrosion penetrations generally were based on the difference in pretest and post-test diameters, the post-test diameter being the minimum diameter of metal not affected by corrosion attack. Sometimes in the case of pitting attack the penetration was taken as the value for the deepest pit.

Test 1 was the most severe of the Na contaminant tests. The corrosion structures given in Figures 4-2 through 4-7 give the corrosion microstructures for this test.

The specimens shown were etched with the standard 2:2:1 etch: 2 parts HCL, 2 parts Gycerol, and 2 parts HNO_3. The pins were designated according to their pretest temperatures, determined by a trailing edge thermocouple, and set by adjusting the cooling air flow. During the course of the test, the thermocouples became unreliable because of environmental attack. It is believed, however, that the pretest temperatures remained fairly

**This is because the large temperature drops between the combustion gas and cooling air occur primarily across the boundary layers and not across the walls of the specimen.

Table 4-1

ACSBR TEST CONDITIONS

Test Type	Test No.	Fuel	Fuel Contaminant					SO_2 Air Add. (cc/min)	pSO_2 (atm)
			S(%)	Na(ppm)	K(ppm)	Mg(ppm)	V(ppm)		
Na	1	No.2	0.17	125	4	13	0	784	3.8×10^{-3}
	2	No. 2	0.17	125	4	13	0	0	2.7×10^{-5}
	3	No. 2	0.16	125	4	13	0	784	3.8×10^{-3}
Na + K	4	No. 2	0.87	85	100	16	0	0	1.4×10^{-4}
	5	No. 2	0.14	85	100	16	0	0	2.2×10^{-5}
	6	K-1	0.026	100	110	16	0	0	4.1×10^{-6}
Additive Tests	7	No. 2	0.16	130	4	440	0	784	3.8×10^{-3}
	8	No. 2	0.16	130	4	465	69	784	3.8×10^{-3}
	9	No. 2	0.16	85	100	465	0	784	3.8×10^{-3}

Notes: Test 1,2, and 3 used ASTM sea salt additive.
Air flow rate is 268 gm/min.
Fuel flow rate is 4.7 gm/min.
Nominal test time is 200 h.
Vanadium napthenate was the V additive.
Mg additives were oil soluble (KI-16, Tretolite Corp.; GTT-124, Buckley Assn.).
Test 4, 5, 6, and 9 used NaCl and KCl for the alkali additives.

Table 4-2

ACSBR TEST CORROSION

Temperature		Corrosion (mils)							
Test	1	2	3	4	5	6	7	8	9
Principal Fuel Contaminants	Na	Na	Na	Na + K	Na + K	Na + K	Na + Mg	Na + V + Mg	Na + K + Mg
pSO_2 (atm) $\times 10^4$	38.0	0.27	38.0	1.4	0.22	0.041	38.0	38.0	38.0
1600° F	13.1	3.3	7.3	9.3	15.2	17.2	2.0	0.8 (3.0)	1.4
1550° F			11.2						
1500° F	1.4	0.3	17.1	13.2	7.3	5.3	1.4	0.2	0.1
1450° F			15.1						
1400° F	15.0	0.3	10.0	13.2	3.4	0.3	3.3	0.8 (2.0)	3.8 (6.0)
1350° F			8.5						
1300° F	7.2	0.1		7.4	1.4	0.9	2.0	0.4	0.2
1250° F									
1200° F	3.3	0.1		3.9	0.6	0.4	0.0	1.0	0.0
1150° F									
1100° F	1.3	0.1		2.3	1.4	0.4	1.0	0.6	0.0

Notes: Test 1, 1400° F, lost cooling air. Should be about 1600° F.
Test 1, 1500° F point is suspicious.
Nominal test time was 200 h.
Parenthesis, Tests 8 and 9 indicate one spot where corrosion was severe.

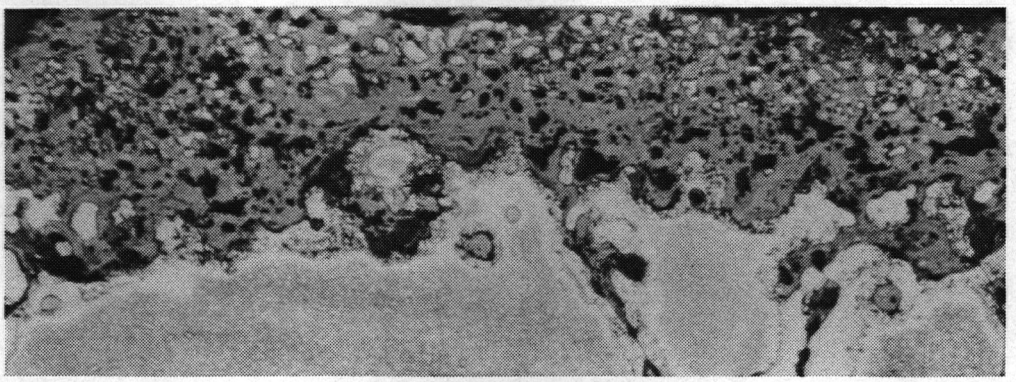

Figure 4-2. **Air-Cooled Small Burner Rig, IN-738, Test No. 1, 1600 °F specimen, 200X, 2-2-1 Etch.**

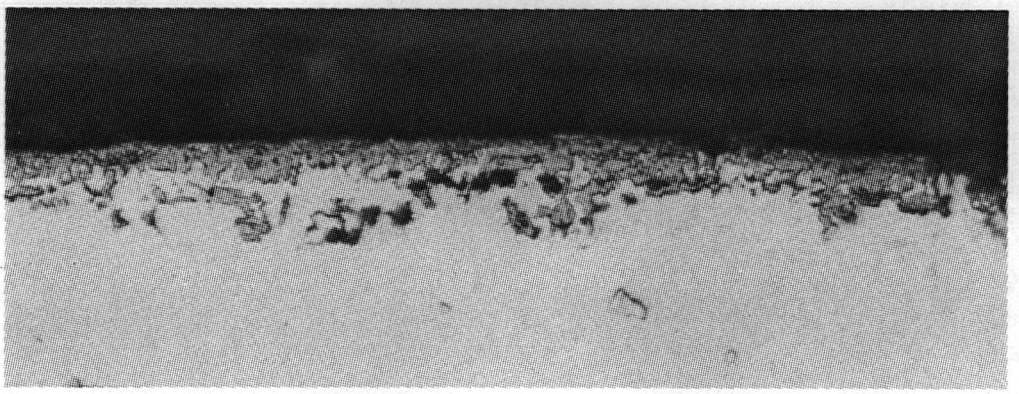

Figure 4-3. **Air-Cooled Small Burner Rig, IN-738, Test No. 1, 1500 °F specimen, 200X, 2-2-1 Etch.**

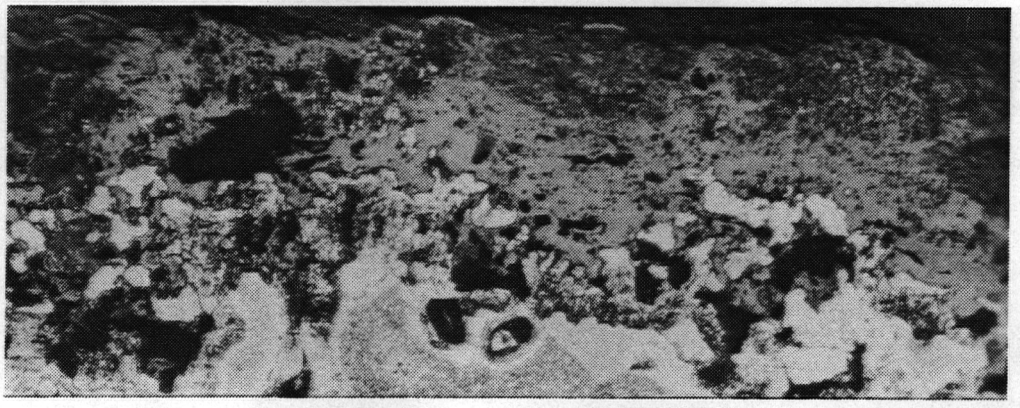

Figure 4-4. **Air-Cooled Small Burner Rig, IN-738, Test No. 1, 1400 °F specimen, 200X, 2-2-1 Etch.**

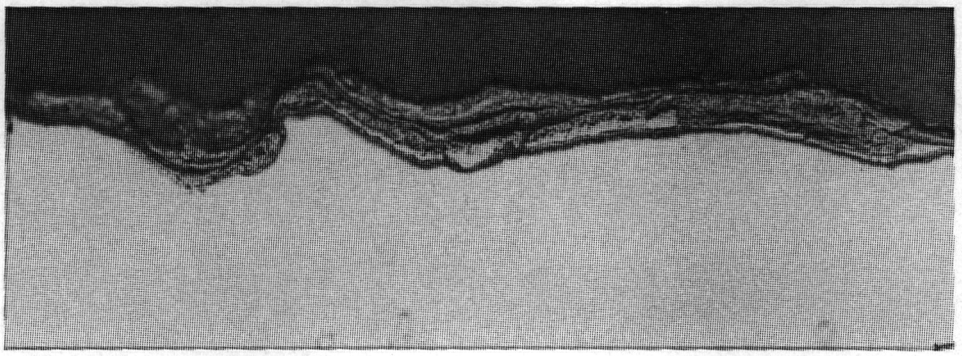

Figure 4-5. **Air-Cooled Small Burner Rig, IN-738, Test No. 1, 1300 °F specimen, 200X, 2-2-1 Etch.**

Figure 4-6. **Air-Cooled Small Burner Rig, IN-738, Test No. 1, 1200 °F specimen, 200X, 2-2-1 Etch.**

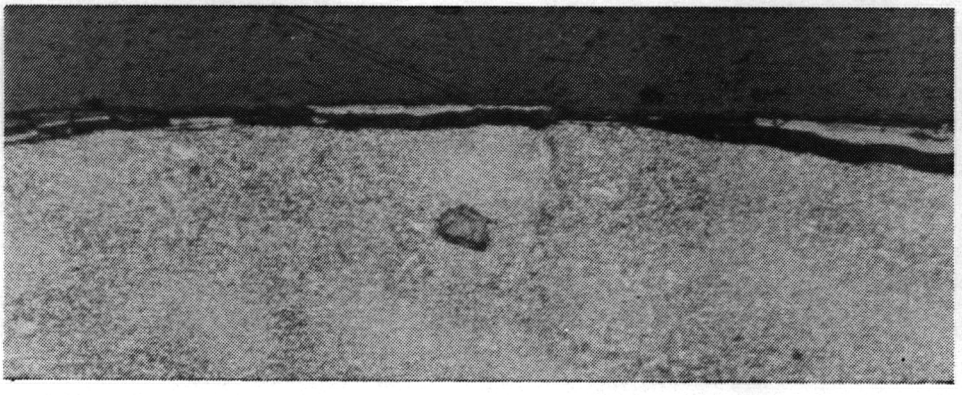

Figure 4-7. **Air-Cooled Small Burner Rig, IN-738, Test No. 1, 1100 °F specimen, 200X, 2-2-1 Etch.**

constant provided air flows remained constant to each pin. This was the case except for the 1400 °F pin which lost cooling air and probably ran at the combustion gas temperature, 1600 °F, for a significant portion of the test.

Figure 4-2 shows the 1600 °F pin with a typical high-temperature hot corrosion structure consisting of a porous oxide depleted metal outer scale over metal with internal attack along grain boundaries. The extent of attack from top of oxide to maximum internal attack is about 15 mils. Figure 4-3 shows the 1500 °F pin with little attack, consisting of a thin oxide scale over depleted metal. The extent of attack is about 1 mil. (In view of Test 3 data, this data point is suspicious.)

The 1400 °F pin shown in Figure 4-4 probably ran at 1600 °F and shows the same morphology of attack as shown in Figure 4-2 and about the same extent of attack, 15 mils.

Figures 4-5, 4-6, and 4-7 are corrosion structures for the pin metal temperatures of 1300, 1200, and 1100 °F, respectively. Much of the corrosion scale was spalled off. At these temperatures the corrosion product is a dense scale with no internal attack. Some pitting can occur, leading to the scalloped-looking structures seen at 1300 and 1200 °F. These are typical low temperature, hot corrosion structures (see Figure 1-3 for the PFB-LVTS).

In Test 2, the sulfur level was considerably reduced by stopping the SO_2 addition to the ACSBR air. Figures 4-8, 4-9, and 4-10 show the microstructures for 1600 °F, 1500 °F, and 1400 °F, respectively. Below 1600 °F, the corrosion attack was very low. The sulfur level in this test, considering all the sulfur as SO_2, was 0.27×10^{-4} atm. This would correspond to a maximum SO_3 partial pressure of about 1×10^{-5} atm at 1350 °F according to Figure B-1. According to Figure 3-1, this is just below the $NaSO_4$ curve at all temperatures. Therefore, there should be no $CoSO_4$ formation and no low-temperature hot corrosion. Indeed, according to Figure 3-1 if P_{SO_3} is 1×10^{-5} then there should be no liquid possible below about 1600 °F, and no corrosion, which is practically what was observed. This is remarkable agreement and perhaps partially fortuitous as the SO_3 pressures are only approximately known and the calculations are approximate themselves. Furthermore, it should be noted that the calculations are for pure cobalt and the test specimens are IN-738.

In Test 3, the Test 1 conditions were repeated to check on the 1500 °F and 1400 °F test points, which as noted above were not considered valid. This was done by spacing the pins in 50 °F-degree intervals instead of the customary 100 °F intervals, and would show if there were any small temperature intervals over which the corrosion rate might be very low as was observed at 1500 °F in Test 1. The results showed considerable attack at all temperatures from 1600 °F to 1350 °F as one would expect by a $P_{SO_2} = 3.8 \times 10^{-3}$ and $P_{SO_3} = 1.5 \times 10^{-3}$ (maximum for 1350 °F according to Figure B-1), well above the $NaSO_4$ stability curve in Figure 3-1 and insuring that liquid salt is present at all temperatures, 1600 °F to 1100 °F. Figures 4-11 and 4-12 show the microstructures at 1500 °F and 1400 °F, respectively.

4.3 SODIUM AND POTASSIUM TEST RESULTS

With Tests 4, 5 and 6 (See Table 4-1) the effects of the K addition to the fuel was studied. At this time theoretical calculations had proceeded far enough to show that there would be little point in running a test with an SO_2 addition to the burner rig air if one wished to reach a sulfur level where low-temperature hot corrosion would be marginal. This conclusion follows from Figure 3-1, which shows far less sulfur is required to stabilize $CoSO_4$ in the presence of K. Therefore, Test 4 began with a small addition of sulfur to the

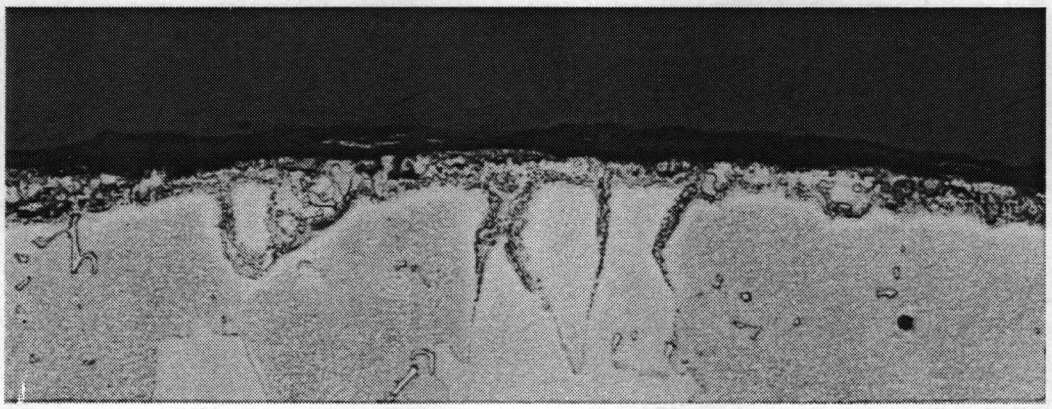

Figure 4-8. **Air-Cooled Small Burner Rig, IN-738, Test No. 2, 1600 °F specimen, 200X, 2-2-1 Etch.**

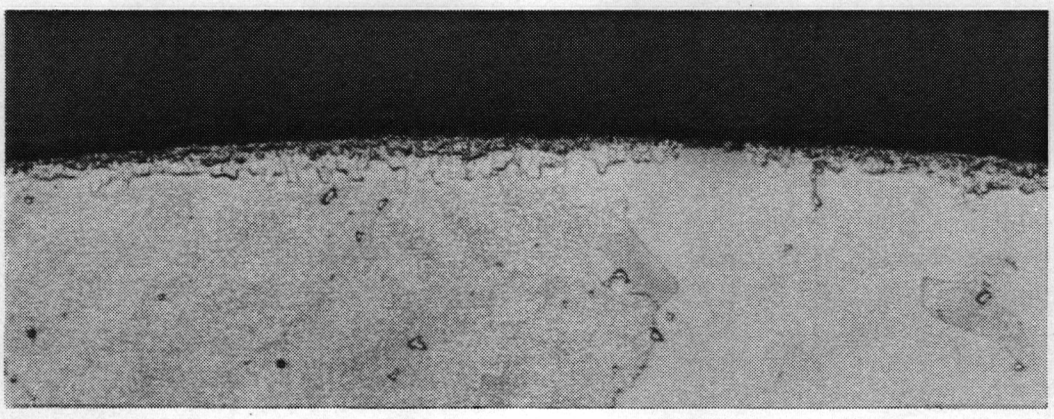

Figure 4-9. **Air-Cooled Small Burner Rig, IN-738, Test No. 2, 1500 °F specimen, 200X, 2-2-1 Etch.**

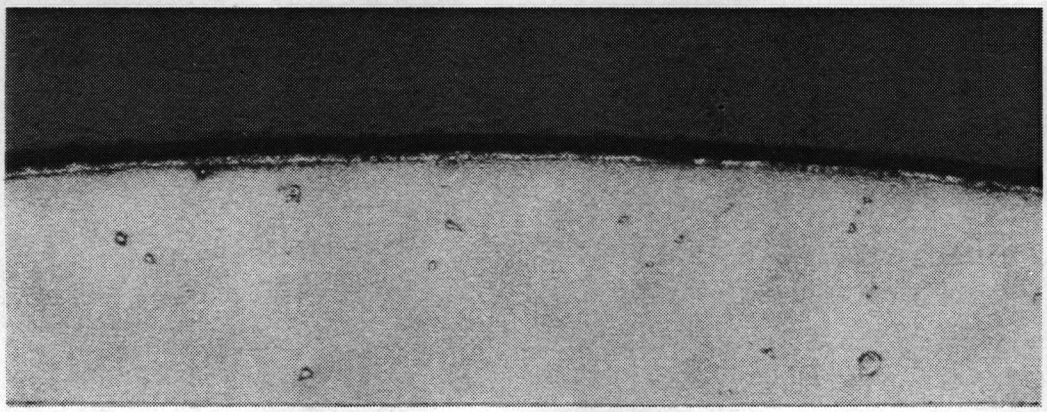

Figure 4-10. **Air-Cooled Small Burner Rig, IN-738, Test No. 2, 1400 °F specimen, 200X, 2-2-1 Etch.**

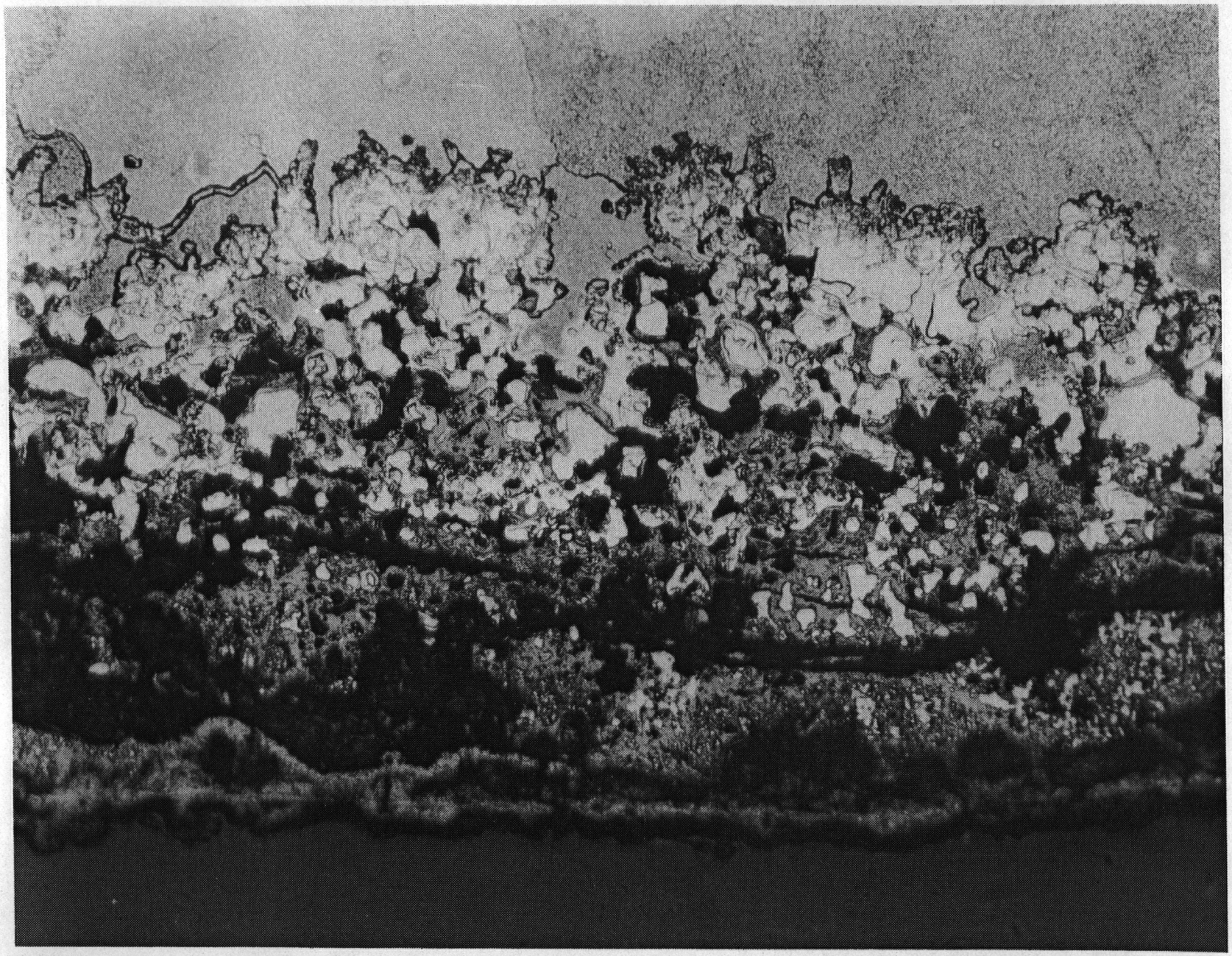

Figure 4-11. ACSBR, Test No. 3, 1500 °F, 200X, 2-2-1 Etch.

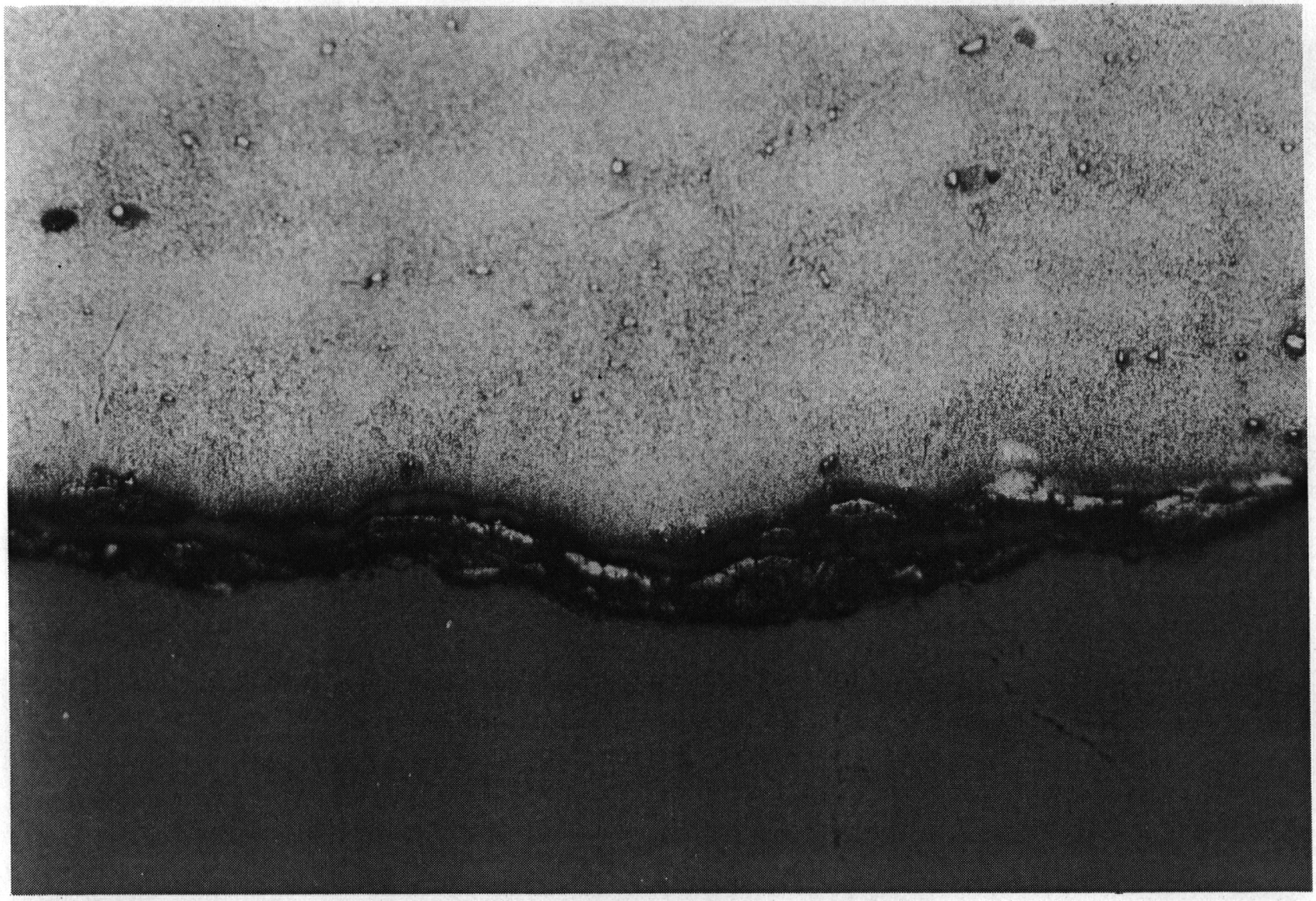

Figure 4-12. ACSBR, Test No. 3, 1400 °F, 200X, 2-2-1 Etch.

burner rig fuel (tertiary butyl disulfide) such that the sulfur pressure counted as SO_2 was $1.4x10^{-4}$ atm. This should give a $P_{SO_3} \approx 6x10^{-5}$ atm (maximum at 1350 °F according to Figure B-1), or somewhat above the mixed sulfate stability curve. Table 4-2 shows significant low-temperature corrosion did occur in this test. With this result Test 5 was run with only the sulfur present in the diesel fuel. In this case the $P_{SO_3} = 0.9x10^{-5}$ atm (maximum at 1350 °F according to Figure B-1), which is much nearer the stability line given in Figure 3-1. As the data shows in Table 4-2, corrosion in the low-temperature region (1400 °F-1100 °F) was substantially reduced.

Finally, to make certain that low-temperature corrosion could be eliminated in the presence of the mixed sulfates, the fuel sulfur level was further reduced in Test 6 by changing the burner rig fuel to kerosene. This reduced the fuel sulfur to 0.026% and $P_{SO_3} = 0.17x10^{-5}$ atm (maximum at 1350 °F according to Figure B-1). This reduction completely eliminated the corrosion in the region 1400 °F to 1100 °F, in agreement with the theoretical curve given in Figure 3-1.

Selected corrosion microstructures from Tests 4 and 5 are given in Figures 4-13 to 4-18. For Test 4, Figure 4-13 shows a high-temperature, hot corrosion structure with internal structure and Cr depleted zones (white metal). This structure does not change greatly until 1300 °F (Figure 4-14) where a typical low-temperature structure develops with layered oxide and no internal structure. Figure 4-15 shows the microstructure at 1100 °F. Some corrosion has occurred as shown by the scalloped surface, but the attack was little and the scale was not retained.

The microstructure for Test 5 at 1600 °F was similar to that for Test 4 at 1600 °F; however, the 1300 °F structure is different as shown in Figure 4-16. In Test 5 the 1300 °F corrosion is much less than for Test 4, and the scale is not layered and appears more protective. Some pins in this test appeared to show a real difference between upstream and downstream attack. This appeared in the 1500 and 1400 °F structures and is shown for the 1400 °F case in Figures 4-17 and 4-18. Apparently the salt conditions on the upstream side produced a liquid salt, whereas on the downstream side this did not occur. The 1400 °F upstream structure appears to be intermediate between low- and high-temperature corrosion.

It should be noted that Tests 2 and 5 were similar in terms of SO_x concentration in the combustion gases. The differences in these tests is K. The results in terms of corrosion (see Table 4-2) show what a potent effect has the K contaminant.

In Test 6 there was significant corrosion at 1600 °F, less corrosion at 1500 °F, and almost no corrosion at lower temperatures. Figures 4-19, 4-20, 4-21, and 4-22 show the corrosion structures. In Figure 4-19, the 1600 °F specimen has a high-temperature, hot-corrosion morphology showing a porous outer corrosion scale containing Cr depleted metal (white) and showing internal grain boundary attack. Figures 4-20a and 4-20b show how the attack at 1500 °F has become nonuniform, consisting of pits (Figure 4-20a) over a uniform background attack (Figure 4-20b). Figure 4-22 shows the minimal attack, which has occurred at 1300 °F. This was typical of the attack in the 1100 to 1400 °F temperature range. (Note the higher magnification for Figures 4-20b and 4-22).

Some of the deposits from Test 6 were highly colored. These colored deposits have not been seen before. The 1100 to 1400 °F specimens were bright orange, whereas the 1600 °F specimen showed a typical corrosion scale color of dull green and the 1500 °F specimen

Figure 4-13. ACSBR, Test No. 4, 1600 °F, 200X, 2-2-1 Etch.

Figure 4-14. ACSBR, Test No. 4, 1300 °F, 200X, 2-2-1 Etch.

Figure 4-15. ACSBR, Test No. 4, 1100 °F, 200X, 2-2-1 Etch.

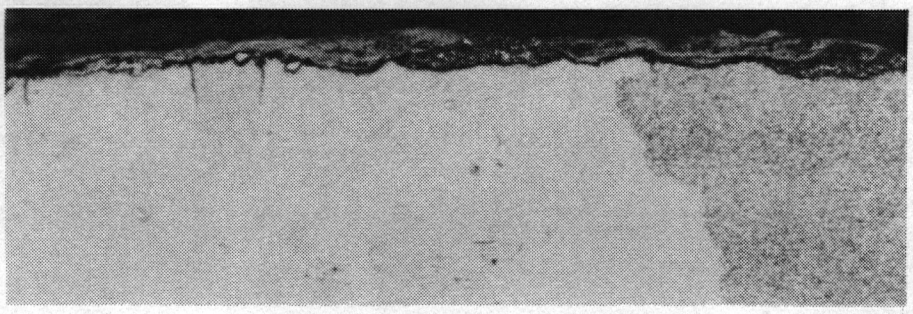

Figure 4-16. ACSBR, Test No. 5, 1300 °F, 200X, 2-2-1 Etch.

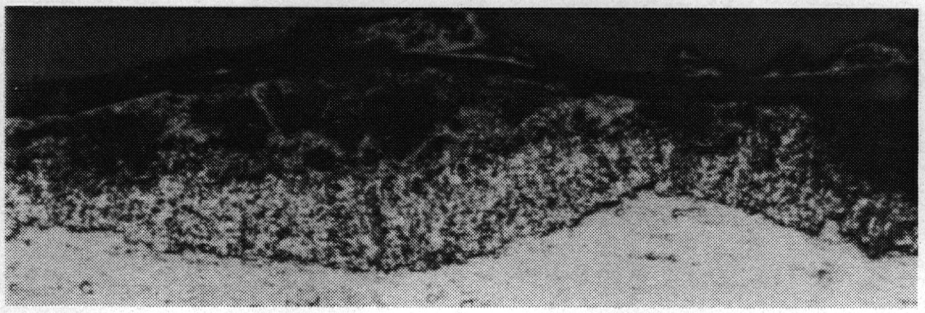

Figure 4-17. ACSBR, Test No. 5, 1400 °F, Leading Edge, 200X, 2-2-1 Etch.

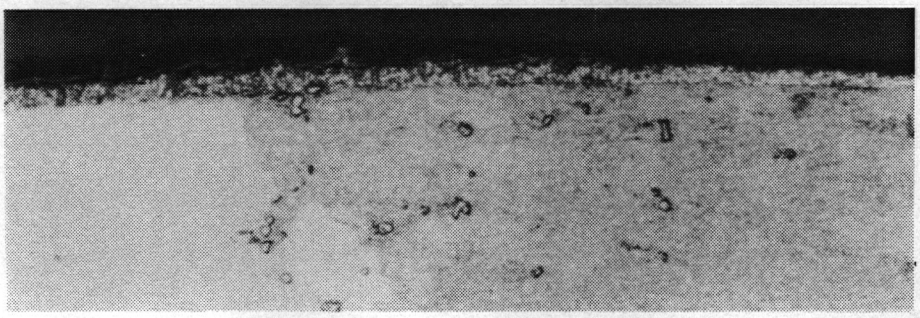

Figure 4-18. ACSBR, Test No. 5, 1400 °F, Trailing Edge, 200X, 2-2-1 Etch.

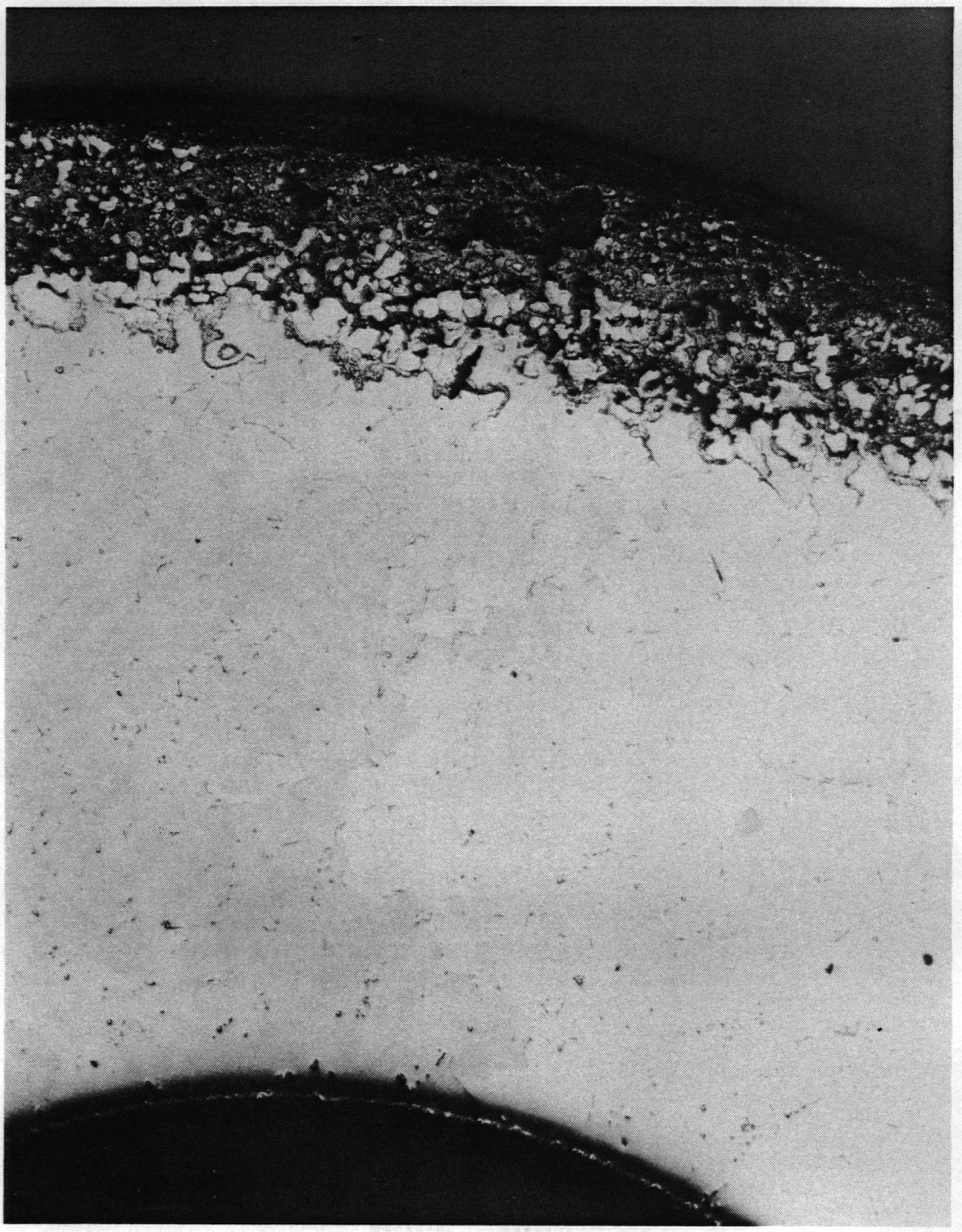

Figure 4-19. 1600 °F Specimen, ACSBR (etched 2-2-1) 100X.

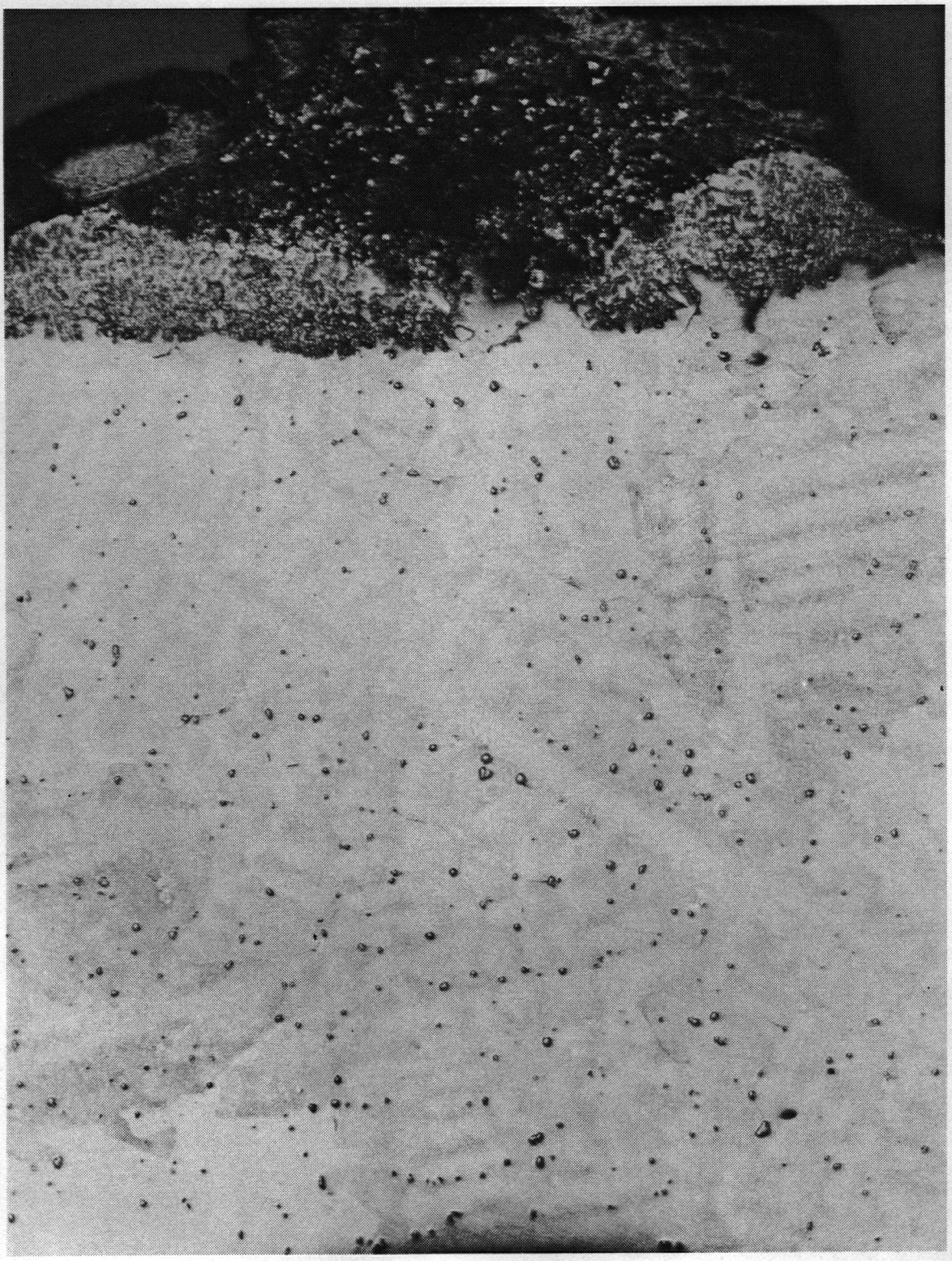

Figure 4-20a. 1500 °F Specimen, ACSBR, Area of Attack (etched 2-2-1) 100X.

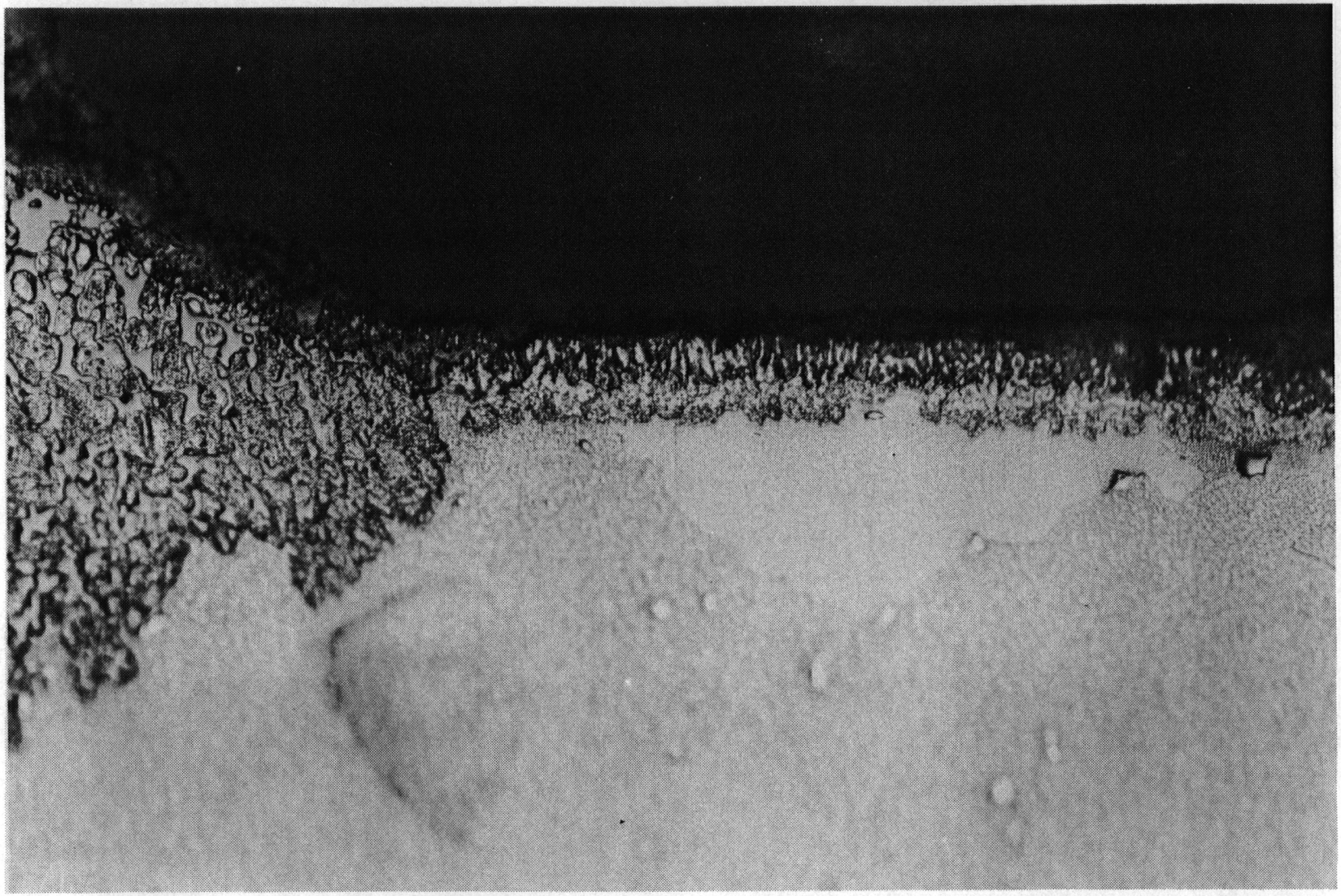

Figure 4-20b. **1500 °F Specimen, ACSBR, Area of Uniform Attack near a Pit (etched 2-2-1) 400X.**

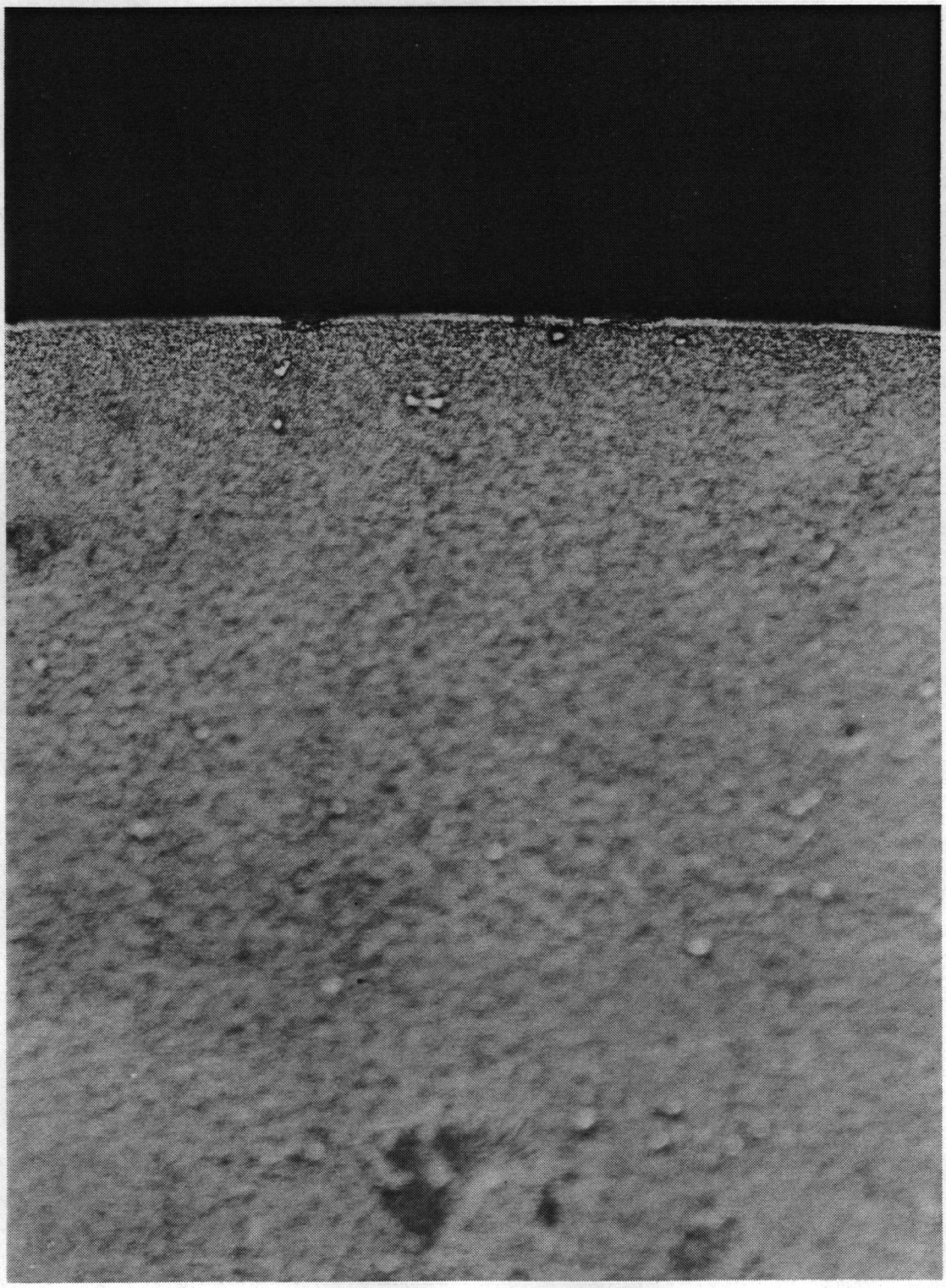

Figure 4-21. 1300 °F Specimen, ACSBR (etched 2-2-1) 400X.

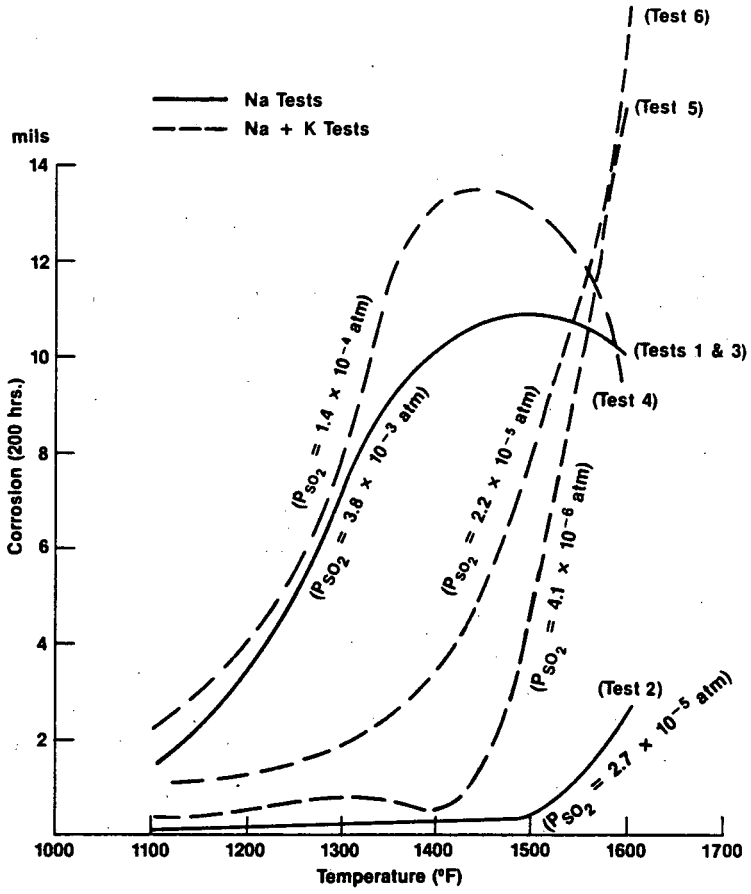

Figure 4-22. Corrosion versus Temperature.

showed no scale. All of the deposits were found to contain Cr. Some of the Cr on the lower temperature specimens must have been present in a chromate form. A complete deposit and corrosion scale chemical analysis is given in Section 4.6.

A summary of the corrosion data for the alkali tests (Tests 1-6) is given in Figure 4-22. These curves represent a best estimate based on the corrosion data from these tests and show clearly how a reduction in sulfur reduces the corrosion rate. They also show how the addition of K as a contaminant has an effect similar to raising the sulfur level; in this case the effect is about 28 times, comparing the curves for Tests 1 and 3 with Test 4, where they run together. Above about 1300 °F, the K effect is even stronger.

The corrosion attack at high temperatures was not diminished by the very low SO_2 level used in Test 6. It is thought this was due to the presence of the Na-K sulfate eutectic which allows the sulfate melt to be liquid down to about 1510 °F (as compared to pure Na sulfate which melts at 1630 °F) without the addition of any alloy sulfates.

4.4 ADDITIVE TESTS

Mg appears in dolomite used in gettering sulfur in PFBs, as was done during the LTMT program, and it appears as a constituent in these deposits along with Ca. Being one of the alkaline metals and being readily available in an oil soluble form, it was selected as the additive to try in these tests. Mg is used extensively in boilers and gas turbines for preventing the effects of vanadium corrosion. Also, it is used in preventing acid dew in stack emissions.

With Test 7, the first of three additive tests was begun. As shown in Table 4-1, the test involved the fuel contaminants Na and Mg. The relative amounts of Na and Mg would give a $NaSO_4$-$MgSO_4$ mixture in the deposit which would melt at about 1470 °F provided the proportions remained the same as in the fuel. With the presence of an additive, deposits were observed in all three tests, but they were only present in significant amounts for the specimens at 1400 °F and below.

In Test 7, the 1600 °F and 1500 °F specimens showed green and black oxide scales, the 1600 °F scale showing more green and the 1500 °F scale more black. These are typical hot corrosion and oxidation colors, respectively. Starting with the 1400 °F specimen, deposit formation was in the form of a brown-white deposit, and at lower temperatures the deposits were all white. The latter became quite thick, maybe 30 to 40 mils. The deposits were not mechanically strong and had poor adhesion. They were easily removed when the specimens were rinsed in water for chemical analysis, indicating they contained considerable water soluble material, $MgSO_4$. (The results of the chemical analyses appears in Section 4.6.)

Corrosion in Test 7 was minimal compared to Tests 1 and 3, which were identical tests in terms of the concentration of Na in the fuel and SO_x present in the combustion gases. This is shown in Table 4-2. Not only has the Mg additive reduced corrosion in the low-temperature regime (1400 °F-1100 °F), it has also reduced corrosion at 1600 °F and 1500 °F.

Figures 4-23 through 4-28 show the corrosion morphologies for Test 7. The 1600 °F morphologies shown in Figures 4-23a and 4-23b show some internal attack along grain boundaries under a somewhat uniform scale about 0.3 mils in thickness. This pin, at the place sectioned, probably ran closer to 1550 °F throughout most of the test according to its

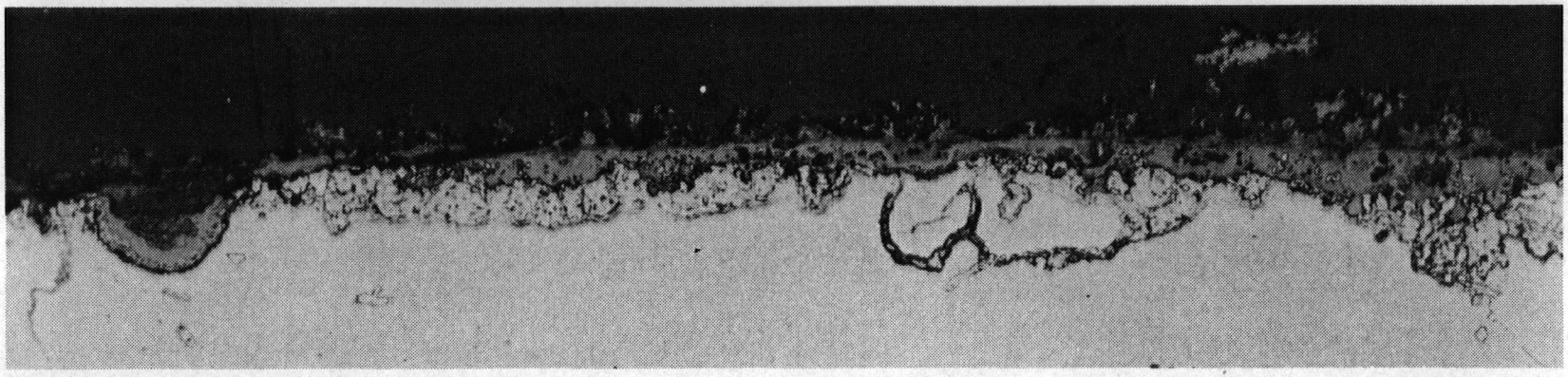

Figure 4-23a. 1600 °F Specimen, ACSBR (etched 2-2-1), 400X.

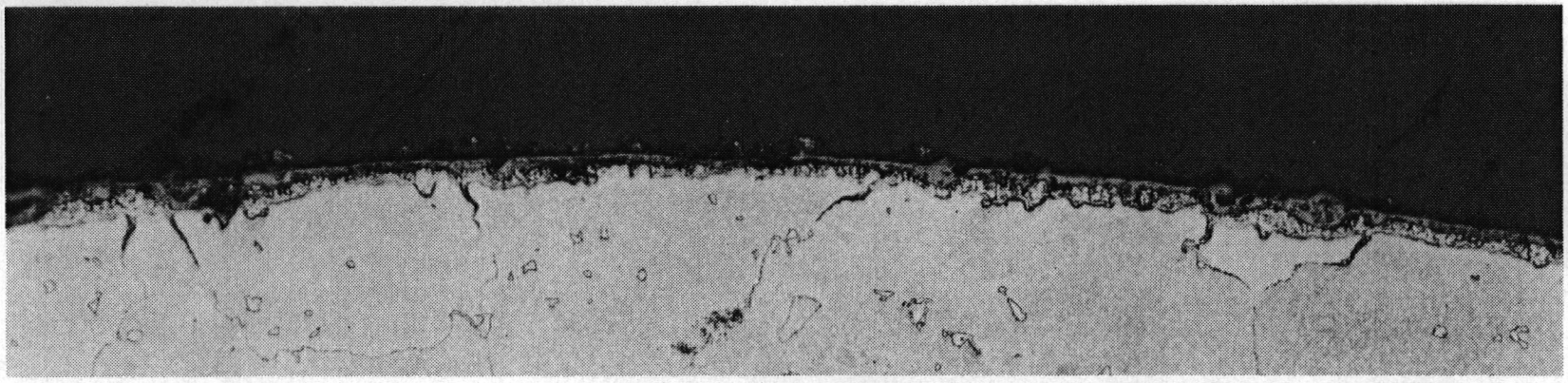

Figure 4-23b. 1600 °F Specimen, ACSBR (etched 2-2-1), 200X.

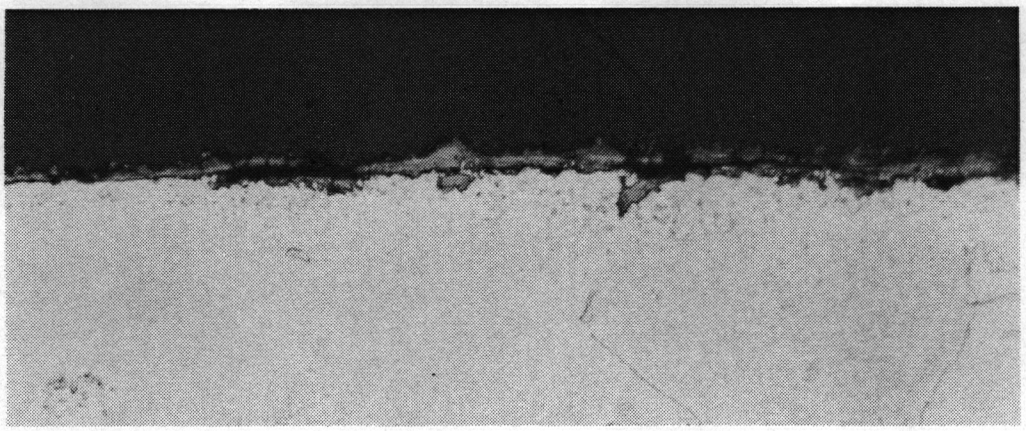

Figure 4-24. 1500 °F Specimen, ACSBR (etched 2-2-1), 400X.

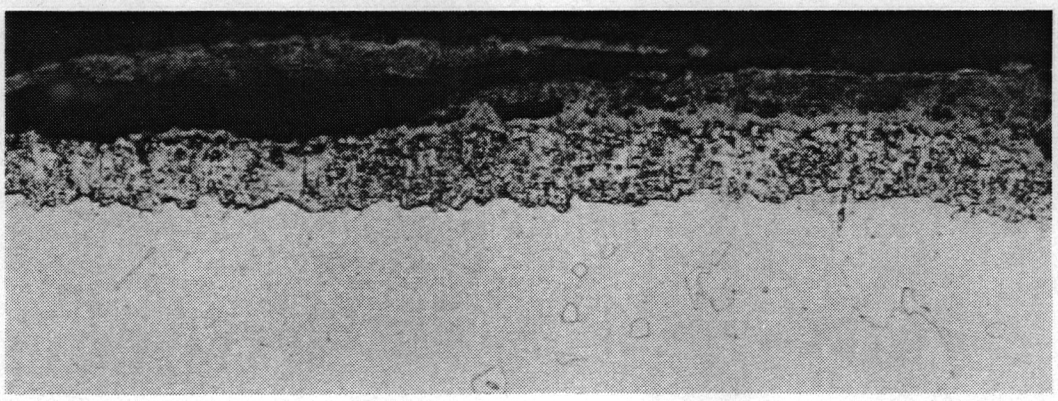

Figure 4-25a. 1400 °F Specimen, ACSBR (etched 2-2-1), 400X.

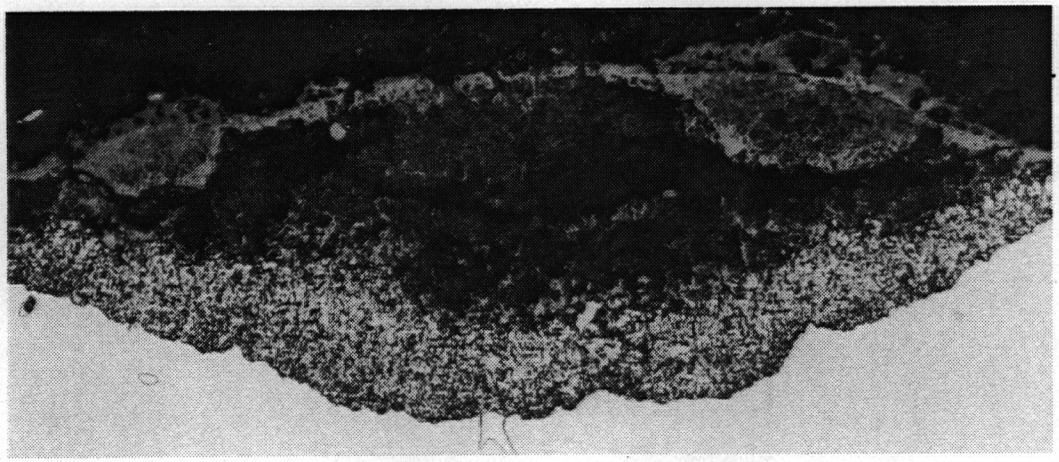

Figure 4-25b. 1400 °F Specimen, showing pit ACSBR (etched 2-2-1), 400X.

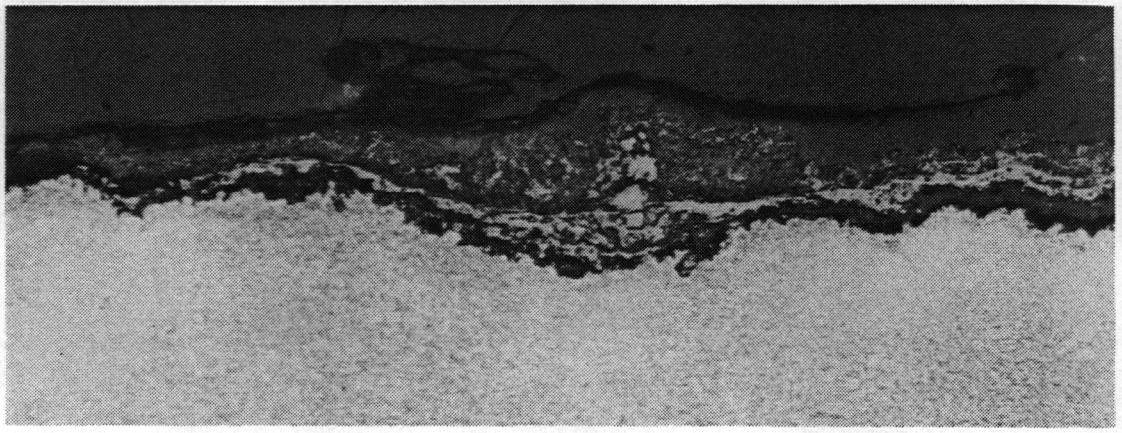

Figure 4-26. 1300 °F Specimen, ACSBR (etched 2-2-1), 400X.

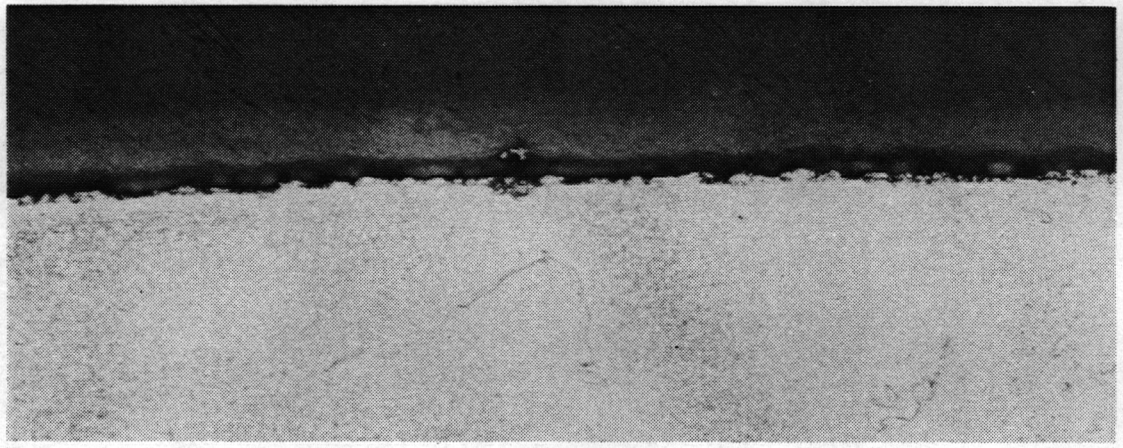

Figure 4-27. 1200 °F Specimen, ACSBR (etched 2-2-1), 400X.

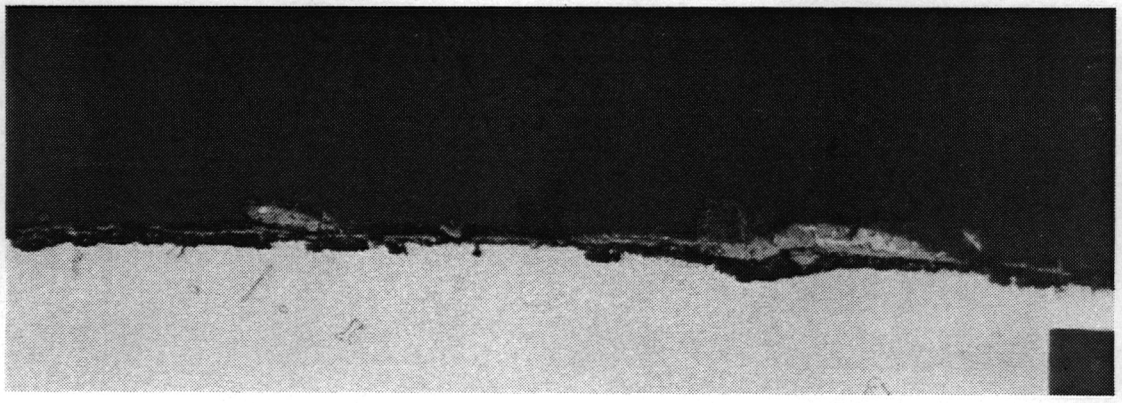

Figure 4-28. 1100 °F Specimen, ACSBR (etched 2-2-1), 400X.

attached thermocouple. Although the corrosion morphology is similar to that usually observed at this temperature, the amount of corrosion is considerably less than what would be expected from these contaminant levels as is shown by comparing Tests 1 and 3 with Test 7 in Table 4-2. At 1500 °F there was virtually no attack, but the beginning of some internal precipitation is visible beneath the scale as shown in Figure 4-24. Figures 4-25a and 4-25b show more significant attack is occurring at 1400 °F. The corrosion morphology is tending towards what is termed low-temperature, hot corrosion, but the rate of attack is much lower than what would be expected were Na the only fuel contaminant. At 1300 °F low-temperature, hot-corrosion attack is occurring as shown in Figure 4-26. Little attack took place at 1200 °F or 1100 °F. The microstructures for these two specimens are shown in Figures 4-27 and 4-28.

The reason Mg inhibits the corrosion rate is not well understood. For Test 7, in which a Mg additive was added to the fuel, the corrosion rate definitely appears to be reduced compared to what would have occurred were only Na present in the fuel. One may speculate that the reason for this is that the Mg in some way is inhibiting the arrival of dissolved SO_3 at the metal oxide surface. There are several ways one could envision that this might occur.

The Mg additive, which is a commercially available fuel additive, is a combination of oil soluble magnesium sulfonate and dispersed magnesium carbonate. It is believed when a fuel droplet is burned that the Mg ash particle probably takes the form of an oxide particle. This is certainly the stable form of Mg at flame temperatures. The particle, however, begins to convert to sulfate when it leaves the flame zone and is mixed with dilution air and becomes part of the combustion gases, (maximum combustion gas temperature in these tests is 1600 °F) depending on the SO_x pressures. In Test 7, the SO_x pressure is quite high and the stable form of Mg is the sulfate. It is likely the Mg ash particle has not converted to sulfate by the time it impacts a corrosion pin. Upon reaching the surface of a corrosion pin, the MgO ash particle becomes a source to consume SO_3 and prevent the formation of alloy sulfates.

Another possibility is that a Na_2SO_4-$MgSO_4$ liquid appears on the surface of a pin (the eutectic temperature is below 1300 °F) and precludes the environment from making direct contact with the metal oxide interface and delays formation of alloy sulfates. In contrast with Na_2SO_4 alone, initially there is only a solid, and access to the surface by SO_x is much easier and hence the initial formation of alloy sulfates is easier.

Since the phase diagram for the Na_2SO_4-$MgSO_4$ system shows compound formation, the speculation is that the activity of Na_2SO_4 is reduced by the addition of $MgSO_4$. By the reaction of $Na_2SO_4 + SO_3 = Na_2S_2O_7$ at the gas-salt interface, the activity of pyrosulfate is lowered by a reduction of the sulfate activity, the partial pressure of SO_3 being fixed by the environment. If the concentration of pyrosulfate is also lowered, then there should be less pyrosulfate being transported to the salt-oxide interface, which should lead to a reduction in the formation of $CoSO_4$ and ultimately to a reduction in the rate of corrosion.

In Test 8 both Mg and V were fuel additives. The reason behind the selection of V was as follows. In low-temperature, hot-corrosion SO_3 in the combustion gases reacts with Co and Ni in the alloy to form alloy sulfates. These alloy sulfates mix with alkali sulfates to form a low melting liquid. It is the low melting liquid that is believed to be necessary for hot corrosion. It is reasoned that the low melting liquid could be prevented from forming if the Co and Ni in the alloy could be prevented from forming sulfates. From heavy fuel

experience in gas turbines, it has been observed that Co and Ni vanadates do form. Thus, Test 8 was an attempt to reduce low-temperature, hot corrosion by introducing V to the fuel, assuming alloy vanadates would form and prevent the formation of a low melting point liquid.

A thermodynamic investigation of the competition between vanadate and sulfate was made. The details of this study are given in Appendix C. Of course the presence of V in a fuel can cause severe corrosion because of the formation of V_2O_5 (melting point 1270 °F). Mg is a very effective additive in preventing this and hence its presence in Test 8.

The specimens from Test 8 also had deposits. The 1600 °F and 1500 °F specimens had only slight deposits, which were brown over yellow in color. The 1400 °F specimen had a thick deposit, which consisted of brown over yellow over white. This deposit had some mechanical strength, unlike the deposits formed in Test 7, and it showed good adhesion to the underlying metal. The 1300 °F deposit was white with some patches of yellow. It was also strong and well bonded. The 1200 °F and 1100 °F deposits were white and not nearly as strong or well bonded.

The deposits at 1400 °F and 1300 °F proved not to be very water soluble when rinsed in water. The deposits at 1200 °F and 1100 °F were removed by rinsing in water. Chemical analysis data are given in Section 4.6.

Photomicrographs of the specimens from Test 8 are shown in Figures 4-29 through Figure 4-32. At 1600 °F there is light corrosion as was also true at 1500 °F (not shown). Compare this to Figures 4-2 and 4-11 noting the change in magnification. At 1400 °F light pitting attack is observed with some internal attack. Again compare this to Figure 4-12, which looks similar but which has 5 to 10 times the amount of metal loss according to Table 4-2. This is because at the lower temperatures the corrosion scale is not always adherent. (A comparison with the 1400 °F specimen in Test 1 cannot be made because as pointed out it lost cooling air during that test and probably saw conditions more like the 1600 °F specimen.) Figure 4-31 shows a scalloped surface for the 1300 °F specimen with no internal attack. The metal loss here is quite small. This is to be compared with Figure 4-5, and a difference in corrosion between the two specimens amounting to a factor of 18 as given in Table 4-2. The 1200 °F and 1100 °F specimens were essentially without corrosion. Figure 4-32 shows the 1200 °F specimen. Figure 4-6 shows the corresponding specimen from Test 1.

Tests 7 and 8 were the same tests in terms of Na and the SO_x levels in the combustion gases (see Table 4-1). In terms of corrosion, Table 4-2 shows there is little to choose in terms of which additive system was more effective. Because of this, Mg alone was chosen as the additive in Test 9, where both Na and K were present in the fuel. In terms of the corrosion causing contaminants present, Test 9 was the most aggressive test run. None of the Na plus K tests (4, 5 and 6) were run at such high sulfur levels. Test 4 is the closest, but its sulfur level was 27 times lower than that of Test 9. It is remarkable that the Mg additive was just as effective in the mixed alkali system as it was in Tests 7 and 8, where only Na was present.

The deposits in Test 9 again were confined to the specimens at 1400 °F and below. These deposits were beige to white as the temperature went from 1400 °F to 1100 °F. At 1400 °F there were many hard light-brown-colored nodules attached to the specimen surface. These had good adhesion with the specimen surface. As the temperature decreased

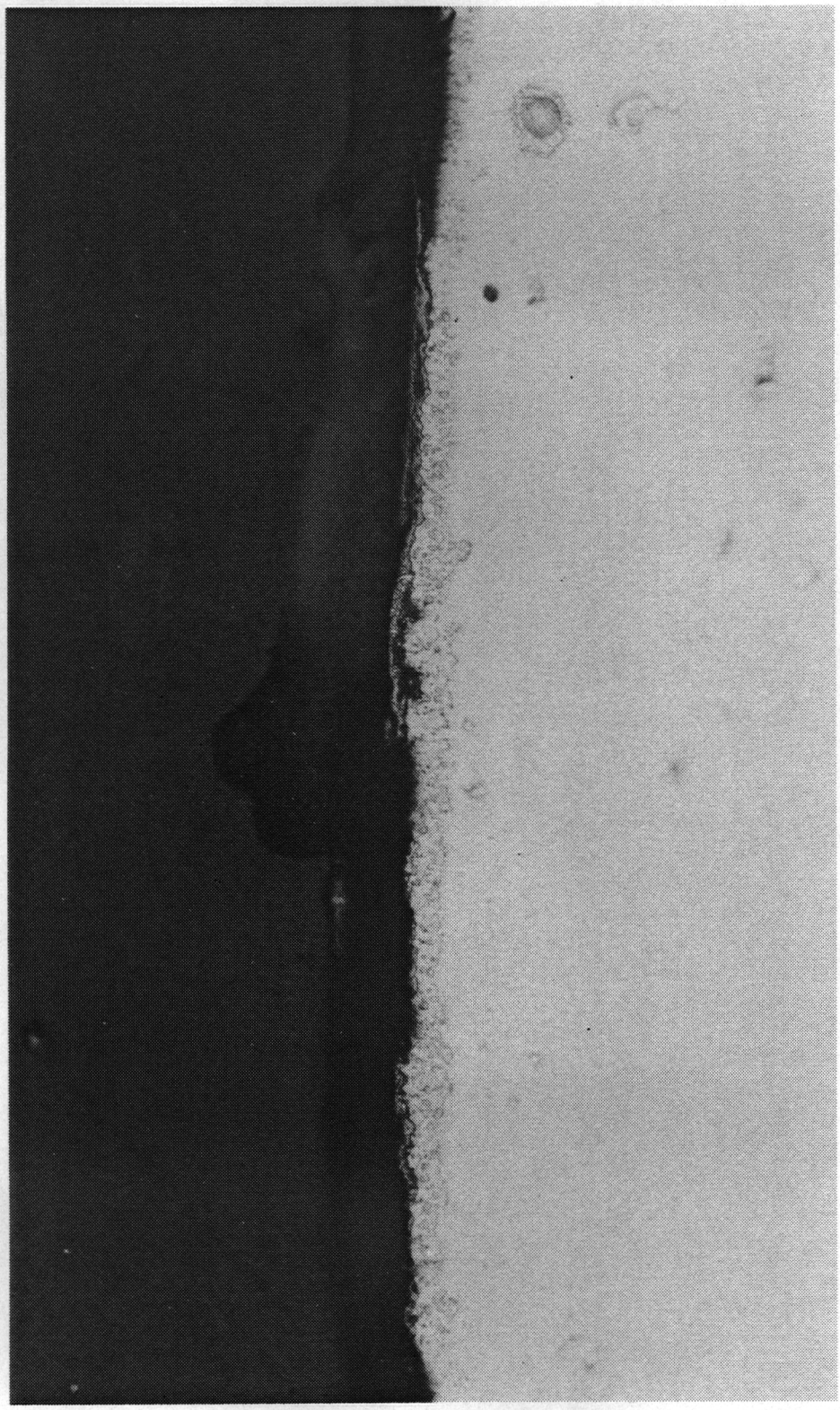

Figure 4-29. 1600 °F Specimen, Test 8 (etched 2-2-1), 400X.

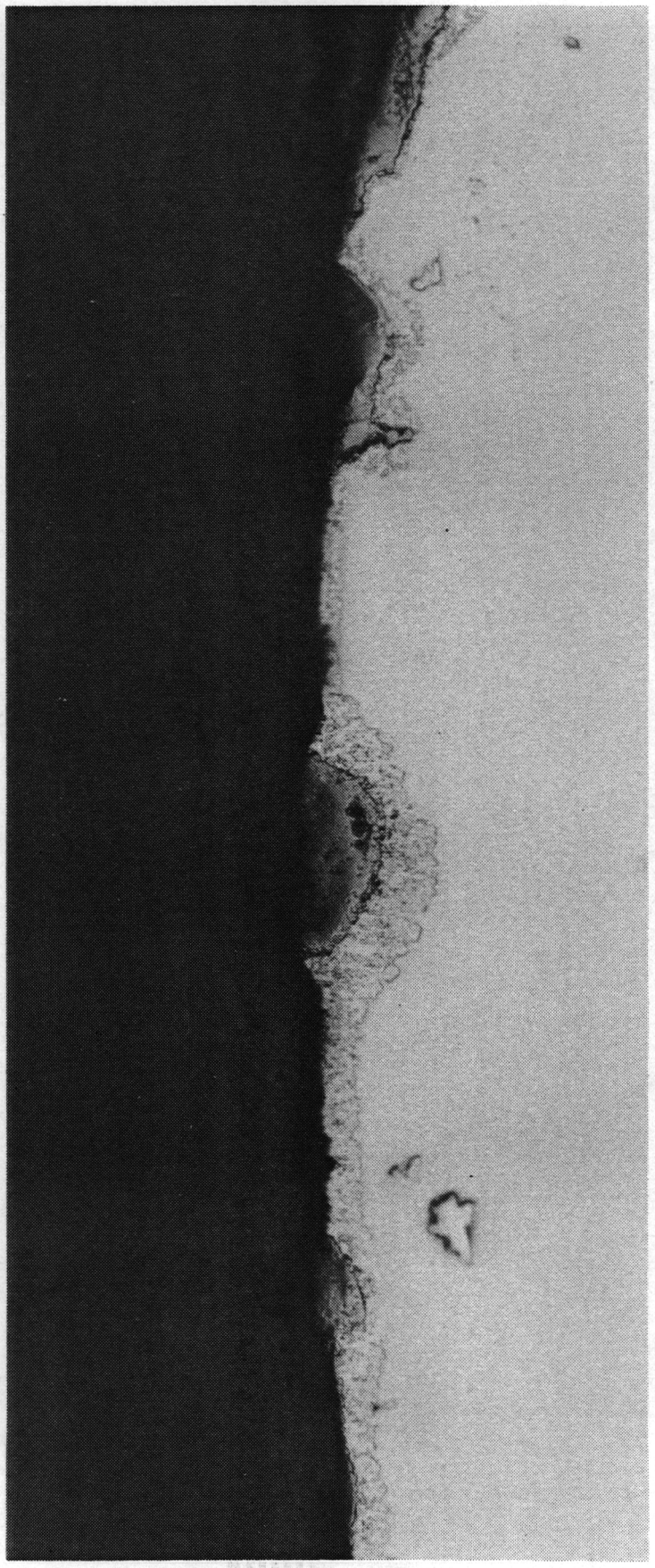

Figure 4-30. 1400 °F Specimen, Test 8 (etched 2-2-1), 400X.

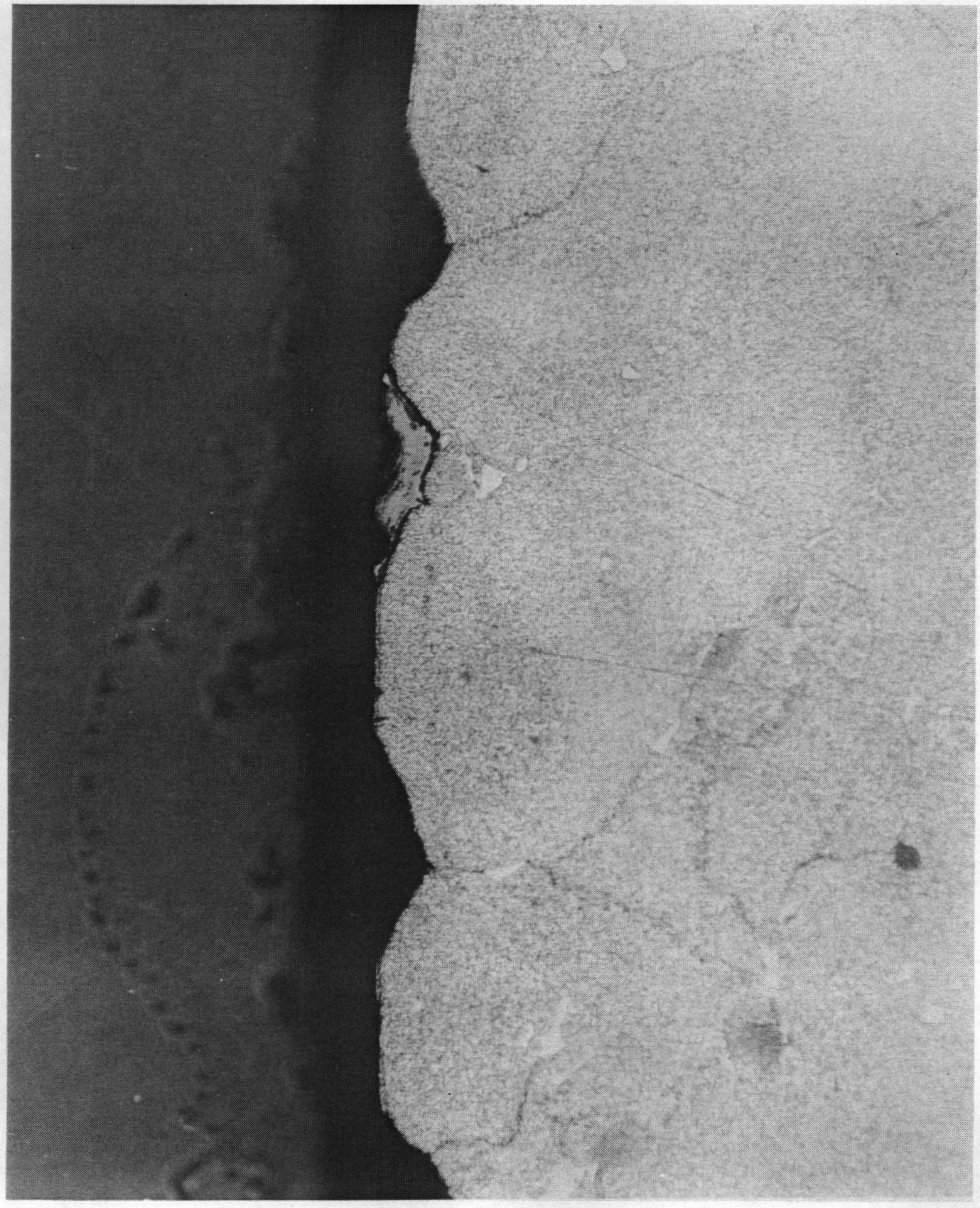

Figure 4-31. 1300 °F Specimen, Test 8 (etched 2-2-1), 400X.

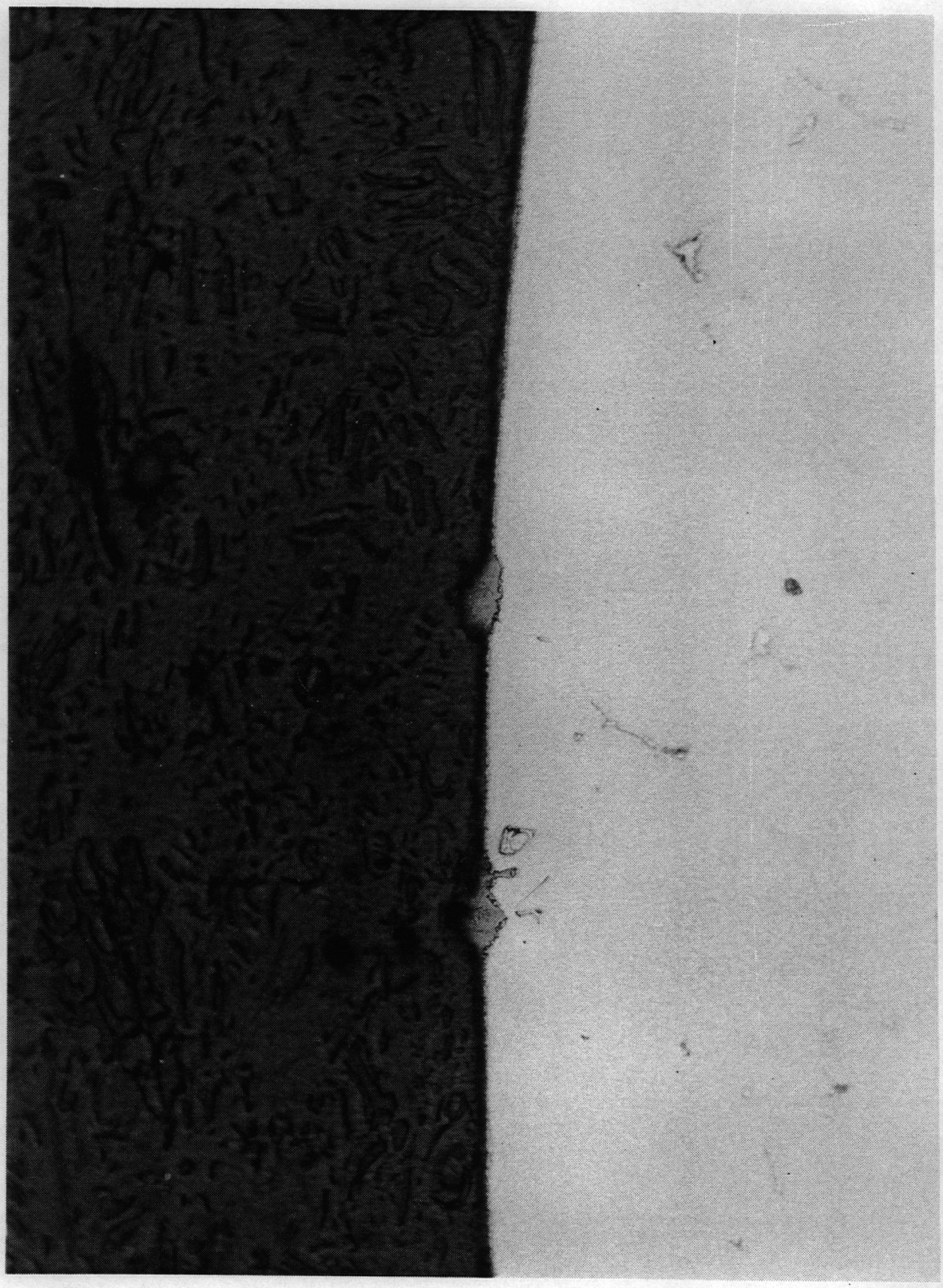

Figure 4-32. 1200 °F Specimen, Test 8 (etched 2-2-1), 400X.

the number of nodules decreased. The deposits were readily removed by water rinsing except for the nodules. However, these could be easily removed by brushing after the deposits were rinsed.

Figure 4-33 shows a photomicrograph of the 1600 °F specimen. A thin oxide scale covers the surface with some internal attack occurring beneath. The corrosion attack is minimal. The 1500 °F specimen is similar as shown in Figure 4-34. The 1400 °F specimen shown in Figure 4-35 is showing low-temperature attack with corrosion pitting. Some internal attack is present beneath the pit and elsewhere indicating this corrosion morphology is intermediate between low-temperature, hot-corrosion (layered scale, pitting, no internal attack) and high-temperature, hot corrosion (voluminous scale, internal attack, grain boundary attack). Figure 4-36 shows the 1300 °F specimen with its layered structure and no internal attack. The specimens at 1200 °F and 1100 °F showed no attack.

4.5 MICROPROBE ANALYSES OF SELECTED SPECIMENS

Microprobe work was done on selected low-temperature corrosion specimens from the high SO_x, Na and K contaminant tests (Tests 1, 3 and 4). Figure 4-37 shows the current image of the corrosion scale for the 1300 °F specimen in Test 1. Figure 4-38 shows the sulfur map for this structure. It is similar to what was found for the 1300 °F specimen for the LTMT-PFB (see Figure 2-8b). It is noted that the sulfur resides in bands near the bottom of the scale. Figures 4-39, 4-40, and 4-41 are the probe maps for Ni, Cr, and Al, respectively. Like the sulfur map they show bands in the lower scale. Some portions of the high sulfur bands correspond to portions of the low Cr bands and places where the Ni is high. The high Al bands appear to be just at the margin of the high sulfur bands in many places. In the case of Al there is also a high concentration of this element at the outer margin of the scale. Cr is not present in this outer portion, only some Ni along with the Al. The large black diagonal band in these maps is where the scale has separated and only mounting material is present. Other elements were looked at in the Test 1 specimen. The Ti, W and Co maps are given in Figures 4-42, 4-43 and 4-44.

Microprobe results of the 1400 °F specimen from Test 3 are as follows. Figure 4-45 shows the current image of a corroded area showing scale and internal sulfides in the metal matrix beneath the scale. Figure 4-46 is the sulfur map of this area. It shows the presence of the internal sulfides in the metal matrix and also sulfides in the scale. These sulfides are to be associated with Cr and Al, and the Cr and Al maps are given in Figures 4-47 and 4-48, respectively. A Ni map is shown in Figure 4-49. It is noted that the Ni is not associated with the sulfides and indeed the dark spots in the sulfur band (right-hand side) for the metal matrix sulfides correspond to high (bright) Ni areas on the Ni map, and absent (dark) Cr areas on the Cr map. These are called depleted areas in the metal matrix. The sulfides surrounding the depleted areas are almost entirely Cr. This region corresponds to the black band in the Al map where no Al is present.

Ti was found to be absent from the metal matrix internal sulfides. (The large particle just within the metal matrix is an MC carbide containing a high concentration of Ti.) Some Ti is present in the sulfides in the scale. The outer oxide scale is mostly Al, and a little way in, Cr is also present.

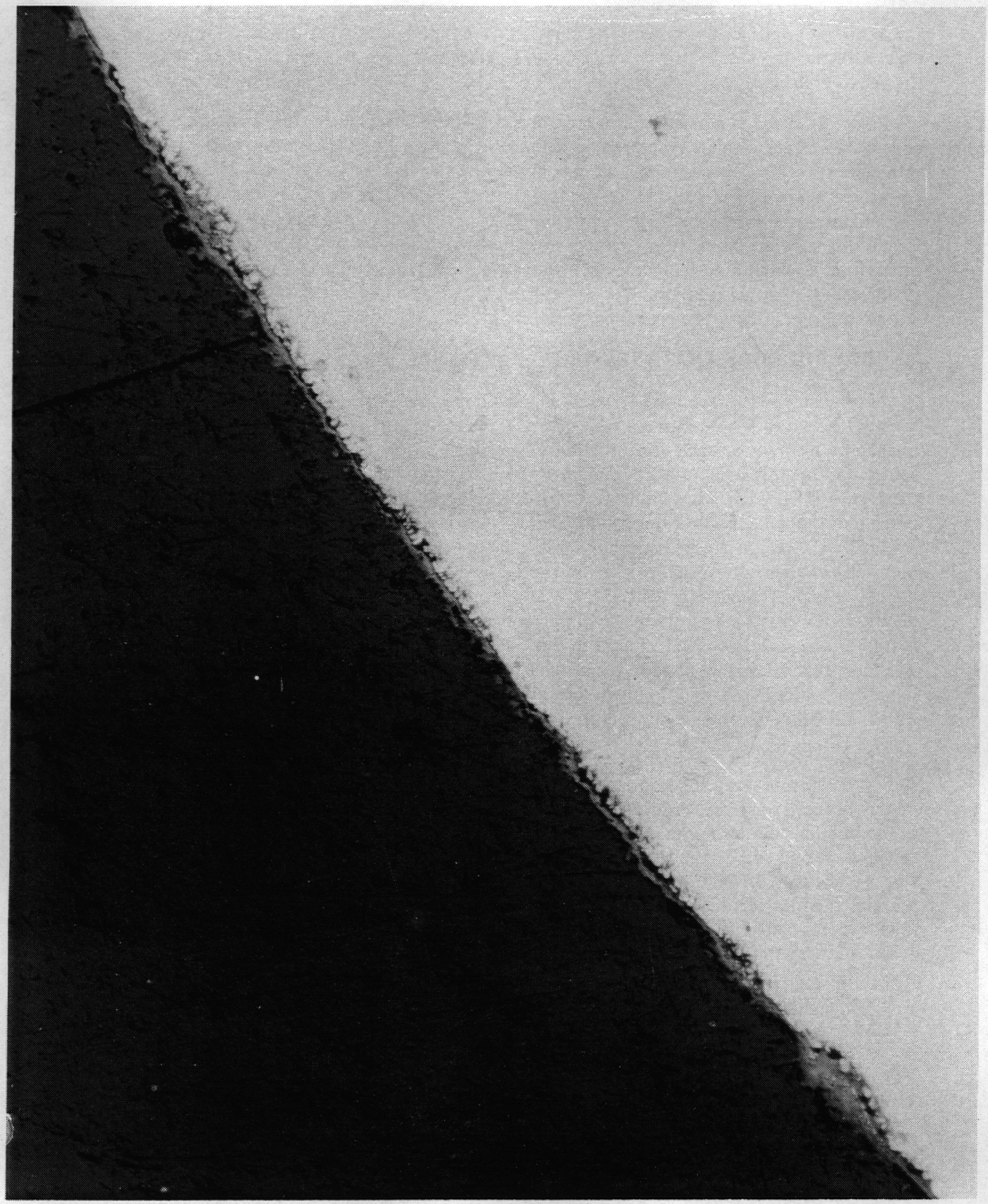

Figure 4-33. 1600 °F Specimen, Test 9 (etched 2-2-1), 400X.

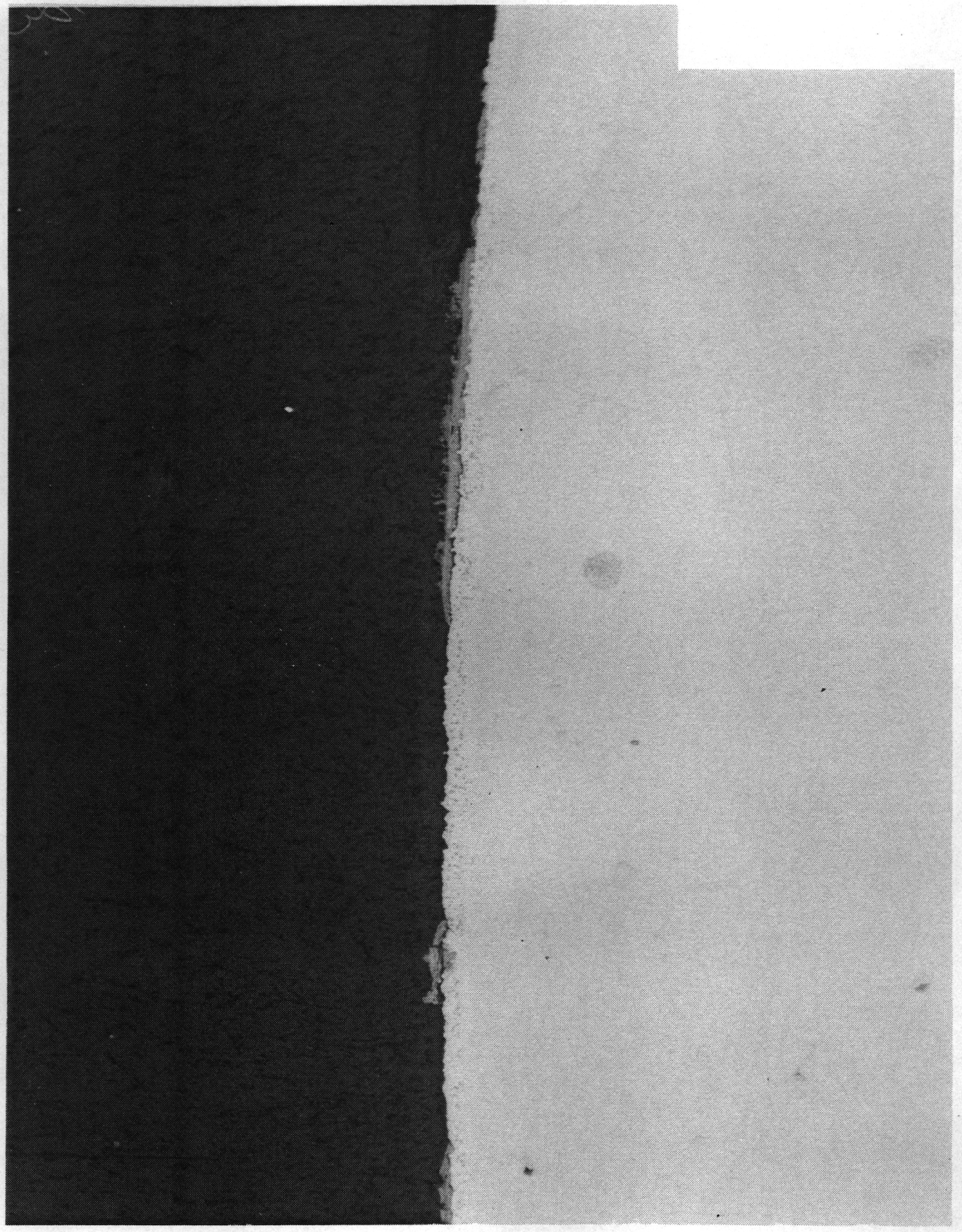

Figure 4-34. 1500 °F Specimen, Test 9 (etched 2-2-1), 400X.

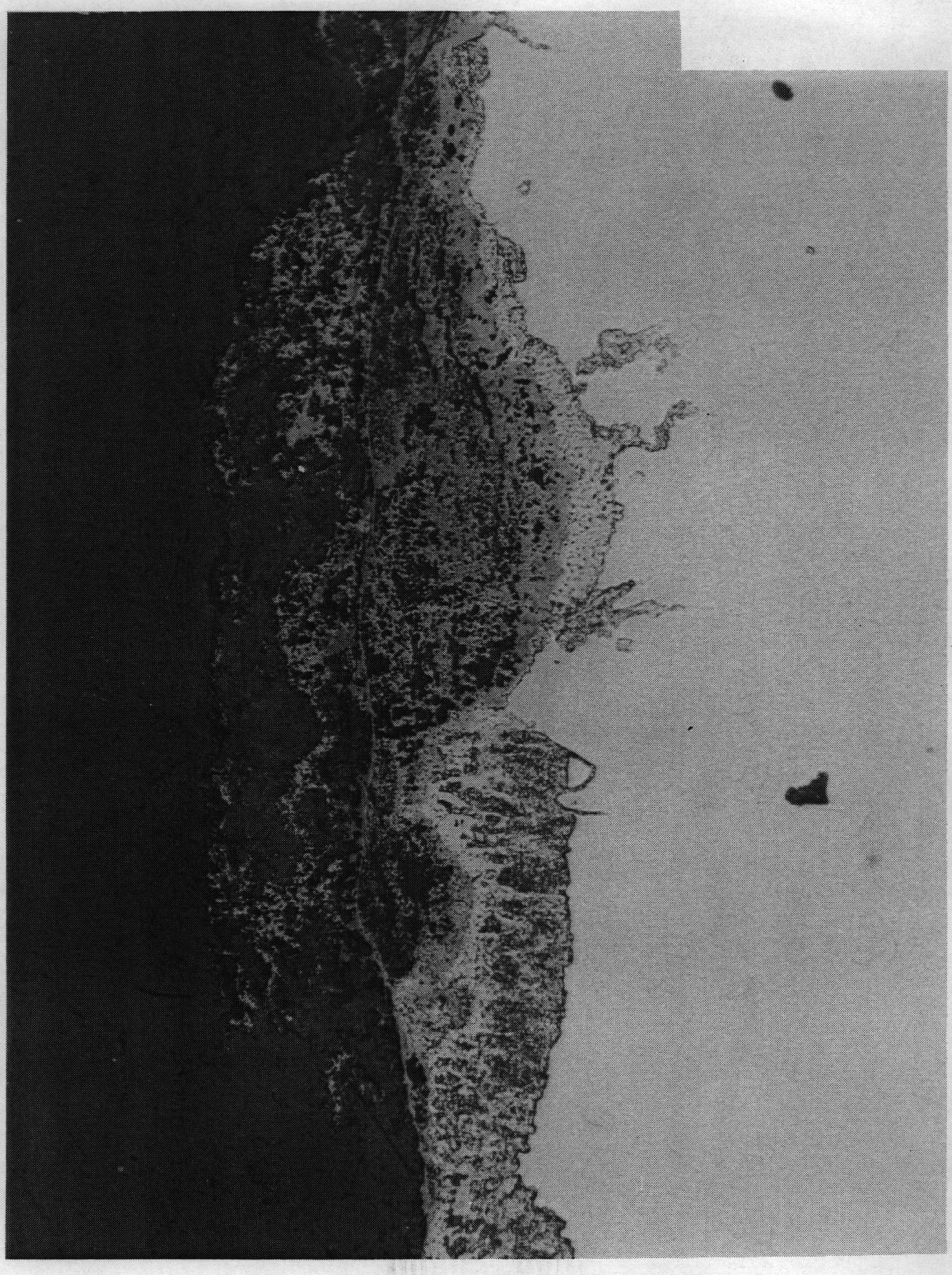

Figure 4-35. 1400 °F Specimen, Test 9 (etched 2-2-1), 400X.

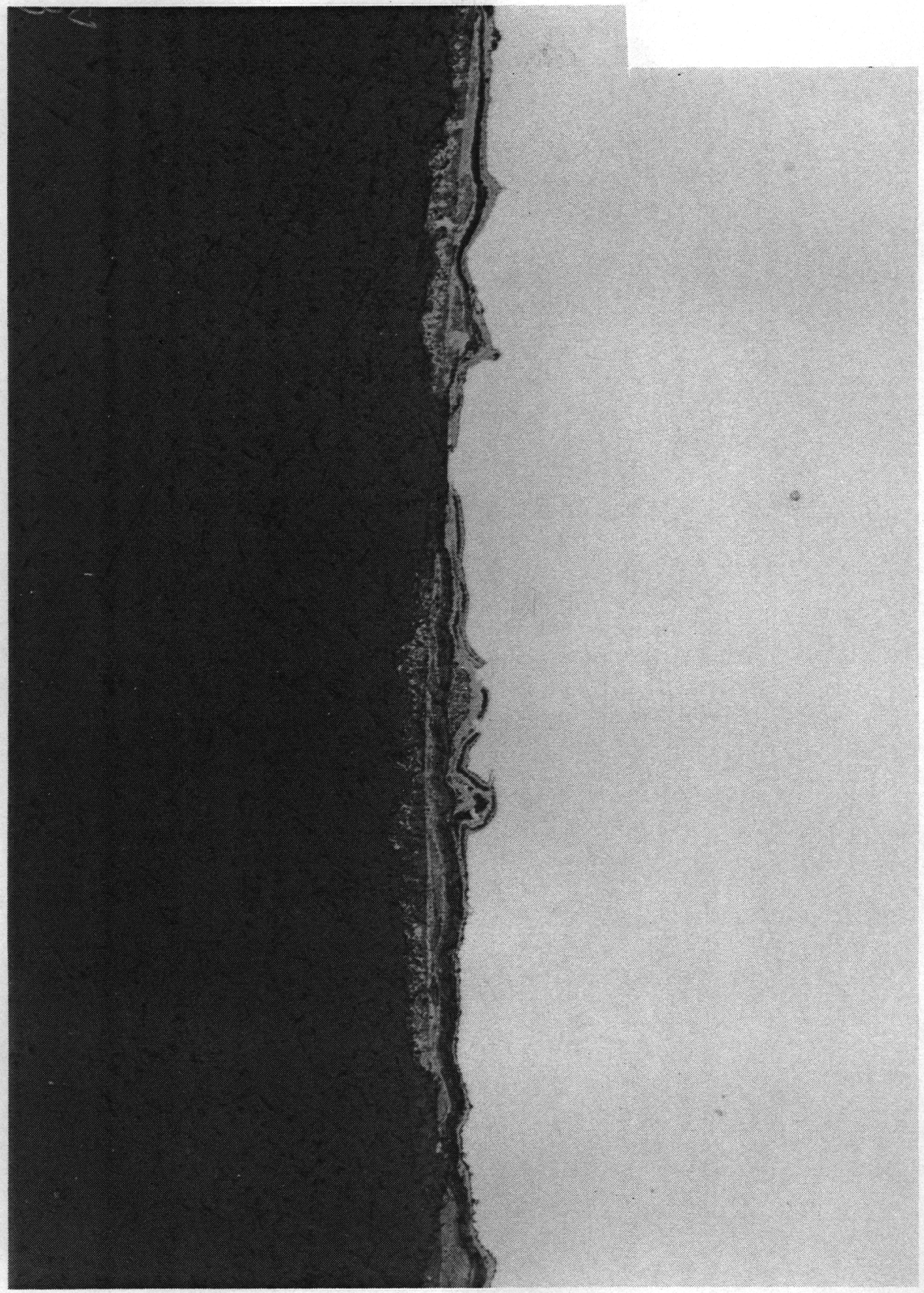

Figure 4-36. 1300 °F Specimen, Test 9 (etched 2-2-1), 400X.

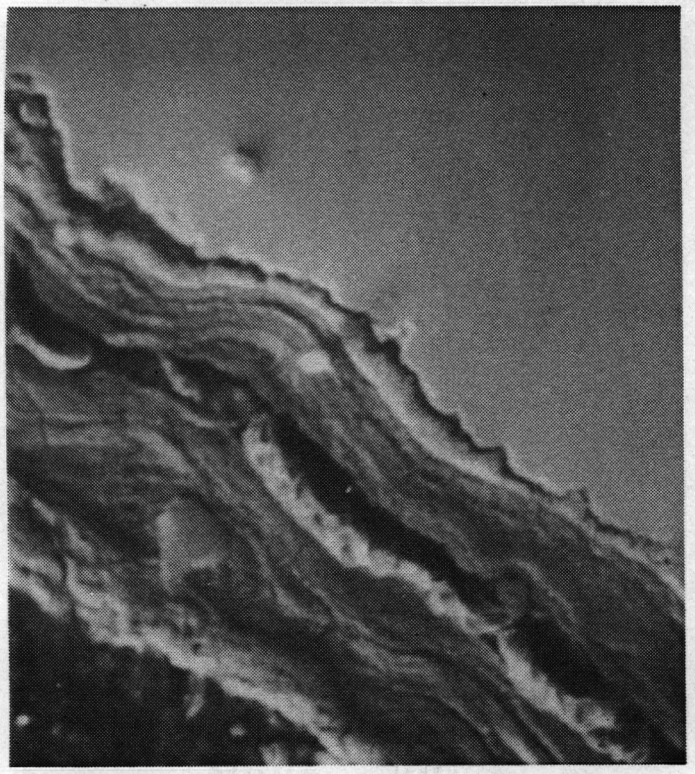

Figure 4-37. Test 1, Specimen Image, 1000X.

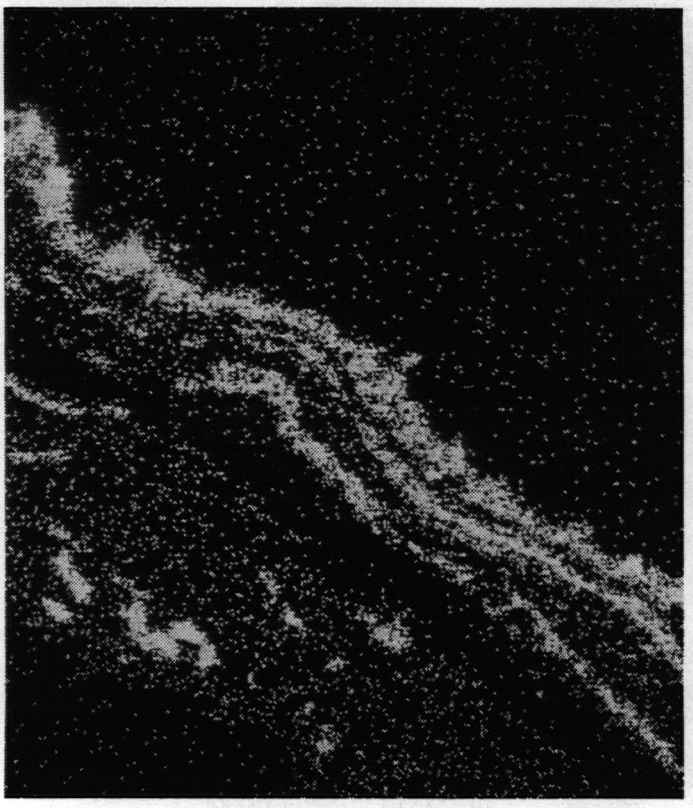

Figure 4-38. Test 1, Sulfur Map, 1000X.

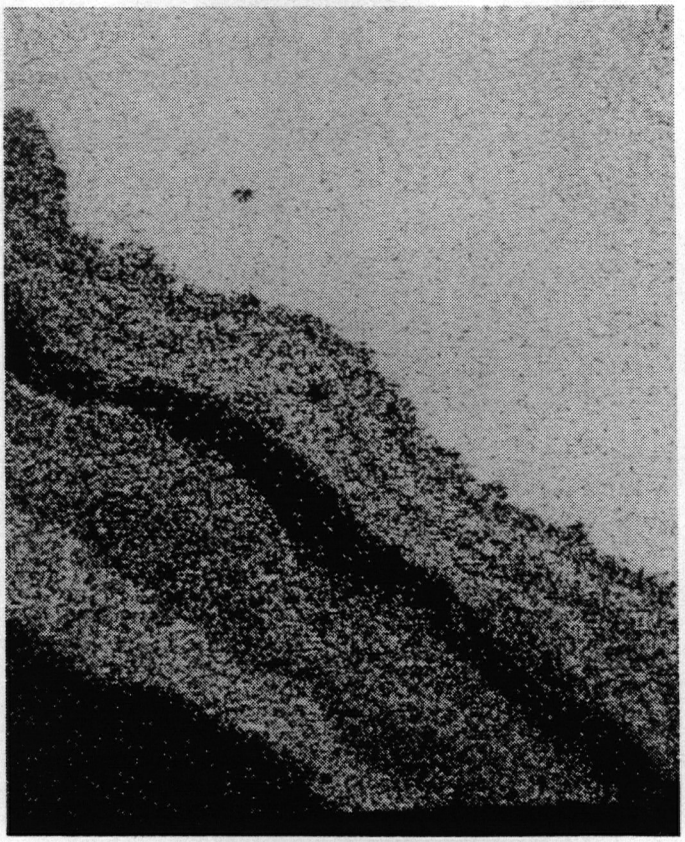

Figure 4-39. Test 1, Ni Map, 1000X.

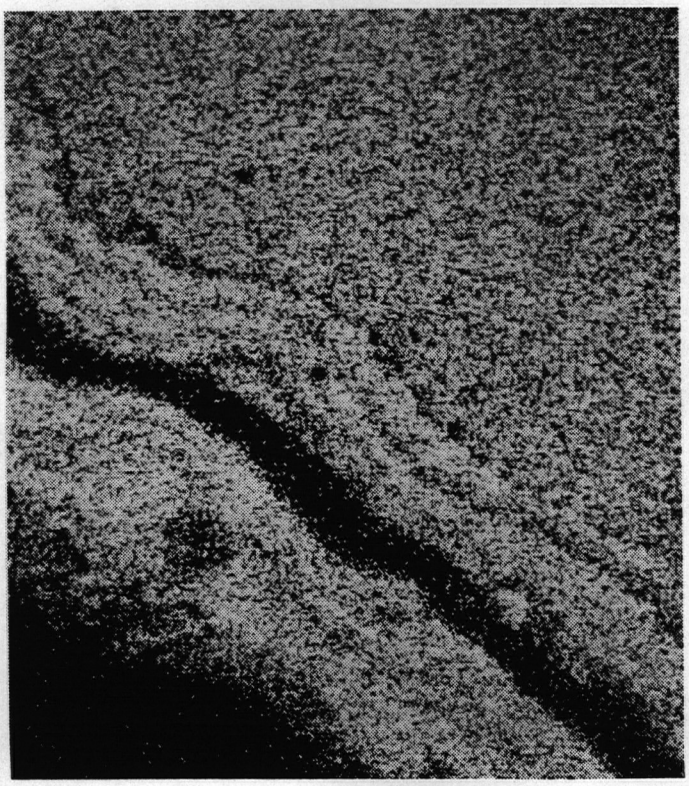

Figure 4-40. Test 1, Cr Map, 1000X.

Figure 4-41. Test 1, Al Map, 1000X.

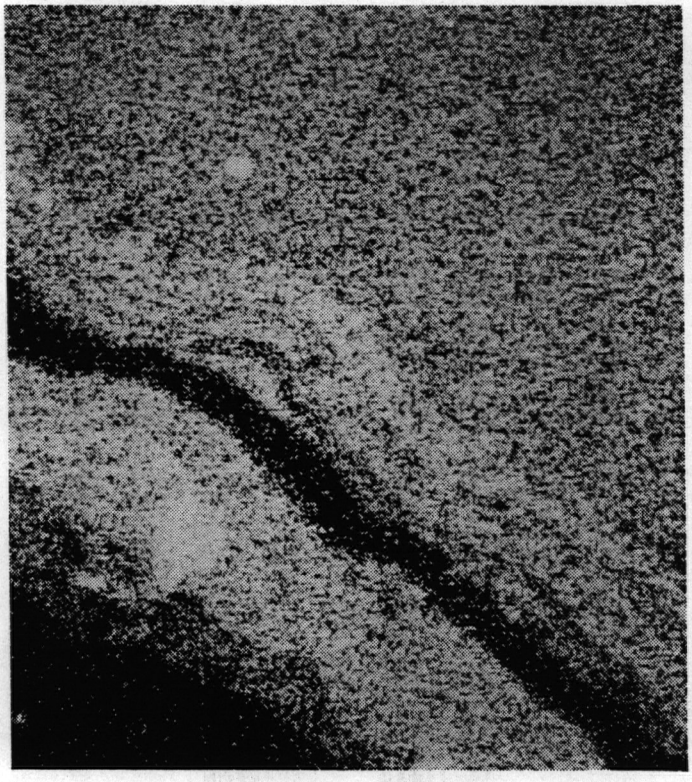

Figure 4-42. Test 1, Ti Map, 1000X.

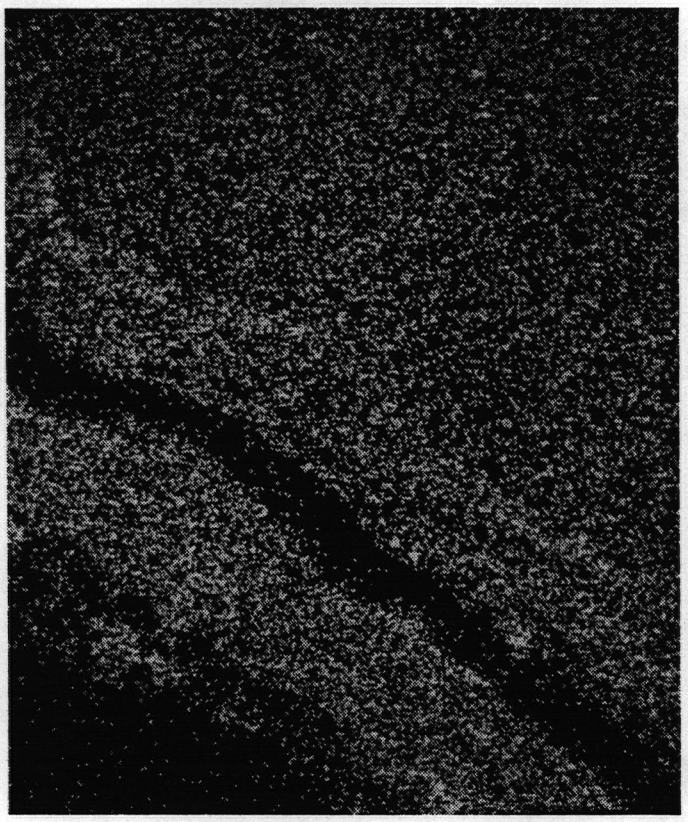

Figure 4-43. Test 1, W Map, 1000X.

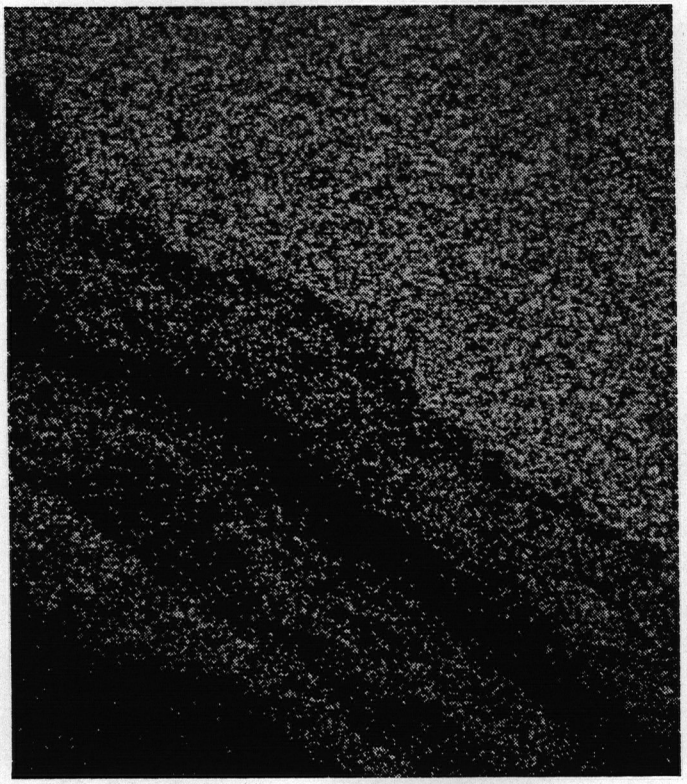

Figure 4-44. Test 1, Co Map, 1000X.

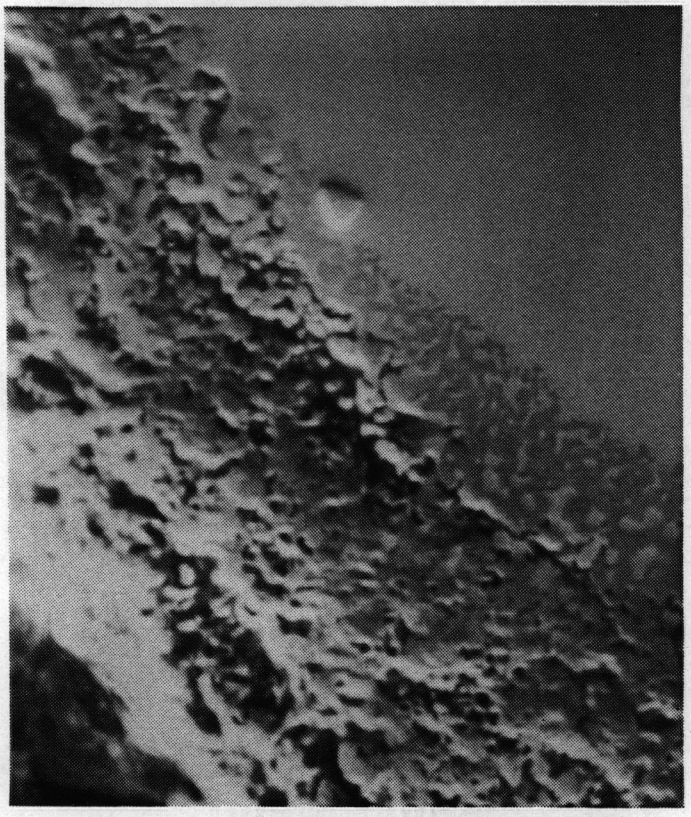

Figure 4-45. Test 3, Specimen Image, 1000X.

Figure 4-46. Test 3, Sulfur Map, 1000X.

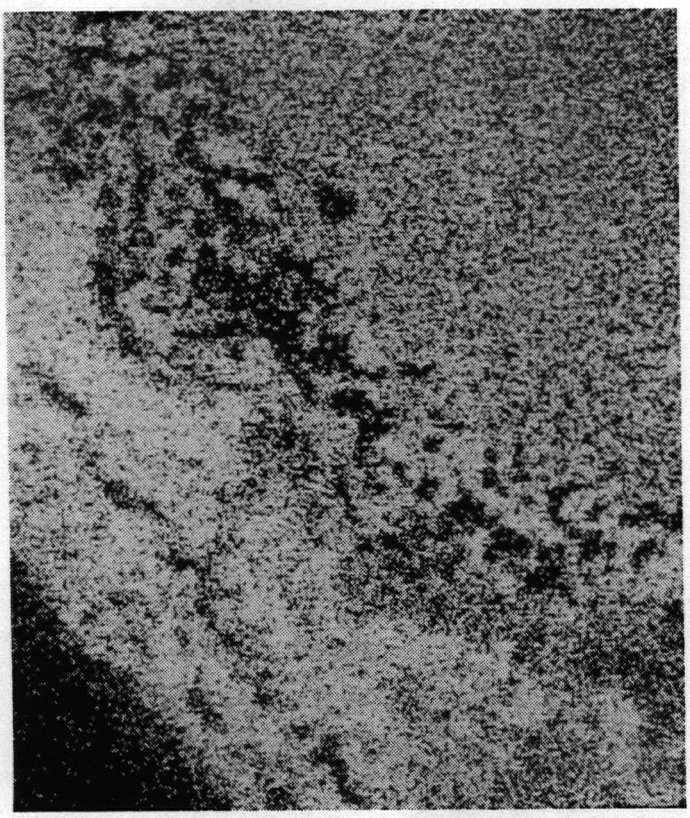

Figure 4-47. Test 3, Cr Map, 1000X.

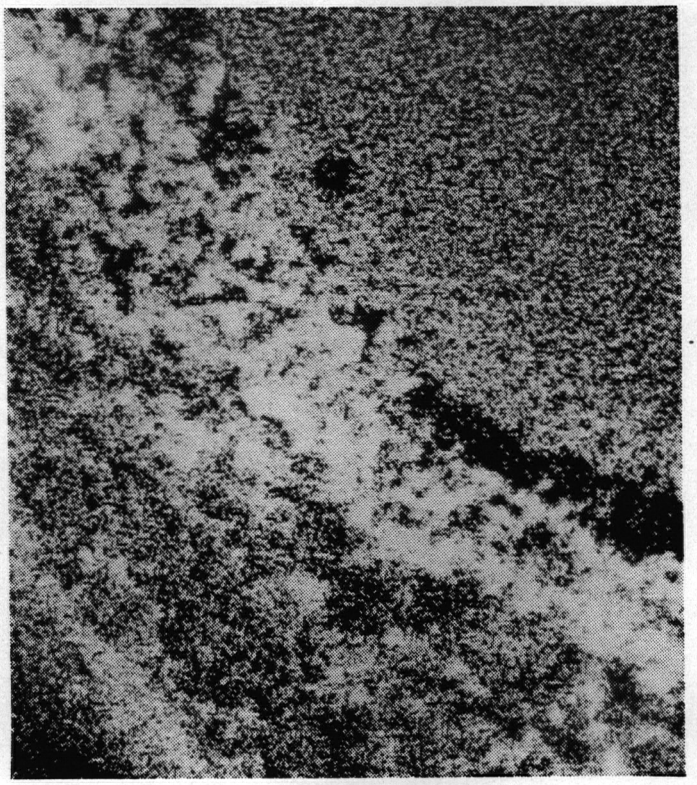

Figure 4-48. Test 3, Al Map, 1000X.

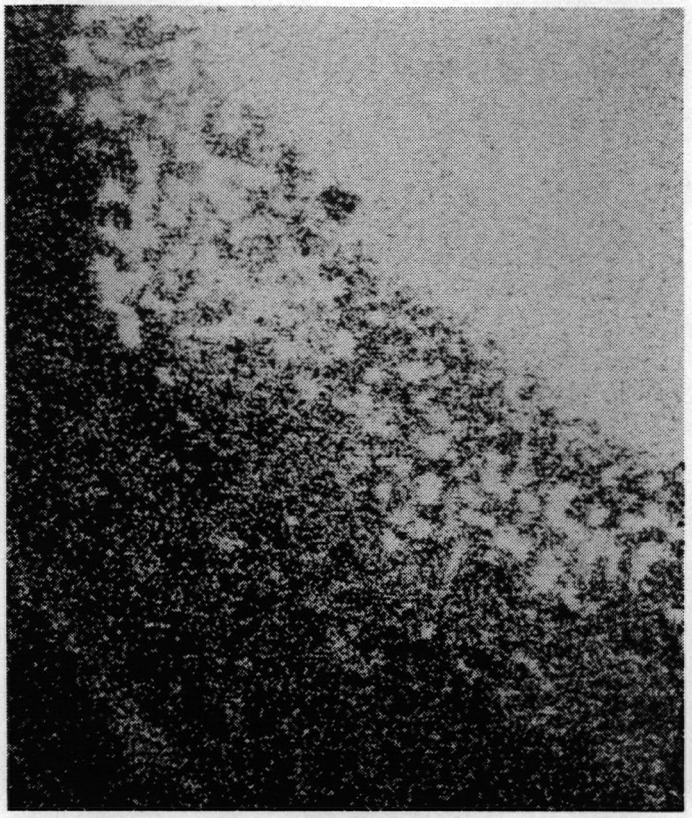

Figure 4-49. Test 3, Ni Map, 1000X.

Test 4 was run with the highest SO_x concentration and both Na and K as fuel contaminants. The current image of a portion of the scale from the low temperature 1300 °F pin is shown in Figure 4-50. It was unique among the probe samples investigated in that considerable K was present. Usually the sulfates of the fuel contaminants are lost in metallographic preparation but in this instance most of the salt/scale material was retained. Figures 4-51 and 4-52 show the S and K maps, respectively. It is clear that most of this material is K_2SO_4. The Ni and Cr maps are shown in Figures 4-53 and 4-54. To see how the K and other material were distributed, a portion of the deposit shown in Figure 4-50 was analyzed at a higher magnification. The current image of this is shown in Figure 4-55. The sulfur and K maps are shown in Figure 4-56 and 4-57. It is clear that these maps are nearly identical. The Ni map is shown in Figure 4-58. This map shows the reason this material was probably not lost during metallographic preparation, for surrounding the K_2SO_4 islands is a fairly continuous network of what is probably Ni oxide. Of course, there is some Ni present in the K_2SO_4 islands, so these are mixed sulfates. There was some Al present in this material as shown in Figure 4-59. It was associated primarily with the Ni oxide. Most of this material is probably precipitated from the salt melt.

The EDAX results show that the LTMT and ACSBR specimens are quite similar. In both instances the low temperature scales contain sulfides along the scale side of the scale-metal matrix interface. In some instances, precipitated oxides from the salt melt appeared as in Test 4 of the ACSBR tests, where a porous Ni oxide scale filled with K sulfate was found. This was not notable for IN-738 in the LTMT specimens, but it was for the cobalt base alloy FSX-414 as shown in Figure 2-11.

4.6 DEPOSIT CHEMISTRY

After each of the runs in the ACSBR (See Tables 4-1 and 4-2) the 0.25-inch tube specimens were removed from the burner rig and rinsed in 40 cc of deionized water, with the exception of the specimens from test 8. In the case of test 8, where the vanadium additive was used, some of the deposit material was water insoluble. In this case the specimens were scraped to remove deposit and then the pins were rinsed in deionized water. The scrapings were treated with acid (50% HCl). The main objectives of the deposit collection were to obtain the water soluble species, which are the sulfates of Na, K, Co, and Ni. The concentrations of these salts can tell much about the corrosion processes occurring.

Tables 4-3, 4-4 and 4-5 give the results of the chemical analyses for the ACSBR tests. Because it was impossible to remove specimens from the rig without losing deposit material, the results must be viewed with this in mind. Concerning Table 4-3, one of the first things to be noticed is the increase in alkali metals with a decrease in temperature below 1600 °F. A maximum concentration appears about 1400 °F + 100 °F. After that there is a steady decline in concentrations with decreasing temperature. It could be this deposition profile has to do with rig geometry, as in all tests for the sake of consistency the specimen temperature was highest in the front of the rig and decreased incrementally towards the rear of the rig. It could also be related to the temperature gradient between specimen and combustion gases. This gradient is believed to enhance the deposition rate of submicron particles and condensing vapor species. The explanation of why the deposition amount decreases after about 1400 °F is not clear. Perhaps at temperatures more than a few hundred degrees below the bulk gas temperature (1600 °F), deposit adherence begins to decrease, and the deposit does not grow as much as expected.

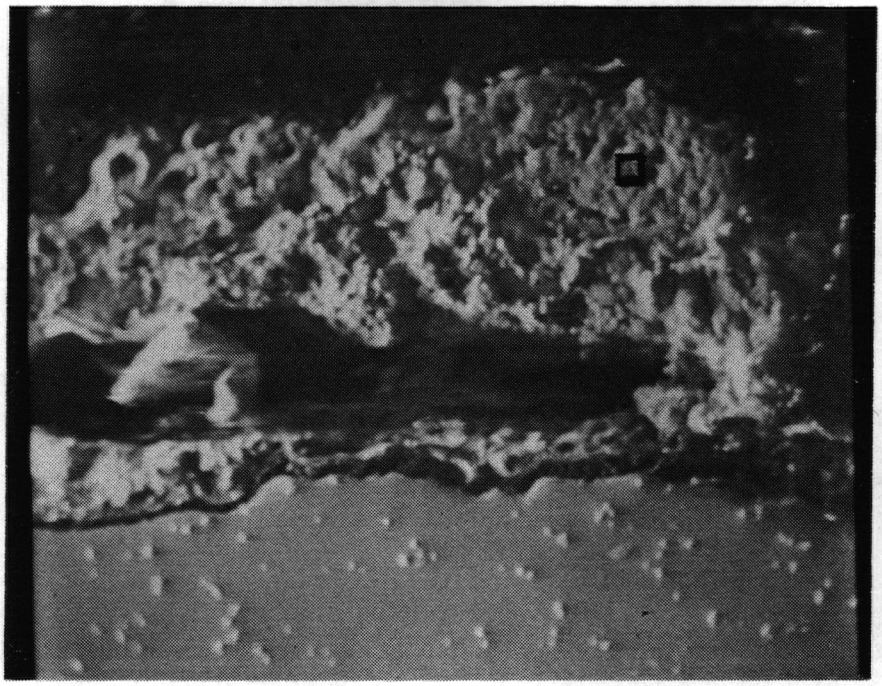

Figure 4-50. Test 4, Specimen Image, 100X.

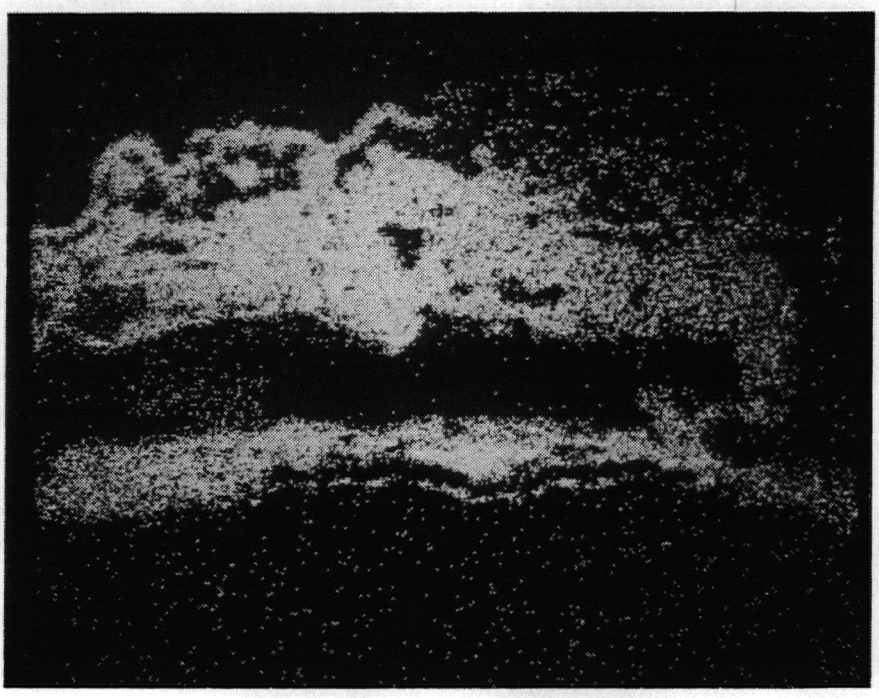

Figure 4-51. Test 4, Sulfur Map, 100X.

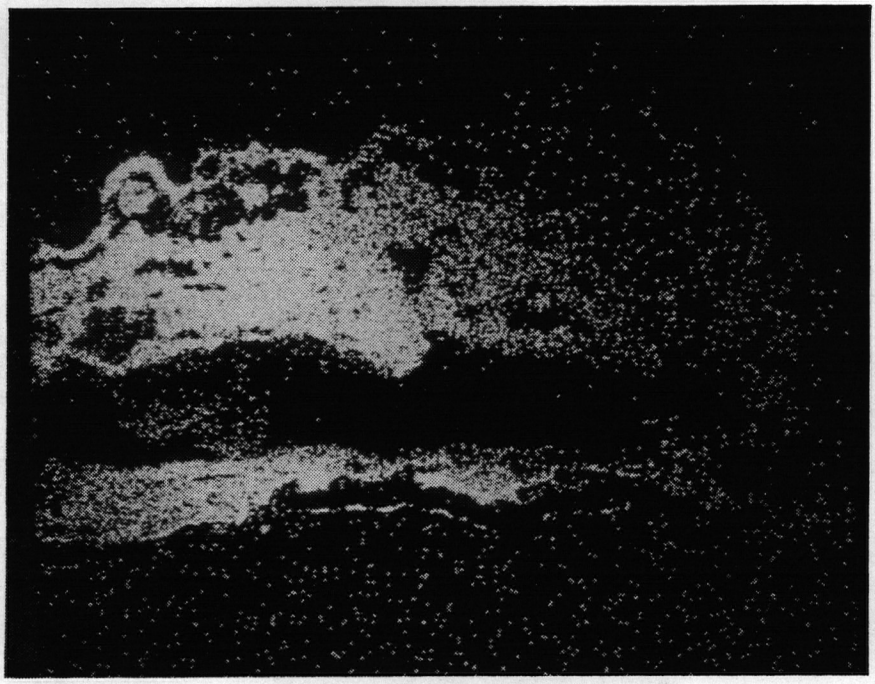

Figure 4-52. Test 4, K Map, 100X.

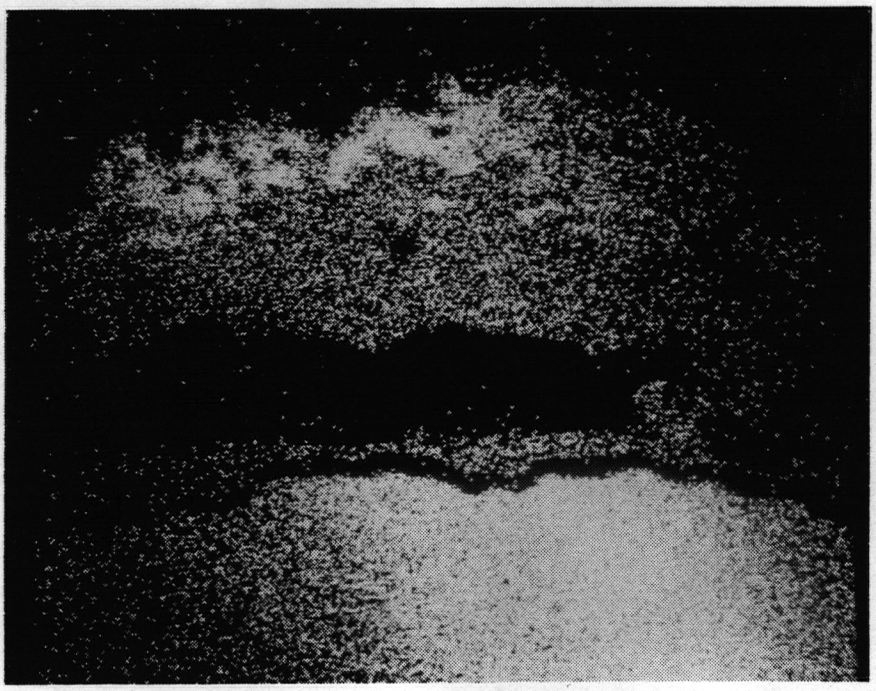

Figure 4-53. Test 4, Ni Map, 100X.

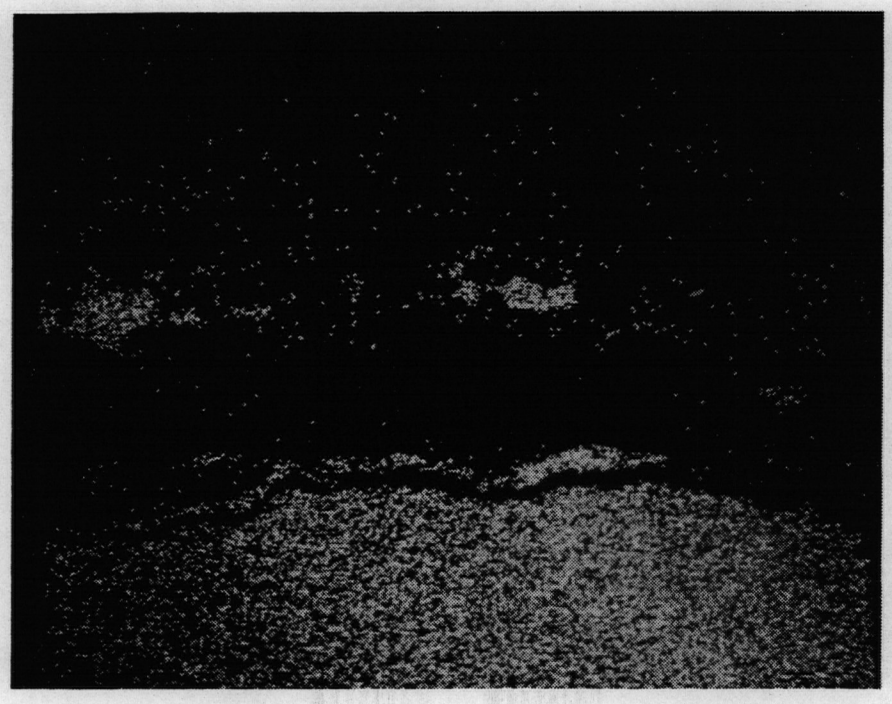

Figure 4-54. Test 4, Cr Map, 100X.

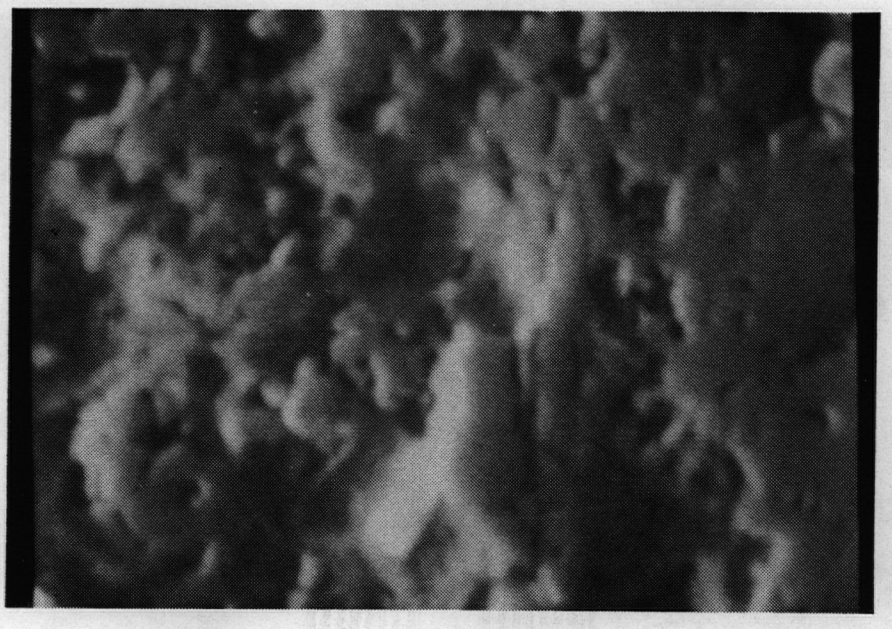

Figure 4-55. Test 4, Specimen Image, 2000X.

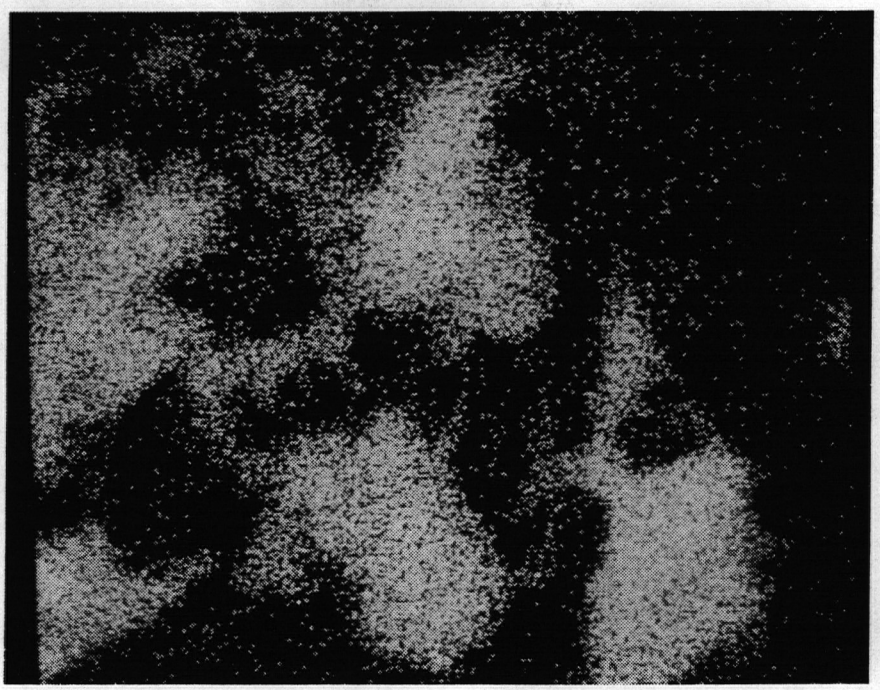

Figure 4-56. Test 4, Sulfur Map, 2000X.

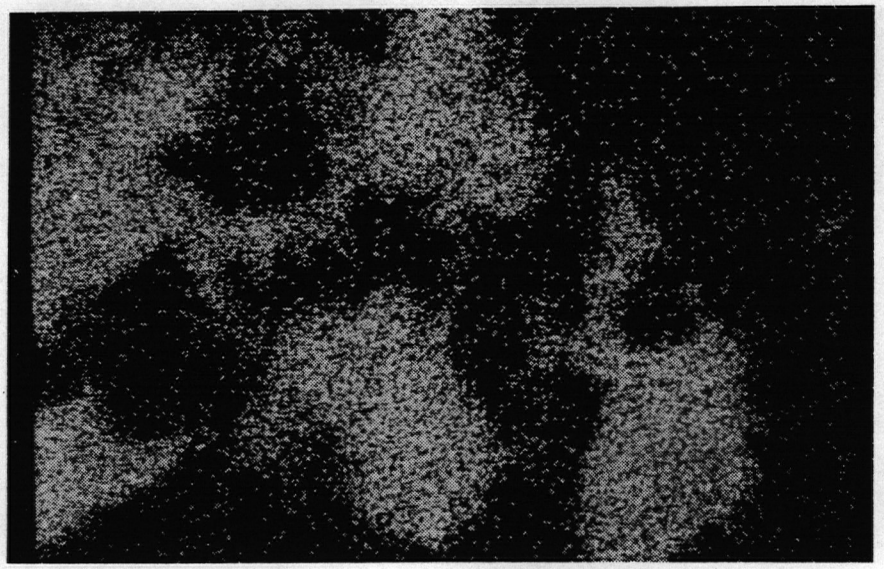

Figure 4-57. Test 4, K Map, 2000X.

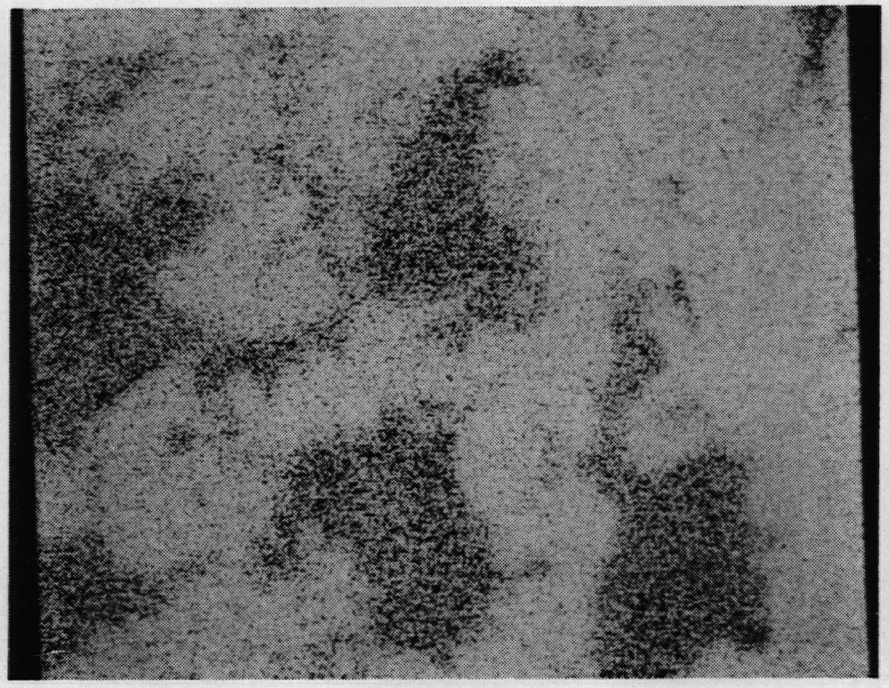

Figure 4-58. Test 4, Ni Map, 2000X.

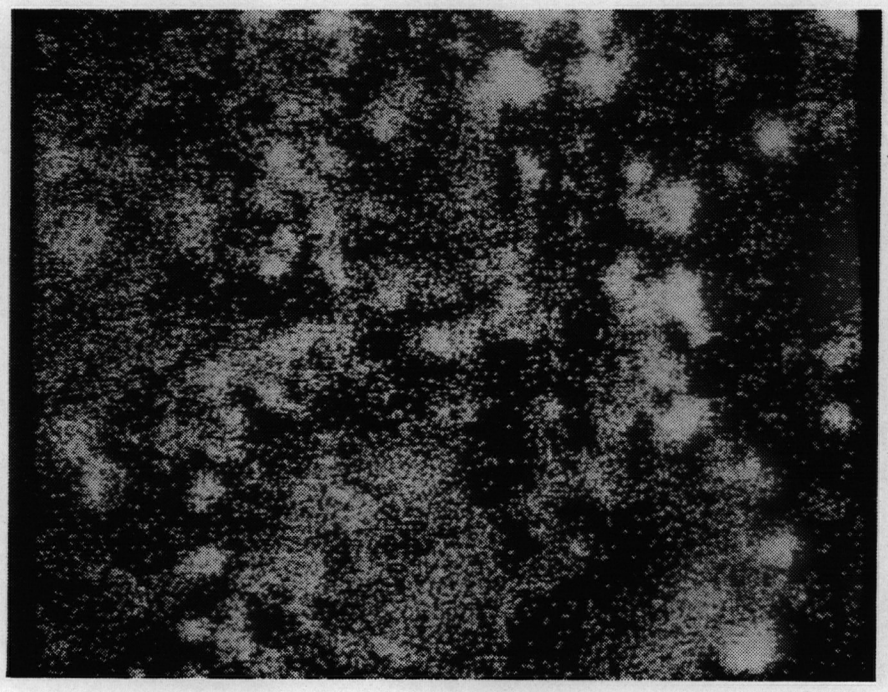

Figure 4-59. Test 4, Al Map, 2000X.

Table 4-3

CONCENTRATIONS (ppm) IN 40 cc DEPOSIT WASHING

	1	2	3	4		5		6		7		8			9		
	Na	Na	Na	Na	K	Na	K	Na	K	Na	Mg	Na	Mg	V	Na	K	Mg
1600	210	1500	420	370	195	460	230	360	150	250	190	104	107	1.0	37	29	45
1550			740														
1500	1000	2100	1100	550	420	1000	790	950	540	200	210	118	118	0.43	180	280	470
1450			210														
1400	1250	1200	130	850	770	1500	1500	1200	1000	450	440	280	377	1.7	440	330	760
1350			200														
1300	275	610		670	810	1200	1500	1050	1200	350	510	350	538	9.7	180	220	660
1250																	
1200	625	490		500	660	550	750	740	900	230	510	168	154	0.52	140	160	520
1150																	
1100	700	390		380	480	450	580	460	630	200	560	116	155	2.3	93	99	460

Table 4-4

ALLOY SULFATE CONCENTRATIONS (ppm) IN 40 cc DEPOSIT WASHING

	1		2		3		4		5		6		7		8		9	
	Ni	Co	Ni	Co	Ni	Co	Ni	Co	Ni	Co	Ni	Co	Ni	Co	Ni	Co	Ni	Co
1600	3.5	1.4	0.4	0.2	5.6	3.3	0.5	0.3	0.4	0.1	<0.1	<0.1	3.4	2.5	1.6	0.8	0.34	<0.1
1550					5.7	3.8												
1500	18.5	8.0	0.3	0.3	42	28	8.6	13	1.0	1.7	0.15	0.2	7.2	3.3	5.1	2.0	6.1	1.3
1450					36	28												
1400	25	11.5	12	3	65	20	25	49	5.2	10	<0.1	<0.1	25	15	17.0	13.4	<0.1	<0.1
1350					97	29												
1300	170	47.5	52	12			130	95	38	47	<0.1	<0.1	87	29	37.7	9.2	48	7.2
1250																		
1200	375	77.5	50	9			150	56	71	32	<0.1	<0.1	33	4.3	37.8	6.4	27	0.94
1150																		
1100	325	52.5	56	11			160	35	74	24	2.3	0.1	25	2.7	17.6	3.0	50	0.66

Table 4-5

DEPOSIT CHEMISTRY, TEST 8

Element	%					
	1600	1500	1400	1300	1200	1100
Ni	7.8	5.1	6.9	2.0	0.78	0.05
V	5.4	2.3	2.4	1.2	0.48	1.9
Na	4.5	3.5	5.3	6.7	5.6	4.3
Co	0.55	0.54	0.73	0.23	0.03	0.01
Mg	14.	3.9	12.	14.	13.	13.
Mg/Na/V	2.6/.83/1	1.7/1.5/1	5/2.2/1	11.7/5.6/1	27/11.7/1	6.8/2.2/1
Ni/Co	14.2	9.4	9.4	8.7	26.0	5.0

Notes: Fuel Ratio Mg/Na/V = 6.7/1.9/1.1
The electron microprobe was used to record x-ray energy spectra of the deposits. All but the 1500 °F specimen are highest in S with lesser amounts of Mg, Na, and V. The 1500 °F specimen is mostly black magnetic flakes that appear to be a stainless steel corrosion product but also contain S, V, Mg and Na.

Concerning Table 4-3, it is interesting to note that in the additive tests (tests 7, 8 and 9) the amount of alkali is less than appeared in the alkali only tests (tests 1 to 6). This is surprising since the alkali levels and the duration of test were about the same for all the tests. For the lower temperatures (1400 °F and below), in the additive tests the deposits were quite noticeable. These deposits would have an insulating effect and reduce the temperature gradient between the combustion gases and the deposit, so any enhancement due to undercooling would be reduced. Whether this effect is causing the reduction in alkali levels for the additive test specimens is not known, but it must be considered.

Also, in Table 4-3, it is clear that the K/Na ratio is far below the fuel value until temperatures of 1300 °F and below are reached. This is true in every instance in tests 4, 5, 6 and 9. The fuel values were K/Na = 1.1-1.2 and Mg/Na = 5.5 (test 9) and Mg/Na = 3.4-3.6 (tests 7 and 8) (See Table 4-1). This is expected because of the higher vapor pressure of K_2SO_4 compared to Na_2SO_4. Only at temperatures below about 1300 °F are vapor pressures small enough to make the deposit ratio close to the fuel ratio.

With regard to the Mg/Na ratio in the additive tests, the deposits should be Mg-rich at the higher temperatures. Thus, the fuel ratio would be approached at the lower temperatures. This expectation is because Na_2SO_4 has a higher vapor pressure than $MgSO_4$. However, as the data from tests 7, 8 and 9 show the Mg/Na ratio is below the fuel value at all temperatures, but approaches it at the lowest temperatures. There is no clear explanation for this. Perhaps the adherence of the Mg compounds being deposited is not high. There is some evidence from other work that Mg is first deposited as the oxide and then converted to the sulfate.

Table 4-4 gives results of the analyses for Ni and Co, the alloy sulfates in the deposits. The first thing to notice about these analyses is the increase of water soluble Ni and Co with a decrease in temperature. This agrees with the theory. Concentrations of alloy

sulfates relative to alkali sulfates are expected to be small down to about 1500 °F. Below this alloy sulfate stability increases rapidly (see Figure 4-8). Another trend to notice is Ni and Co concentrations are strongly affected by the SO_x concentration in the combustion gases. For example, in Test 6 where kerosene was the fuel and the SO_x pressure was $4.1x10^{-6}$ atm (SO_x counted as SO_2), almost no alloy sulfates were formed. This agrees with Figure 4-8 which shows no $CoSO_4$ formation below about $P_{SO_3} = 1x10^{-6}$ atm. Furthermore, the amounts of alloy sulfates at each temperature decrease with SO_x concentration in each analysis in tests 4, 5 and 6 and also in tests 1 and 3 versus 2. (For example at 1300 °F, the Ni values are 130, 38, 0.1 and the Co values are 95, 47, 0.1 as the SO_2 levels were $1.4x10^{-4}$, $2.2x10^{-5}$ and $4.1x10^{-6}$, respectively.)

Also, concerning Table 4-4 the ratio Ni/Co is 7.1 for the alloy IN-738. As $CoSO_4$ is the more stable sulfate, one would expect this ratio to be lower in the analyses of the water rinsings, and this is what is observed. It is interesting to note the concentration of Co actually was higher than the value of Ni in several instances around 1400 °F in tests 4 and 5. Perhaps this is the result of the stabilizing effect of K on Co sulfate.

Acid dissolution results of deposit material from test 8, given in Table 4-5, show the deposits consisting primarily of Mg compounds. The 1500 °F specimen had Fe contamination from attached stainless tubing. The Mg is primarily $MgSO_4$, but Mg, Ni and Na vanadates are probably present. The high Ni in the higher temperature specimens is a result of the presence of corrosion scale. Thus, the Ni/Co ratios are higher than those for the water washings. Also, in Table 4-5 is the ratio Mg/Na/V. Again, the Mg is low relative to the ratio set in the fuel in the higher temperature specimens. Sample size and inhomogenity is thought to be part of the reason for the low value of V in the 1200 °F specimen. There was some V present in the water washings as shown in Table 4-3, but the amount was small. It was felt that these levels represented the limited solubility of Mg vanadates.

As is shown in Figure 3-8 for Co sulfate and discussed earlier, it is the formation of Ni and Co sulfates in combination with alkali sulfates which reduce the salt melting point to the range 1400 °F to 1100 °F and result in low-temperature hot corrosion. Thus, the amount of alloy sulfates present in a salt melt is an indication of low-temperature, hot-corrosion activity. Table 4-6 gives the mole percent alloy sulfates. It will be noted how the reduction in S level reduces the amount of alloy sulfate. Raising specimen temperature has the same effect. Although these numbers can not be compared directly with the data in Figure 3-1 (Figure 3-1 refers to pure cobalt whereas the ACSBR work was done on the superalloy, IN-738) it is clear that the phenomena is the same. In Figure 4-60 the mole percent alloy sulfates is plotted versus specimen temperature for tests 1 through 6. As Figure 4-60 shows the alloy sulfates concentration reaches a maximum near 1100 °F to 1200 °F, yet corrosion is decreasing in this range. The reason for this is the kinetics of corrosion attack are greatly reduced at the lower temperatures. Also, some deposits may be so high in alloy sulfates that the salt melt would be solid at the temperatures involved.

In Table 4-6 the mole percent alloy sulfates in the additive tests (7 through 9) were calculated on the same basis as used for tests 1 through 6 for purposes of comparison. Actually the mole percent alloy sulfates are much less in the additive case because of the presence of considerable $MgSO_4$. This may be part of the reason for the reduction in corrosion in these tests, but it does not explain the reduction in corrosion observed at 1600 °F and 1500 °F.

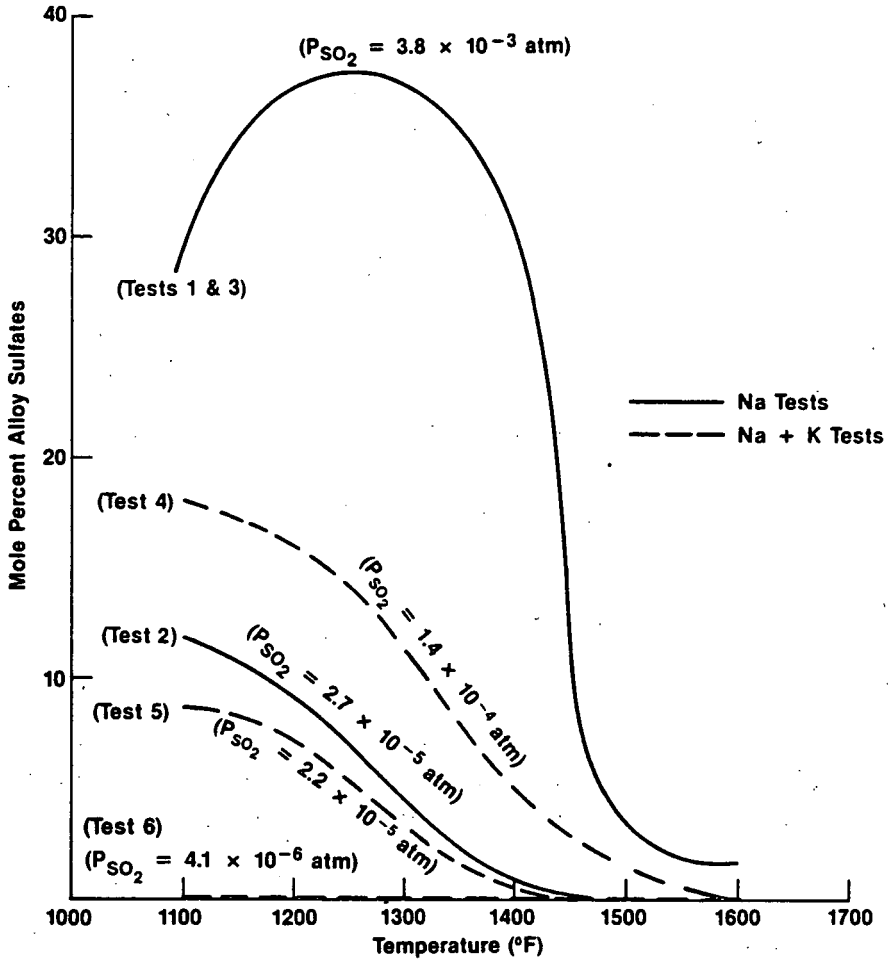

Figure 4-60. Mole Percent Alloy Sulfates versus Temperature.

Table 4-6

ACSBR TEST DEPOSIT CHEMISTRY

Temperature		Mole % Alloy Sulfate							
Test	1	2	3	4	5	6	7	8	9
Principal Fuel Contaminants	Na	Na	Na	Na + K	Na + K	Na + K	Na + Mg	Na + Mg + V	Na + K + Mg
pSO_2 (atm) $\times 10^4$	38.0	0.27	38.0	1.4	0.22	0.041	38.0	38.0	38.0
1600° F	1.8	0.03	1.6	0.13	0.07	<0.02	1.8	1.7	0.5
1550° F			1.0						
1500° F	2.0	0.02	4.7	2.1	0.14	<0.02	3.9	4.5	1.7
1450° F			19.3						
1400° F	2.2	1.0	33.8	4.3	0.50	<0.02	6.5	7.8	0.0
1350° F			33.0						
1300° F	38.1	7.6		13.3	3.1	<0.02	20.5	9.5	12.2
1250° F									
1200° F	36.1	8.6		15.4	7.5	<0.02	11.2	17.1	8.5
1150° F									
1100° F	29.1	11.8		18.7	8.8	<0.02	9.7	12.2	20.8

Note: Mole % alloy sulfate measured as (Ni + Co/ Ni + Co + Na_2 +K_2).

Table 4-7 shows the results of the pH determinations of the water washings. It was observed that in all tests except where the sulfur level was reduced (tests 2 and 6) the pH decreased with decreasing specimen temperature. The acidity appears to occur in the same temperature range (1400 °F to 1100 °F) as low-temperature hot corrosion. The acidity is thought to be related to the concentration of the pyrosulfate ion, which is a function of the SO_3 partial pressure. When the deposit is water washed, the pyrosulfate goes to sulfuric acid.

The 1400 °F to 1100 °F deposits from test 6 were unique in that they were bright orange. All deposits from this test contained Cr (The water soluble levels ranged from 27 to 96 ppm.) Apparently, in the low-temperature deposits an alkali chromate had formed.

The deposit chemistries of high- and low-temperature hot corrosion have their own characteristics, just as do the microstructures. It has been seen that to have low-temperature hot corrosion, an alloy sulfate will form and this will readily show up in the deposit chemistry. The deposit chemistries were sensitive to changes in SO_x pressure and temperature, with reductions in alloy sulfate concentrations accompanying a reduction in SO_x and/or increases in temperature. Deposit washing pH was also sensitive to SO_x pressure and temperature following the same trends as mentioned for alloy sulfate concentration. The presence of the Mg additive reduced alloy sulfates for reasons which are not clear and significantly reduced the rate of low temperature hot corrosion.

Table 4-7

pH of Deposit Washings

Temperature	Deposit Washing pH								
Test No.	1	2	3	4	5	6	7	8	9
pSO_2 (atm) $\times 10^4$	38.0	0.27	38.0	1.4	0.22	0.041	38.0	38.0	38.0
1600° F	6.3	7.1	5.9	6.9	6.7	7.4	6.7	6.7	6.7
1550° F			7.4						
1500° F	6.2	6.9	6.2	5.4	6.3	7.5	3.7	4.4	3.8
1450° F			3.2						
1400° F	5.7	6.3	3.2	3.8	4.2	8.4	3.2	6.5	8.9
1350° F			3.6						
1300° F	4.6	4.9		3.3	3.8	8.0	2.8	2.7	3.8
1250° F									
1200° F	4.3	5.1		3.4	4.0	7.9	3.1	4.2	3.0
1150° F									
1100° F	3.9	5.2		3.4	3.8	7.3	3.1	3.5	2.6

Note: All deposit washings used 40 cc of distilled water.

5. CONCLUSIONS

This study of low-temperature hot corrosion grew out of observations made during the Long-Term Materials Test (LTMT) where gases from a pressurized fluidized bed were run through a test section resulting in 1300 °F and lower temperature corrosion equal to what was seen at 1500 °F. Also the corrosion resistant cobalt base alloy such as FSX-414 (29 Cr) was attacked just as much as the nickel base alloy IN-738 (16 Cr). A significant difference between this environment and typical hot corrosion environments is the presence of potassium.

Potassium will be a contaminant in fluidized bed coal combustion environments, which according to the results of this study will increase the rate of hot corrosion and range over which it occurs in comparison to the more familiar hot corrosion environment produced by sodium as a fuel contaminant. In particular, the range of sulfur concentrations over which low-temperature hot corrosion (1100 °F-1400 °F) can occur is increased by an order of magnitude in sulfur oxide partial pressure.

Theoretical thermochemical calculations were able to determine the range of stability in the Na-K-Co sulfate ternary. In particular, the temperature and SO_x range over which a liquid salt was stable was predicted. These calculations showed the stabilizing effect of K on $CoSO_4$. They also showed the importance of sulfur levels and relative amounts of Na and K in determining the absence or presence of low-temperature hot corrosion. The thermochemical model developed allows one to predict conditions under which low-temperature hot corrosion will occur.

A small burner rig was modified to accept air-cooled specimens used in the LTMT. The test results from the rig confirmed the thermochemical calculations. Also, the corrosion morphologies produced as a function of temperature and sulfur level were similar to those found in the LTMT. Furthermore, the air-cooled specimens showed the same increase in alkali sulfates as was seen in the LTMT specimens when the metal temperature was decreased below the gas temperature. This is thought to be a result of the gas cooling in the neighborhood of the air-cooled specimen resulting in an increased flux of small particles and vaporized condensible species as the alkalies are thought to be.

Other important contaminants in fluidized bed combustors are Mg and Ca, and in the case of the Mg additive, burner rig results show it to be effective in reducing low- temperature hot corrosion. Reductions of at least 50% in the corrosion rate for 200-h tests at all temperatures (1100 F-1600 F) were observed in all additive tests with Mg, even in the presence of both Na and K, and with the highest sulfur levels used in all the testing, $P_{SO_2} = 38 \times 10^{-4}$ atm.

This project sought to understand the effect of potassium in low-temperature hot corrosion. The project has been successful in defining what this effect is. Corrosion problems have a severe impact on the performance, reliability, and economics of power generation equipment. In particular, hot corrosion in combustion gas turbines is among the most important problems faced by this equipment, requiring considerable expenditures in the development of corrosion resistant alloys and coatings, and requiring the implementation of restrictive fuel specifications.

The results of this research clearly re-confirm those of the Long-Term Materials Test (DOE, Morgantown) regarding the degradation of critical gas turbine superalloys exposed to the effluent of a pressurized fluidized bed combustor. This has long-term implications for the performance and reliability of gas turbine equipment in advanced coal-fired system environments. Continuing research into the mechanisms of alloy corrosion and protective systems to extend material performance and component life appears necessary to insure gas turbines of cost-effective performance.

This research, designed to understand and reduce corrosion by gaining a thermo-chemical knowledge of the phenomena has shown its success and is a necessary step in the management of power generation equipment.

APPENDIX A

ANALYSIS OF PHASE DIAGRAMS

ANALYSIS OF THE K_2SO_4-$CoSO_4$ BINARY PHASE DIAGRAM

The K_2SO_4-$CoSO_4$ phase diagram is shown in Figure A-1 [8]. Unlike the Na_2SO_4-$CoSO_4$ system (Figure A-2), there is no observed solid solubility of $CoSO_4$ in K_2SO_4. An attempt to fit the liquidus line at the K_2SO_4 end with a regular solution model was unsuccessful. However, the liquidus line could be fitted nicely with a sub-regular model [15]. According to this model, the total heat of mixing (ΔH^m) and partial molar heats of mixing $\overline{H}_i^m$ can be expressed as a function of mole fractions (X_i) as follows:

$$\Delta H^m = (A_1 X_1 + A_2 X_2) X_1 X_2 = [A_1 + (A_2 - A_1) X_2] X_1 X_2 \quad (1)$$

$$\overline{H}_1^m = [(2A_1 - A_2) + (2A_2 - 2A_1) X_2] X_2^2 \quad (2)$$

$$\overline{H}_2^m = [(2A_2 - A_1) + (2A_1 - 2A_2) X_1] X_1^2 \quad (3)$$

Since the entropies of mixing of a "sub-regular" solution are the same as those for an ideal solution, the heats of mixing are the same as the excess free energies of mixing.

At any temperature T, the activity of a component can be related to its partial heat of mixing by

$$RT \ln a_i = \overline{H}_i^m - T \overline{S}_i^m \quad (4)$$

Various formulations have been suggested for the partial entropy of mixing ($\overline{S}_i^m$) of an ideal solution [16-18]. In an earlier paper [4], an approach suggested by Forland was used [16]. According to this model, the cation sites would be occupied by either two K^+ ions or a Co^{++} ion and a vacancy. This results in entropy relations that are similar to those for two components where there is no dissociation. Here this is called the molecular approximation of entropy.

$$\overline{S}_{CoSO_4} = R \ln X_{CoSO_4} \; ; \; \overline{S}_{K_2SO_4} = R \ln X_{K_2SO_4} \quad (5)$$

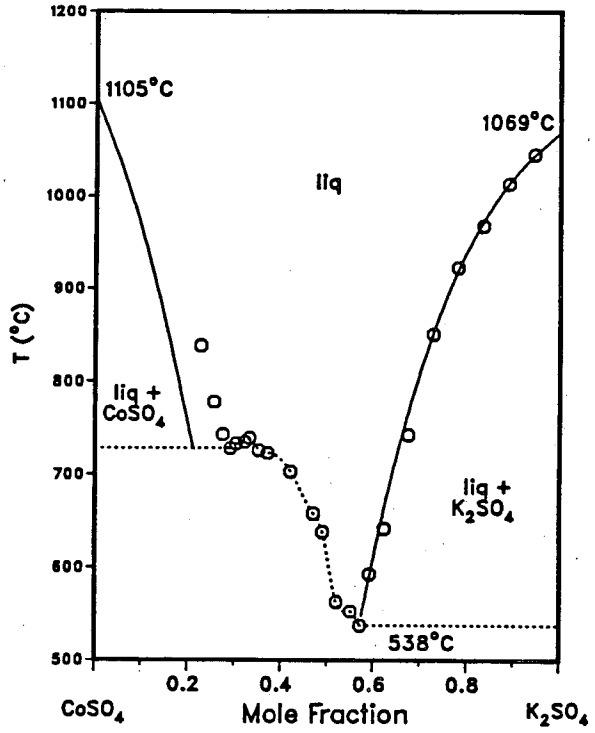

Figure A-1. **K_2SO_4-$CoSO_4$ binary phase diagram. Open circles are data points of Calcagni and Marotta [8], and dotted lines are as drawn by them. Solid lines were calculated as described in the text. Complex K_2SO_4-$CoSO_4$ solid double salts which were not analyzed occur in the center of the diagram.**

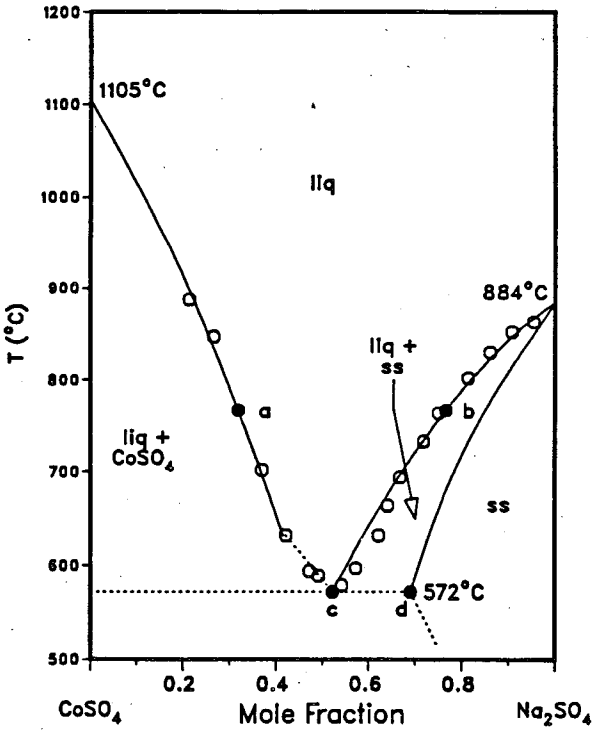

Figure A-2 **Na_2SO_4-$CoSO_4$ binary phase diagram. Open and closed circles are data points of Calcagni and Marotta [8], and dotted lines as drawn by them. Data points marked "a", "b", "c", and "d" were fit exactly to extract parameters from which the solid lines were calculated as described in the text. Complex Na_2SO_4-$CoSO_4$ solid double salts which we cannot analyze occur in the center of the diagram. This phase diagram is also given by Bol'shakov and Fedorov [21].**

Bale and Pelton [19] used the Temkin approach for evaluating the entropies of mixing of an ideal solution. In Temkin's model, the salts are considered to be completely ionized; the cations and anions are assumed to be randomly distributed over their respective positions. Then the entropy relations for K_2SO_4-$CoSO_4$ mixtures can be expressed as

$$\bar{S}_{CoSO_4} = -R \ln X^1_{Co^{2+}} ; \bar{S}_{K_2SO_4} = -2R \ln X^1_{K^+} \quad (6)$$

$$X^1_{Co^{2+}} = \frac{X_{CoSO_4}}{1+X_{K_2SO_4}} ; X^1_{K^+} = 1-X^1_{Co^{2+}} \quad (7)$$

As far as calculations of the activities of $CoSO_4$ are concerned (using the phase diagrams), both of these approaches give similar results, as is shown below. In this work the approach of Pelton, Bale, and Lin [20] for evaluating the ternary system was followed, and the entropy relations of the second approach were used for the ternary system calculations.

The partial molar entropy of mixing of K_2SO_4 ($\bar{S}^m_{K_2SO_4}$) in a liquid in equilibrium with solid K_2SO_4 can be obtained from equations 5 and 6 using the liquidus composition from the binary K_2SO_4-$CoSO_4$ phase diagram. The corresponding activity of K_2SO_4 liquid can be determined from the free energy change of the following reaction.

$$K_2SO_4\ (s) = K_2SO_4\ (l) \quad (8)$$

Thus, the partial molar enthalpy of mixing of K_2SO_4 ($\bar{H}^m_{K_2SO_4}$) can be calculated as a function of temperature and composition from equation 4.

If the K_2SO_4-$CoSO_4$ system obeys the above sub-regular solution model, then a plot of $\bar{H}^m_{K_2SO_4}/X^2_{CoSO_4}$ as a function of X_{CoSO_4} should result in a straight line. Figure A-3 shows a straight line fits to both of the above approximations for entropy. The differences between the two approximations are very small and the fits are reasonably good between 0.1 and 0.4 mole fraction $CoSO_4$. The data obtained using the Temkin's approximation of entropy in Figure A-3 fit the following relationship

$$\bar{H}^m_{K_2SO_4} = (-1326 - 29941\ X_{CoSO_4}) X^2_{CoSO_4} \quad (9)$$

The resulting relationships for the partial heat of mixing of $CoSO_4$ and the total heat of mixing are

$$\bar{H}^m_{CoSO_4} = (-46237 + 29941\ X_{K_2SO_4}) X^2_{K_2SO_4} \quad (10)$$

$$\Delta H^m = (-16296\ X_{K_2SO_4} - 31267\ X_{CoSO_4}) X_{K_2SO_4} X_{CoSO_4} \quad (11)$$

Using equation 10 and the partial entropy of mixing of $CoSO_4$ from equation 6, the activity of $CoSO_4$ can be obtained from equation 4. Similar calculations can be performed for entropies estimated using the molecular model. The difference in activities calculated using the two approximations was very small, on the order of those shown in Figure A-3 for heat terms. For all subsequent calculations Temkin's approximation was used.

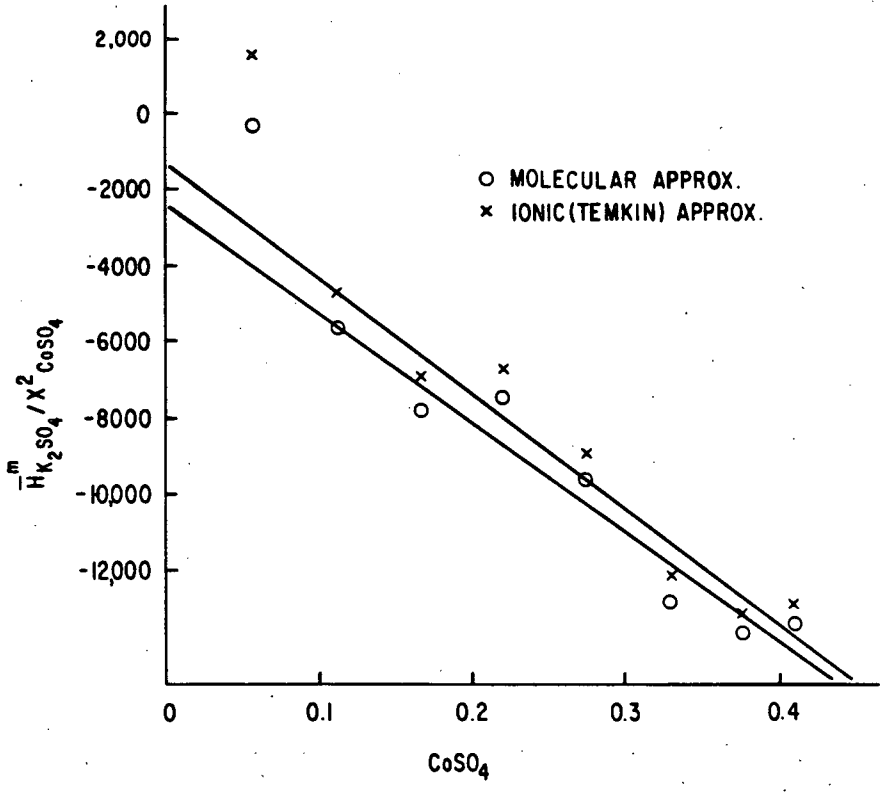

Figure A-3. **Test plots of a quantity related to the partial molar heat of mixing of K_2SO_4 as a function of the mole fraction of $CoSO_4$ along the liquidus line in the K_2SO_4-$CoSO_4$ system using two separate approximations for the entropy of mixing. A straight line through the data points indicates that the solution obeys a sub-regular solution (see equation 2).**

ANALYSIS OF Na_2SO_4-$CoSO_4$ BINARY PHASE DIAGRAM

This binary system has been described both by Calcagni and Marotta [8] and by Bol'shakov and Fedorov [21]. Only the former give numerical data, and so their diagram was used, which is shown in Figure A-2. The data was adjusted in one minor way. Calcagni and Marotta give the melting point of pure Na_2SO_4 as 887 °C rather than the currently accepted value of 884 °C [14,19]. Therefore, 3 °C was subtracted from all the temperatures they give in this system. Thus, for example, in Figure A-2 the eutectic temperature is 572 °C rather than the 575 °C Calcagni and Marotta report.

As in an earlier analysis of this binary system by Luthra and Shores [4], the excess free energies of mixing in both the liquid and the solid solution can be described by a regular solution model. But a different approach is used here to derive these quantities. Luthra and Shores used only the phase diagram information. In this instance the phase diagram is used, but in addition one other piece of experimental evidence, a datum taken from their paper is used. The new procedure lets one determine, from the phase diagram, the free energy of melting of $CoSO_4$, the quantity that was estimated previously. For a regular solution, the heat quantities defined above can be expressed as

$$\Delta H^m = \Omega X_1 X_2 \tag{12a}$$

$$\bar{H}_1^m = \Omega X_2^2 \tag{12b}$$

$$\bar{H}_2^m = \Omega X_1^2 \tag{12c}$$

In this analysis the following quantities are determined: 1) the parameter Ω or liquid solution, 2) the free energy of melting of $CoSO_4$ solid, 3) the parameter Ω for the solid solution of Na_2SO_4 and $CoSO_4$, and 4) the free energy of transition of $CoSO_4$ solid dissolved in Na_2SO_4, with reference to pure $CoSO_4$ solid.

To determine the parameter Ω for the liquid solution, it is noted that the points "a" and "b" in Figure A-2 are both reported at the same temperature by Calcagni and Marotta 770 °C (which we call 767 °C). Point "a" is at equilibrium with $CoSO_4$ (s). The SO_3 partial pressure at this point is therefore equal to the SO_3 partial pressure at equilibrium at this temperature in the chemical reaction (1) (See Section 3), which is 2.4×10^{-3} atm. The SO_3 partial pressure at point "b" can be estimated to be about 5×10^{-5} atm from experimental results shown in Figure 13 of the paper by Luthra and Shores [4] for the presence or absence of melting a various SO_3 partial pressures at almost exactly this temperature. The ratio of these two SO_3 partial pressures is equal to the ratio of the $CoSO_4$ activities in the liquid phase at points "a" and "b".This ratio can be used to determine the parameter Ω . From equations (4) and (12b),

$$RT \ln (a^a_{CoSo_4} / a^b_{CoSO_4}) = \Omega [(X^a_{Na_2SO_4})^2 - (X^b_{Na_2SO_4})^2] - T [\bar{S}^{m,a}_{CoSO_4} - \bar{S}^{m,b}_{CoSO_4}] \tag{13}$$

Here, the partial molar entropies of mixing of $CoSO_4$ can be determined from the equation such as (6). Thus, the only unknown Ω can be determined. The calculated value of Ω is -10,628 cal/mol.

The free energy of fusion of $CoSO_4$ was estimated from the phase diagram by curve fitting the five left-most data points in Figure A-2. The free energy of fusion of $CoSO_4$ at each point can be calculated from the composition and from the regular solution excess heat of mixing parameter of the liquid, which was already determined as described above. The values fall almost exactly on a straight line when plotted against the temperature, showing that the free energy can be approximated in the simplest possible way, as $\Delta G = \Delta H - T \cdot \Delta S$, with only two parameters, a constant enthalpy of fusion, ΔH, and a constant entropy of fusion, ΔS. A straight line was drawn through them such that the free energy of fusion at point "a" was fitted exactly and the mean square deviation of the free energies of the other four points was minimized. This yielded a value of 9962 cal/mol for the enthalpy of fusion of $CoSO_4$ and a value of 7.229 cal/mol·K for the entropy of fusion. The ratio of these quantities is the melting point of $CoSO_4$, 1378 K ▫ 1105 °C.

The parameters determined so far enable construction of the left-most solid curve in Figure A-2, which is the equilibrium line between the liquid and $CoSO_4$ (s). A similar curve can also be calculated for K_2SO_4-$CoSO_4$ liquid mixtures using the same values for the enthalpy and entropy of fusion and melting point of $CoSO_4$. This is shown on the left side in Figure A-1. The fit there to the left-most three data points of Calcagni and Marotta is not particularly good.

To complete the analysis of the Na_2SO_4-$CoSO_4$ system, estimates of the Na_2SO_4 and $CoSO_4$ activities in the solid solution are needed. In the regular solution model the Na_2SO_4 activity in the solid solution depends upon only one additional parameter, the regular solution heat of mixing parameter in the solid solution. This parameter can be obtained from the data points "c" and "d" in Figure A-2, both at the eutectic temperature, 572 °C. The activity of Na_2SO_4 in the solid solution at "d" must equal that in the liquid at "c", which can be calculated from the temperature, the composition, and the regular solution heat of mixing parameter already determined in the liquid. Setting the activity of Na_2SO_4 in the solid solution at "d" equal to this determines the regular solution heat of mixing parameter in the solid solution to be -11,311 cal/mol.

Finally, one needs an approximation for the free energy of "pure" $CoSO_4$ in the solid solution, that is, in the mathematical limit where the mole fraction of $CoSO_4$ in the solid solution is extrapolated to unity and the free energy of mixing vanishes. Because the solid solution does not really extend all the way across the phase diagram to a $CoSO_4$ mole fraction of 1.0, there is no constraint to set this quantity equal to the free energy of $CoSO_4$ (s) itself (in which case, of course, it would be identically equal to zero by convention, since $CoSO_4$ (s) is the conventional standard state).

Assume, again, that this free energy can be approximated in the simplest possible way in terms of two parameters, a constant enthalpy and a constant entropy. These were chosen so as to fit the compositions of eutectic points "c" and "d" and also point "b" in Figure A-2 exactly. Point "d" is the only point on the solidus given by Calcagni and Marotta. The partial molar free energy of $CoSO_4$ in the liquid at "c" can be computed from the parameters so far determined. This equals the partial molar free energy of $CoSO_4$ in the solid solution at "d". From this one subtracts the ideal partial molar free energy of mixing of $CoSO_4$ in the solid solution at "d" and the regular solution excess free energy of mixing of

$CoSO_4$ in the solid solution at "d", both quantities calculated from the composition there, the temperature, and the regular solution excess heat of mixing parameter in the solid solution already determined. The difference is one value of the free energy of "pure" $CoSO_4$ in the solid solution at a temperature of 572 °C.

A similar calculation was then carried out using the point "b" in Figure A-2 as follows. There is no data point for the solidus composition at this temperature, but from the parameters already determined one can calculate the composition of the solidus at which the partial molar free energy of Na_2SO_4 in the solid solution is the same as in the liquid at "b". Then, again requiring also that the partial molar free energy of $CoSO_4$ in the solid solution at that composition be equal to the partial molar free energy of $CoSO_4$ in the liquid at "b" gives a second value for the free energy of "pure" $CoSO_4$ in the solid solution, this at a temperature of 767 °C.

Using just these two values of the free energy of "pure" $CoSO_4$ yields a value of the enthalpy of "pure" $CoSO_4$ of 10,404 cal/mol and a value of the entropy of "pure" $CoSO_4$ of 1.420 cal/mol °K. By using just these two values it is ensured that the points "b", "c", and "d" in the phase diagram will be fit exactly. These values may be thought of as the thermodynamic enthalpy and entropy changes that would, according to the model, occur in a hypothetical phase transition.

$$CoSO_4\ (s) = CoSO_4\ (\text{in } Na_2SO_4\text{-}CoSO_4\ ss)$$

in the limit that the mole fraction of $CoSO_4$ in the solid solution is extrapolated to unity. If the structure of the Na_2SO_4-$CoSO_4$ solid solution were exactly the same as that of pure solid $CoSO_4$, the free energy associated with this reaction should be zero.

The solid curves on the right side of Figure A-2 are the equilibrium liquidus and solidus lines calculated with the various parameters. The liquidus temperatures are also the values indicated on the right-hand side of the ternary diagram in Figure A-4. The $CoSO_4$ activities at these points were used to calculate the SO_3 partial pressures plotted on the right-hand side of the ternary triangle in Figure A-5.

Values of the various parameters obtained in the analysis of this binary diagram and the other two are listed in Tables A-1 and A-2. No strict physical significance is attached to these numerical values. Other sets of choices for these values give fits to the experimental data nearly as good as those shown in the several figures. Furthermore, small variations in the way any one datum is fit causes no great change in the overall quality of the results. For example, the choice of the value of the SO_3 partial pressure at point "b" in Figure A-2 merely serves to fix the scale for all subsequently calculated SO_3 partial pressures. If the P_{SO_3} value at point "b" in Figure A-3 is halved or doubled, then so are all others approximately, so that their relative values (when comparing one situation to another as in Figure 3-1) are virtually unchanged.

ANALYSIS OF K_2SO_4-Na_2SO_4 BINARY PHASE DIAGRAM

The K_2SO_4-Na_2SO_4 binary phase diagram [22] shown in Figure 3-6 has been analyzed by Bale and Pelton [19], who used the heat of mixing of a 50:50 Na_2SO_4-K_2SO_4 liquid solution given by Ostvold and Kleppa [23]. Their results and methods of analysis were adopted. In this system, the liquid freezes to form a K_2SO_4-Na_2SO_4 solid solution at all temperatures. The melting point of K_2SO_4 is 1069 °C and that of Na_2SO_4 is 884 °C, and in the binary mixture there is a melting point minimum at 832 °C at a K_2SO_4 mole fraction of

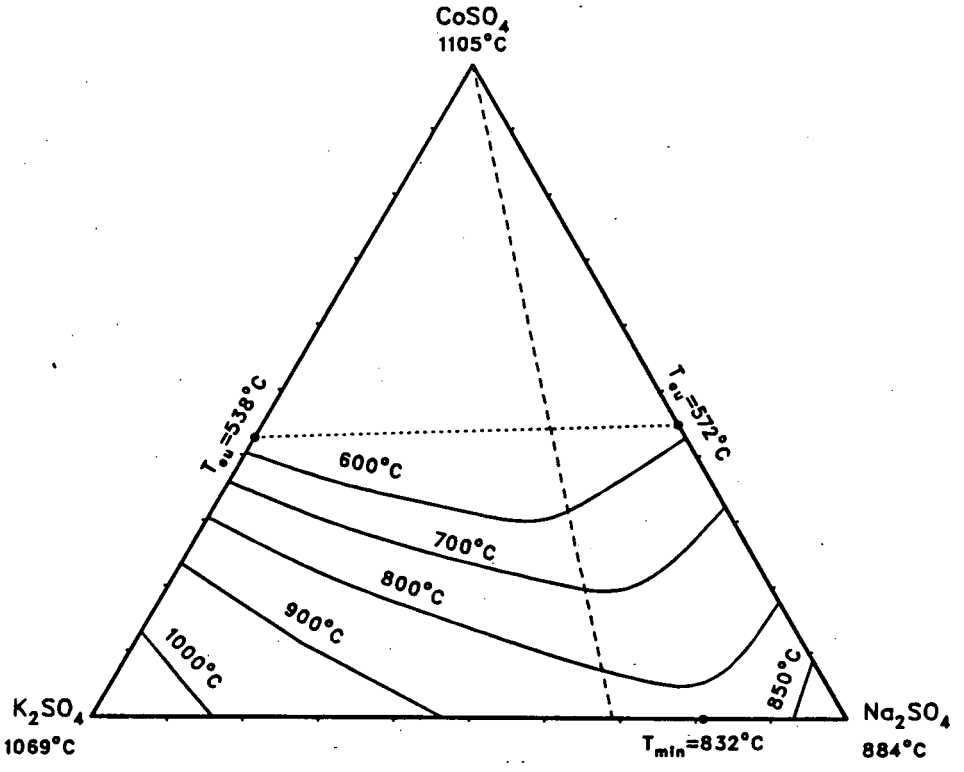

Figure A-4. **K_2SO_4-$CoSO_4$-Na_2SO_4 ternary phase diagram estimated from the three binary phase diagrams as described in the text. The solid lines display the liquidus compositions at the indicated freezing temperature of liquid mixtures in equilibrium with K_2SO_4-$CoSO_4Na_2SO_4$ solid solutions. Complex solid double and triple salts, which we cannot analyze, will occur in the center of the diagram. Calculated freezing points of liquid mixtures in equilibrium with $CoSO_4$ (s) near the top corner are very uncertain and are not shown. Temperatures along the dashed line are replotted in Figure 3-1 against the corresponding SO_3 partial pressures taken from the same line in Figure A-5.**

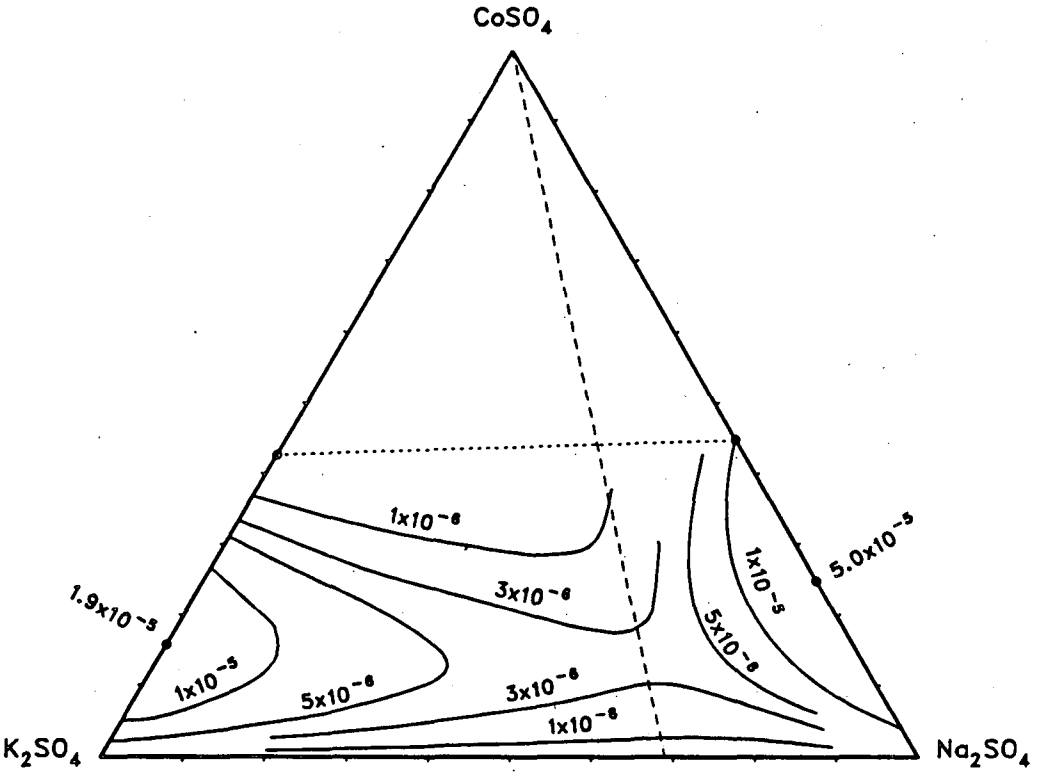

Figure A-5. **SO_3 partial pressures at the freezing point of liquid mixtures in equilibrium with K_2SO_4-$CoSO_4$-Na_2SO_4 solid solutions, Co_3O_4 (s), and 1 atm O_2, calculated as described in the text. The locus of points describe a saddle surface. The dashed line with a 69:31 Na_2SO_4:K_2SO_4 mole ratio passes approximately through the saddle point. Partial pressures along this line are replotted in Figure 3-1 against the corresponding temperatures taken from the same line in Figure A-4. Relatively small SO_3 partial pressures are required to form low-melting mixtures for all Na_2SO_4:K_2SO_4 mole ratios between about 1:9 and 9:1.**

Table A-1

FREE ENERGY OF "PURE" COMPONENTS IN EACH PHASE

Component (Phase)	G^0 (cal/mol)
K_2SO_4 (ss)	0.
$CoSO_4$ (ss)	12,805 - T * 7.113
Na_2SO_4 (ss)	0.
K_2SO_4 (liq)	ΔG_{fus} (T) (Ref. [22])
$CoSO_4$ (liq)	9962 - T * 7.229
Na_2SO_4 (liq)	ΔG_{fus} (T) (Ref. [22])

Table A-2

EXCESS FREE ENERGIES OF MIXING OF BINARY PHASES

	G^{xs} (cal/mol)
K_2SO_4 -$CoSO_4$ (ss)	$-3018 * N_1 * N_2$
K_2SO_4 -$CoSO_4$ (liq)	$-(16{,}296 * N_1 + 31{,}267 * N_2) * N_1 * N_2$
Na_2SO_4 -$CoSO_4$ (ss)	$-11{,}311 * N_2 * N_3$
Na_2SO_4 -$CoSO_4$ (liq)	$-10{,}628 * N_2 * N_3$
K_2SO_4 -Na_2SO_4 (ss)	(Ref. [22])
K_2SO_4 -Na_2SO_4 (liq)	(Ref. [22])

N_i = binary mole fraction : 1 = K_2SO_4, 2 = $CoSO_4$, 3 = Na_2SO_4

0.19. Bale and Pelton obtained an excellent empirical fit to the liquidus and solidus curves at all compositions by treating the liquidus phase as a simple regular solution with a negative heat of mixing,

$$\Delta H^m \text{ (liq)} = -1050\, X_{Na_2SO_4}\, X_{K_2SO_4} \tag{14}$$

and assigning the solid solution a positive heat of mixing given by the more complex expression

$$\Delta H^m \text{ (sol)} = [1282.6 - 2581.6\, X_{Na_2SO_4} + 3160.5\, X^2_{Na_2SO_4}]\, X_{Na_2SO_4} X_{K_2SO_4} \tag{15}$$

ANALYSIS OF K_2SO_4-$CoSO_4$-Na_2SO_4 TERNARY PHASE DIAGRAM

The partial ternary phase diagram shown in Figure A-4 was constructed from the three binary diagrams following procedures described by Pelton, Bale and Lin [20]. As always, the partial molar free energy of each component was taken to be the sum of three terms: the free energy of the pure component, its ideal partial molar free energy of mixing, and its excess partial molar free energy of mixing. The free energies of the pure components are listed in Table A-1. The ideal partial molar free energies were calculated by Temkin's model from the cation fractions (see Table A-3).

The geometrical basis for calculating the excess free energies of mixing is shown in Figure A-7. The total excess free energy at point "p" in the liquid or in the solid solution was computed from the total excess free energy of the binary phases at points "a", "b", and "c" by Toop's [24] algorithm by formulae given by Pelton, Bale, and Lin [20]. They describe several such algorithms. Toop's algorithm appeared to be the most natural to apply in this case, since it is asymmetrical in the three components, treating two similarly (K_2SO_4 and Na_2SO_4 were chosen) and one differently ($CoSO_4$). This asymmetry seemed appropriate in the present situation, in which two of the binary diagrams, K_2SO_4-$CoSO_4$ (Figure A-1) and Na_2SO_4-$CoSO_4$ (Figure A-2) are rather similar, and the third, K_2SO_4-Na_2SO_4 (Figure A-6) is rather different.

The partial molar excess free energy of each component at the ternary point "p" was then calculated by numerical differentiation of the total excess free energy at "p". To this was added the free energy of the "pure" component (Table A-1) and the ideal partial molar free energy (Table A-3) to finally yield the partial molar free energy of the component, which is, of course, just RT times the natural logarithm of the activity, the quantity sought.

To carry forth the mathematics of this procedure, it was necessary to invent and describe a fictitious solid solution phase at point "a" in Figure A-7 in the K_2SO_4-$CoSO_4$ binary, which was not observed experimentally by Calcagni and Marotta [8]. Such a phase must exist in reality. Their failure to observe this phase must mean that the maximum extent of the solid solution phase, the point in Figure A-1 that would correspond to point "d" in Figure A-2, must fall very near the K_2SO_4 axis, at a composition containing only a few mole percent $CoSO_4$. A solid solution phase was invented with this point set arbitrarily at 1 mole percent $CoSO_4$ by assuming a regular solution with an excess heat of mixing chosen so that the activity of K_2SO_4 in the solid solution at this composition was just equal

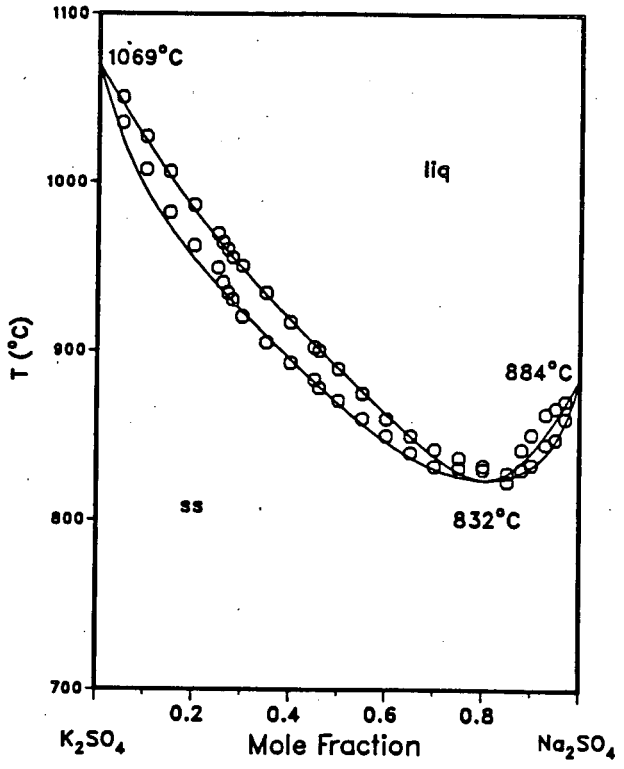

Figure A-6. **K_2SO_4-Na_2SO_4binary phase diagram. Open circles are data points of Perrier and Bellanca [22]. Solid lines were calculated as described in the text using the parameters given by Bale and Pelton [19].**

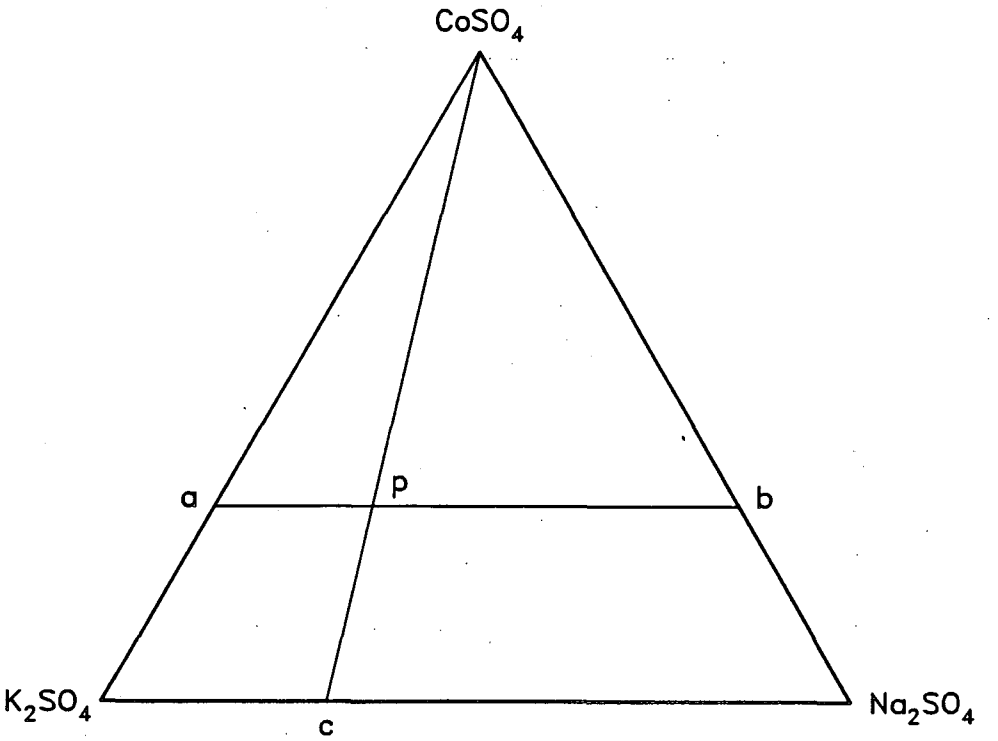

Figure A-7. **Geometrical basis of the Toop algorithm [24] as we apply it. The total excess free energy of mixing in a ternary solution of composition "p" is computed from the corresponding quantities in the same phase at compositions "a", "b", and "c" in the three binary systems. Pelton, Bale, and Lin [20] give the correct equations for the Toop algorithm for several kinds of salt mixtures, including the present one where there are three salts with a common anion.**

Table A-3

TEMKIN IDEAL FREE ENERGIES OF MIXING

	$\underline{g^{ideal}}$
K_2SO_4	$2\ RT\ In\ (2\ M_1 / 2\ M_1 + M_2 + 2M_3)$
$CoSO_4$	$RT\ In\ (M_2 / 2\ M_1 + M_2 + 2M_3)$
Na_2SO_4	$2\ RT\ In\ (2\ M_3 / 2\ M_1 + M_2 + 2M_3)$

M_i = ternary mole fraction : 1 = K_2SO_4, 2 = $CoSO_4$, 3 = Na_2SO_4

to that in the liquid at the eutectic point. The value required for the excess heat of mixing was -3018 cal/mol. This is the first value listed in Table A-2. The exact value of this parameter is irrelevant in the ternary diagram so long as it is not too large and negative, i.e., so long as it is chosen to give the correct result that the solid solution phase has negligible extent in the K_2SO_4-$CoSO_4$ binary.

Using this method for estimating free energies, liquidus temperatures were calculated. These are the temperatures at which a liquid of a given composition will just begin to freeze. Given the composition of a point in the liquid, the mathematical problem involved in determining its freezing point is to find a temperature (one degree of freedom) and a solid solution composition (two more degrees of freedom in a ternary) at which three functions all vanish simultaneously, the three functions being the ratio for each component of its activity in the liquid to its activity in the solid solution. The strategy was to guess an answer and march forward. It began by guessing a temperature and solid solution composition. The three activity ratios and also their derivatives with respect to the temperature and the solid solution mole fractions were calculated. The ratios and their derivatives were used to compute a next guess. The procedure was repeated until the three activities differed by less than 1%.

The freezing temperatures so calculated are shown in Figure A-4. The SO_3 partial pressure at the freezing temperature in equilibrium with $CoSO_4$(s) and 1 atm 0_2 was calculated from the partial molar free energy of $CoSO_4$ that was found. These values are shown in Figure A-5.

Results are shown in these figures only for approximately the lower half of the ternary as it is drawn. These are really the only points of interest in connection with hot corrosion phenomena. The calculated results in the rest of the diagram are quite uncertain. Near the center of the diagram one expects the freezing liquid to be in equilibrium with various double and triple salts, judging both from the K_2SO_4-$CoSO_4$ and Na_2SO_4-$CoSO_4$ binary diagrams and from ternary diagrams of other salt mixtures. Because the free energies of these solids are completely unknown, we cannot calculate freezing points in this region. The uncertainty in the calculations near the top corner of the diagram, where the freezing liquid is in equilibrium with $CoSO_4$ (s), is illustrated by the poor fit of the calculated line to the experimental points on the left side of Figure A-1.

SO_3 partial pressures at the freezing points were calculated from the $CoSO_4$ activities, and these are shown in Figure A-5. These are the minimum SO_3 partial pressures required to cause a liquid to form and, thus, to cause aggravated hot corrosion. The locus of points describe a saddle surface. The dashed line with a 69:31 Na_2SO_4:K_2SO_4 mol ratio passes approximately through the saddle point. Partial pressures along this line are replotted in Figure 3-1 against the corresponding temperatures taken from the same line in Figure A-4. The curvature of the central part of the saddle surface is fairly flat from left to right. Relatively small SO_3 partial pressures are required to form low-melting mixtures for all Na_2SO_4:K_2SO_4 mole ratios between about 1:9 and 9:1. Plots of P_{SO_3} versus T at any of these compositions are similar to the dashed curve in Figure 3-1.

APPENDIX B

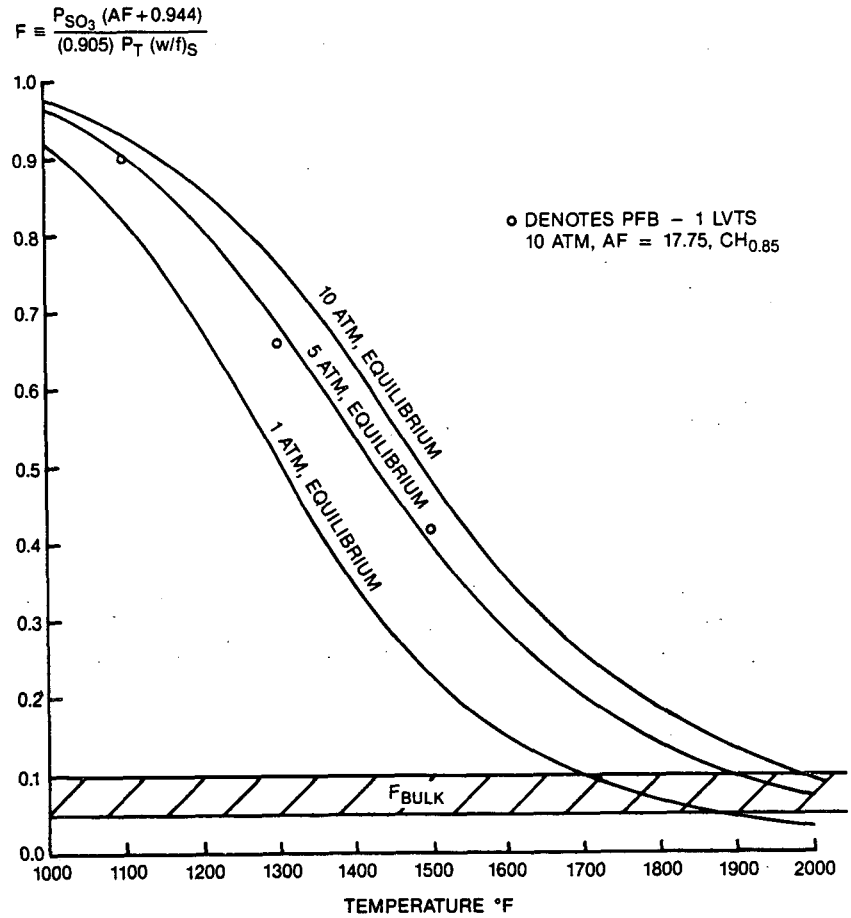

NOTES: Equilibrium lines based on $SO_2 + \frac{1}{2} O_2 = SO_3$
F (bulk) range refers to fraction commonly found in combustion gases.

Figure B-1 Fraction (F) of sulfur converting to SO_3

APPENDIX C

The current understanding of low-temperature hot corrosion is that sulfur trioxide in hot combustion gases reacts with nickel and cobalt oxides to form sulfates. These alloy sulfates mix with sodium and potassium sulfates to form low melting liquids. These low melting liquids produce the aggressive hot corrosion which is observed.

This hypothesis provides for several ways of eliminating this form of corrosion. One is by a reduction of the SO_3 pressure below the value required to stabilize the alloy sulfates. This has been shown to be possible in the results of tests 2 and 6. Another is through a reduction in the activities of Co and Ni oxides sufficient to make sulfate formation unfavorable.

This form of prevention is investigated here by considering the presence of V as a fuel additive. In the combustion gases this would be converted almost entirely to vanadium pentoxide, V_2O_5. Some of this would react with NiO or CoO to form the respective ortho-vanadate

$$3\,NiO + V_2O_5 \rightarrow Ni_3(VO_4)_2 \qquad (1)$$

$$3\,CoO + V_2O_5 \rightarrow Co_3(VO_4)_2 \qquad (2)$$

Thermodynamic data are available [1] for $Ni_3(VO_4)_2$ but not, so far as can be found currently, for $Co_3(VO_4)_2$. From these data [1] the results are calculated and shown in Table C-1. Displayed is the NiO activity in the presence of unit activity of V_2O_5 and of $Ni_3(VO_4)_2$. At lower temperatures, below about 1100 K (1520 °F), reaction 3 proceeds from left to right, and the NiO activity is less than unity, as desired. Under these circumstances a correspondingly higher partial pressure of SO_3 could be tolerated in the combustion gas without producing $NiSO_4$. The predicted effect is large enough to be experimentally observable, though not very large. The magnitude of the effect in the cobalt system cannot be predicted at this time.

Table C-1

Activity of NiO in the presence of V_2O_5 and $Ni_3(VO_4)_2$

T (k)	T (F)	[NiO]
700	800	0.153
800	980	0.264
900	1160	0.416
1000	1340	0.686
1100	1520	1.255
1200	1700	2.169

If this reaction were to be considered as a means to control low-temperature hot corrosion in coal combustion atmospheres, there are obvious considerations: The use of V_2O_5 is rather paradoxical, because V_2O_5 itself has a relatively low melting point (960 K = 1270 °F) and, if present in substantial amounts, will cause severe corrosion. Therefore, the amount of V_2O_5 added must be carefully titrated in order to assure that all of it reacts to form vanadates. No excess can be left over, hence the addition of magnesium in test 8 which will react with V_2O_5 to form magnesium vanadate.

REFERENCES

[1] H.S. Spacil and K.L. Luthra, *J. Electrochem. Soc. 129,* 2119 (1982).

[2] R.W. Haskell, H. von E. Doering, and D.F. Grzybowski, Stationary Gas Turbine Alternate Fuels, ASTMSTP 809, J.S. Clark and S.M. DeCorso, eds., American Society for Testing and Materials, Philadelphia, Pa., p. 156, (1983).

[3] L.T.H.C. Na$^{\Delta}$K Report.

[4] K.L. Luthra and D.A. Shores, *J. Electrochem. Soc. 127,* 2202 (1980).

[5] K.L. Luthra, *Met. Trans. 13A,* 1843 and 1853 (1982).

[6] R.L. Jones, in "High Temperature Corrosion," R.A. Rapp (ed.), NACE-6, National Association of Corrosion Engineers, Houston, TX, p. 513 (1983).

[7] S.Y. Hwang, G.H. Meir, F.S. Pettit, G.R. Johnson, V. Provenzano, and F.A. Smidt, in "High Temperature Protective Coatings," S.C. Singhal (ed.), The Metallurgical Society of AIME, New York, p. 121 (1982).

[8] G. Calcagni and D. Marotta, *Gaz. Chem. Ital. 43,* 380 (1914).

[9] National Coal Board/Coal Utilization Research Laboratory, Leatherhead, England, "Fluidized Bed Combustion: 1000-hour Test Program in a Pressurized Fluidized Bed Combustion Facility," Final Report No. FE-3121-15, Prepared for the U.S. Department of Energy under Contract ET-78-C-01-3121.

[10] Exxon Research and Engineering Company, Linden, NJ, "Hot Corrosion/Erosion Testing of Materials for Application to Advanced Power Conversion Systems Using Coal-Derived Fuels, Task II - Fluidized Bed Combustion," Final Report No. FE-2452-39, November 1979, Prepared for the U.S. Department of Energy under Contract EX-76-C-01-2452.

[11] K.P. Lilleurd and P. Kofstad, Oxid. of Metals *21,* 223 (1984).

[12] O.H. LeBlanc and D.A. Shores, Extended Abstracts, Fall Meeting of the Electrochemical Society, Montreal, October 1982, Vol. 82-1, Electrochemical Society, Pennington, NJ, 1982, Abstract 254.

[13] A.K. Misra, D.P. Whittle, and W.L. Worrell, *J. Electrochem. Soc., 129,* 1840 (1982).

[14] JANAF Thermochemical Tables, The Dow Chemical Company, Midland, MI, 1971; Supplement 1974; Supplement 1975; Supplement 1978; Supplement 1982.

[15] H.K. Hardy, *Acta Met. 1,* 202 (1953).

[16] T. Forland, *J. Phys. Chem. 59,* 152 (1955).

[17] M. Temkin, *Acta Physiochem USSR 20,* 411 (1945).

[18] M. Blander, "Molten Salt Chemistry," Wiley-Interscience, p. 127 (1964).

[19] C.W. Bale and A.D. Pelton, *CALPHAD 6,* 225 (1982).

[20] A.D. Pelton, C.W. Bale, and P.L. Lin, *Can. J. Chem. 62,* 457 (1984).

[21] K.A. Bol'shakov and P.I. Fedorov, *Zh. Obsch. Khim. 26,* 367 (1956).

[22] C. Perrier and A. Bellanca, *Periodico Mineral.* (Rome) 11, 163 (1940).

[23] T. Ostvold and O.J. Kleppa, *Acta Chem. Scand. 25,* 919 (1971).

[24] G.W. Toop, *Trans. Met. Soc.-AIME 33,* 850 (1965).

[25] B.V. Slobodin, I.I. Miller, and A.A. Fotiev. "Termodynamics of Iron (III). Chromium (III), and Nickel (III) Orthovanadates," *Russ. J. Phys. Chem. 49,* pp. 511-4, (1975).

REPORT DISTRIBUTION LIST

1. ALLISON GAS TURBINE OPERATIONS, Mail Stop W-5, P.O. Box 420, Indianapolis, Indiana 46206

   P. Khandelwal

2-3. ARGONNE NATIONAL LABORATORY, 9700 S. Cass Avenue, Argonne, Illinois 60439

   W. A. Ellingson
   K. Natesan

4. ASEA PFBC, S-612 20, FINSPONG SWEDEN

   S. A. Jansson

5. BABCOCK AND WILCOX, Corrosion Technology Section, P. O. Box 835, Alliance, Ohio 44601

   P. L. Daniel

6. BATTELLE COLUMBUS LABORATORIES, 505 King Avenue, Columbus, Ohio 43201

   I. G. Wright

7. BETHLEHEM STEEL CORPORATION, Bethlehem, Pennsylvania 18016

   B. L. Bramfitt

8. CBI INDUSTRIES, 800 Jorie Blvd., Oak Brook, Illinois 60521

   W. R. Mikesell

9. CANADA CENTER FOR MINERAL AND ENERGY TECHNOLOGY, 555 Booth Street, Ottawa, Ontario, Canada K1A OG1

   Mahee Sahoo

10. CASE WESTERN RESERVE UNIVERSITY, Department of Metallurgy and Materials Science, 10900 Euclid Avenue, Cleveland, Ohio 44106

   K. M. Vedula

11. COMBUSTION ENGINEERING, 1000 Prospect Hill Road, Windsor, Connecticut 06095

   A. Plumley

12-14. ELECTRIC POWER RESEARCH INSTITUTE, 3412 Hillview Avenue, P.O. Box 10412, Palo Alto, California 94303

W. T. Bakker
R. I. Jaffee
J. T. Stringer

15. FOSTER WHEELER DEVELOPMENT CORPORATION, Materials Technology Department, John Blizard Research Center, 12 Peach Tree Hill Road, Livingston, New Jersey 07039

J. L. Blough

16. HANFORD ENGINEERING DEVELOPMENT LABORATORY, P.O. Box 1970, Richland, Washington 99352

R. N. Johnson

17. KENTUCKY CENTER FOR ENERGY RESEARCH, Iron Works Pike, P.O. Box 13015, Lexington, Kentucky 40512

V. K. Sethi

18. THE JOHNS HOPKINS UNIVERSITY, Materials Science and Engineering, Baltimore, Maryland 21218

R. E. Green, Jr.

19. THE MATERIALS PROPERTIES COUNCIL, INC., United Engineering Center, 345 E. Forty-Seventh Street, New York, New York 10017

M. Prager

20. NASA-LEWIS RESEARCH CENTER, Lewis Library, MS 60-3, 21000 Brookpark Road, Cleveland, Ohio 44135

K. Grasse

21. NATIONAL BUREAU OF STANDARDS, Materials Building, Gaithersburg, Maryland 20899

S. J. Dapkunas

22. NATIONAL MATERIALS ADVISORY BOARD, National Research Council, 2101 Constitution Avenue, Washington, DC 20418

K. M. Zwilsky

23-36. OAK RIDGE NATIONAL LABORATORY, P. O. Box X, Oak Ridge, TN 37831

R. A. Bradley
P. T. Carlson
J. A. Carpenter
J. H. DeVan
W. N. Drewery, Jr. (8)
H. S. Hsu
R. R. Judkins

37. OFFICE OF NAVAL RESEARCH, Code 431, 800 N. Quincy Street, Arlington, Virginia 22217

S. G. Fishman

38. SOLAR TURBINES INTERNATIONAL, P. O. Box 85376, San Diego, California 92138

R. L. McCarron

39. UNITED TECHNOLOGIES RESEARCH CENTER, East Hartford, Connecticut 06108

K. M. Prewo

40. UNIVERSAL ENERGY SYSTEMS, INC., 4401 Dayton-Xenia Road, Dayton, Ohio 45432

V. Srinivasan

41-42. UNIVERSITY OF PITTSBURGH, School of Engineering, Department of Metallurgical & Materials Engineering, 848 Benedum Hall, Pittsburgh, Pennsylvania 15261

G. H. Meier
F. S. Pettit

43. DEPARTMENT OF THE ARMY, Army Materials and Mechanics Research Center, Watertown, Massachusetts 02172

D. R. Messier

44-46. DOE, MORGANTOWN ENERGY TECHNOLOGY CENTER, P.O. Box 880, Morgantown, West Virginia 26505

H. Webb
N. Holcomb
J. McClung

47-49. DOE, OFFICE OF FOSSIL ENERGY, Washington, DC 20545

J. P. Carr
K. N. Frye
R. T. King

50. DOE, OFFICE OF BASIC ENERGY SCIENCES, Materials Sciences Division, Washington, DC 20545

F. V. Nolfi, Jr.

51. DOE, OFFICE OF ENERGY CONVERSION AND UTILIZATION TECHNOLOGY, CE-12, 5E-066/FORS, Washington, DC 20585

J. J. Eberhardt

52. DOE, OFFICE OF VEHICLE AND ENGINE R&D, Route Symbol CE-131, Forrestal Building, Washington, DC 20585

R. B. Schulz

53. DOE, OAK RIDGE OPERATIONS OFFICE, P.O. Box E, Oak Ridge, Tennessee 37831

E. E. Hoffman

54-56. DOE, PITTSBURGH ENERGY TECHNOLOGY CENTER, P.O. Box 10940, Pittsburgh, Pennsylvania 15236

J. I. Joubert
F. W. Steffgen
J. Winslow